Physical Layer Aware Optical Networks

ScuDo
Scuola di Dottorato ~ Doctoral School
WHAT YOU ARE, TAKES YOU FAR

Doctoral Dissertation
Doctoral Program in Electrical, Electronic and Communications Engineering
(30^{th}cycle)

Physical Layer Aware Optical Networks

By

Mattia Cantono

******

Supervisor(s):
Prof. Vittorio Curri, Supervisor
Prof. Roberto Gaudino, Co-Supervisor

Doctoral Examination Committee:
Prof. Alberto Bononi, Referee, Università degli Studi di Parma
Prof. Ioannis Tomkos, Referee, Athens Information Technology Center
Prof. Cristian Antonelli, Università degli Studi dell'Aquila
Dr. Antonio Napoli, Coriant R&D GmbH
Dr. Rosanna Pastorelli, SM Optics s.r.l

Politecnico di Torino
2018

Declaration

I hereby declare that, the contents and organization of this dissertation constitute my own original work and does not compromise in any way the rights of third parties, including those relating to the security of personal data.

Mattia Cantono
2018

* This dissertation is presented in partial fulfillment of the requirements for **Ph.D. degree** in the Graduate School of Politecnico di Torino (ScuDo).

Acknowledgements

First, I would like to thank my advisors Vittorio Curri and Roberto Gaudino for giving me the chance of starting this PhD. I would like to especially thank Vittorio for his mentorship, and guidance in the world of academia, for his unmatched confidence, enthusiasm and leadership when diving into new and unexplored topics. Nevertheless, I would like to thank all the members of the OptCom group, and ISMB for all the learning experiences we shared.

A special thanks to all the people from the industry that helped me in getting a clearer understanding of the bigger picture, and pushed me to develop new solutions, with real-world applicability.

Great thanks to Marco Bertino for his friendship, and for all the coffee we shared. I would like to thank all my fellow colleagues and team members from DET and from the Acquario for their friendship, and for all the good times we shared together. Special thanks to Andrea Arduino, Dario Pilori, Emanuele Virgillito, Shoaib Khaliq, Alessio Ferrari, and Marianna Hovsepyan.

A heartfelt thank to all my friends: to the GAP VG family and to the EV group for always providing a getaway from stress and headaches; to my padrino Calogero for his constant support and understanding; to Giuseppe for all the laughs and all the thoughts we shared; to Fernando for being an example of commitment to excellence.

Finally and most importantly, I would like to thank my family for their unconditional love, and support to help me reach new heights. Special thanks to my father for being an example of perseverance and dedication, to my mother for her unmatched emotional support, and to my sister for her intelligence, and for always being an inspiration for me.

Abstract

This thesis describes novel contributions in the field of physical layer aware optical networks. IP traffic increase and revenue compression in the Telecom industry is putting a lot of pressure on the optical community to develop novel solutions that must both increase total capacity while being cost effective. This requirement is pushing operators towards network disaggregation, where optical network infrastructure is built by mix and match different physical layer technologies from different vendors. In such a novel context, every equipment and transmission technique at the physical layer impacts the overall network behavior. Hence, methods giving quantitative evaluations of individual merit of physical layer equipment at network level are a firm request during network design phases as well as during network lifetime. Therefore, physical layer awareness in network design and operation is fundamental to fairly assess the potentialities, and exploit the capabilities of different technologies.

From this perspective, propagation impairments modeling is essential. In this work propagation impairments in transparent optical networks are summarized, with a special focus on nonlinear effects. The Gaussian Noise model is reviewed, then extended for wideband scenarios. To do so, the impact of polarization mode dispersion on nonlinear interference (NLI) generation is assessed for the first time through simulation, showing its negligible impact on NLI generation. Thanks to this result, the Gaussian Noise model is generalized to assess the impact of space and frequency amplitude variations along the fiber, mainly due to stimulated Raman scattering, on NLI generation. The proposed Generalized GN (GGN) model is experimentally validated on a setup with commercial linecards, compared with other modeling options, and an example of application is shown.

Then, network-level power optimization strategies are discussed, and the Locally Optimization Global Optimization (LOGO) approach reviewed. After that, a novel framework of analysis for optical networks that leverages detailed propagation impairment modeling called the Statistical Network Assessment Process (SNAP) is presented. SNAP is motivated by the need of having a general framework to assess the impact of different physical layer technologies on network performance, without relying on rigid optimization approaches, that are not well-suited for technology comparison. Several examples of applications of SNAP are given, including comparisons of transceivers, amplifiers and node technologies. SNAP is also used to highlight topological bottlenecks in progressively loaded network scenarios and to derive possible solutions for them.

The final work presented in this thesis is related to the implementation of a vendor agnostic quality of transmission estimator for multi-vendor optical networks developed in the context of the Physical Simulation Environment group of the Telecom Infra Project. The implementation of a module based on the GN model is briefly described, then results of a multi-vendor experimental validation performed in collaboration with Microsoft are shown.

Contents

List of Figures

List of Tables

Nomenclature

Acronyms / Abbreviations

ADC Analog-to-Digital Converter

API Application Programming Interface

ASE Amplified Spontaneous Emission

AWGN Additive White Gaussian Noise

CAGR Compound Annual Growth Rate

CAPEX Capital Expenditure

CD Chromatic Dispersion

CDC Colorless Directionless and Contentionless

CDN Content Delivery Network

CPE Carrier Phase Estimation

CSM Coarse Step Method

CUT Channel Under Test

DAC Digital-to-Analog Converter

DC Data Center

DCU Dispersion Compensating Unit

DD Direct Detection

DGD Differential Group Delay

DP-NLSE Dual Polarization Nonlinear Schroedinger Equation

DSP Digital Signal Processing

DWDM Dense Wavelength Division Multiplexing

EDC Electronic Dispersion Compensation

EDFA Erbium Doped Fiber Amplifier

EOL End of Life

FEC Forward Error Correction

FFSS Fast Fiber Simulator Software

FOM Figure of Merit

FWM Four-Wave Mixing

GGN Generalized Gaussian Noise Model

GN Gaussian Noise

GPU Graphic Processing Unit

HFA Hybrid Fiber Amplifier

IMDD Intensity Modulation with Direct Detection

IP Internet Protocol

ISI Inter-Symbol Interference

ISP Internet Service Provider

IX Internet Exchange

LCOS Liquid Crystal on Silicon

LOGO Locally Optimized Globally Optimized

LP Lightpath

M2M Machine-to-Machine

MCA Monte Carlo Analysis

MCS Multicast Switch

ME Manakov Equation

MSA Multi-Source Agreement

NLI Nonlinear Interference

NZDSF Non-Zero Dispersion Shifted Fiber

OADM Optical Add Drop Multiplexer

OEO Optical-Electro-Optical

OFDM Orthogonal Frequency Division Multiplexing

OLA Optical Line Amplifier

OOK On-Off Keying

OOT Over the Top

OSA Optical Spectrum Analyzer

OSNR Optical Signal-to-Noise Ratio

PDL Polarization Dependent Loss

PM Polarization Multiplexed

PMD Polarization Mode Dispersion

PSCF Pure Silica Core Fiber

PSP Principal States of Polarization

QAM Quadrature Amplitude Modulation

QoT Quality of Transmission

QPSK Quadrature Phase Shift Keying

RA Raman Amplifier

ROADM Reconfigurable Optical Add Drop Multiplexer

ROI Return over the investment

RRC Root Raised Cosine

RSA Routing and Spectrum Assignment

RWA Routing and Wavelength Assignment

RWSA Routing and Wavelength or Spectrum Assignment

SBS Stimulated Brillouin Scattering

SNAP Statistical Network Assessment Process

SNR Signal-to-Noise Ratio

SRS Stimulated Raman Scattering

SSFM Split Step Fourier Method

SSMF Standard Single Mode Fiber

TCO Total Cost of Ownership

TDHMF Time Division Hybrid Modulation Format

TIP Telecom Infra Project

VNI Visual Networking Index

WDM Wavelength Division Multiplexing

WSS Wavelength Selective Switch

List of Scientific Contributions

A list of the scientific contributions, with special focus on publications, carried out during the PhD are described here.

List of Publications

Peer Reviewed International Journals Publications

[1] M. Filer, M. Cantono, A. Ferrari, G. Grammel, G. Galimberti, and V. Curri, "Multi-vendor Experimental Validation of an Open Source QoT Estimator for Optical Networks". In: *Journal of Lightwave Technology* Mar. 2018. DOI: 10.1109/JLT.2018.2818406.

[2] D. Pilori, M. Cantono, A. Ferrari, A. Carena, and V. Curri, "On the Effect of Polarization Mode Dispersion on Nonlinear Interference Generations". In preparation for: *Optics Express*.

[3] M. Cantono, D. Pilori, A. Ferrari, C. Catanese, J. Thouras, J.L. Auge, and V. Curri, "On the Interplay of Nonlinear Interference Generation with Stimulated Raman Scattering for QoT Estimation". In: *Journal of Lightwave Technology* Mar. 2018. DOI: 10.1109/JLT.2018.2814840.

[4] V. Curri, M. Cantono, and R. Gaudino, "Elastic All-Optical Networks: A New Paradigm Enabled by the Physical Layer. How to Optimize Network Performances?". In: *Journal of Lightwave Technology*, vol. 35, no. 6,pp. 1211–1221, Mar. 15, 2017. DOI: 10.1109/JLT.2017.2657231.

[5] M. Cantono, R. Gaudino, and V. Curri, "Potentialities and criticalities of flexible-rate transponders in DWDM networks: A statistical

approach". In: *Journal of Optical Communications and Networking*, vol. 8, no. 7, pp. A76-A85, 2016. DOI: 10.1364/JOCN.8.000A76.

[6] M. Cantono, V. Curri, A. Mecozzi, and R. Gaudino, "Polarization-Related Statistics of Raman Crosstalk in Single-Mode Optical Fibers". In: *Journal of Lightwave Technology*, vol. 34, no. 4, pp. 1191-1205, 2016. DOI: 10.1109/JLT.2015.2506481.

[7] M. Cantono, V. Curri, and R. Gaudino, "Raman Crosstalk Suppression in NG-PON2 Using Optimized Spectral Shaping". In: *Journal of Lightwave Technology*, vol. 33, no. 24, pp. 5284-5292, 2015. DOI: 10.1109/JLT.2015.2501058.

[8] M. Cantono, V. Curri, A. Mecozzi, and R. Gaudino, "Interplay between Raman and polarization effects in next-generation passive optical networks". In: *Optics Express*, vol. 23, no. 11, pp. 13924-13936, 2015. DOI: 10.1364/OE.23.013924.

[9] M.S. Khaliq, M. Cantono, S. Straullu, and V. Curri, "Performance assessment of short-reach multi-level pulse-amplitude modulation transmission exploiting least-mean-square equalisation", In: *IET Optoelectronics*, vol. 11, no. 4, pp. 134-140, 2017. DOI: 10.1049/iet-opt.2016.0148.

Contributions to International Conferences

[1] M. Cantono, S. Piciaccia, A. Tanzi, G. Galimberti, B. Smith, M. Bianchi, and V. Curri, "A Statistical Assessment of Networking Merit of 2MxN WSS", in *2018 Optical Fiber Communications Conference and Exhibition*, OFC 2018 - Proceedings, OSA, Mar. 2018, Paper M1A.3.
DOI: 10.1364/OFC.2018.M1A.3.

[2] M. Cantono, J.L. Auge, and V. Curri, "Modelling the Impact of SRS on NLI Generation in Commercial Equipment: an Experimental Investigation", in *2018 Optical Fiber Communications Conference and Exhibition*, OFC 2018 - Proceedings, OSA, Mar. 2018, Paper M1D.2. DOI: 10.1364/OFC.2018.M1D.2.

[3] M. Cantono, F. Guiomar, A. Carena, and V. Curri, "Networking Benefit of Multi-Subcarrier Transceivers", in *2018 Optical Fiber Communications Conference and Exhibition*, OFC 2018 - Proceedings, OSA, Mar. 2018, Paper Tu3E.1. DOI: 10.1364/OFC.2018.Tu3E.1.

[4] M. Cantono, D. Pilori, A. Ferrari, A. Carena, and V. Curri, "Observing the Interaction of PMD with Generation of NLI in Uncompensated Amplified Optical Links", in *2018 Optical Fiber Communications Conference and Exhibition*, OFC 2018 - Proceedings, OSA, Mar. 2018, Paper W1G.4. DOI: 10.1364/OFC.2018.W1G.4.

[5] D. Pilori, M. Cantono, A. Carena, and V. Curri, "FFSS: The fast fiber simulator software", in *2017 19th International Conference on Transparent Optical Networks (ICTON)*, IEEE, Jul. 2017, pp. 1–4. DOI: 10.1109/ICTON.2017.8025002.

[6] M. Cantono, and V. Curri, "Flex- vs. fix-grid merit in progressive loading of networks already carrying legacy traffic", in *2017 19th International Conference on Transparent Optical Networks (ICTON)*, IEEE, Jul. 2017, pp. 1–4. DOI: 10.1109/ICTON.2017.8025171.

[7] M. Cantono, and V. Curri, "Identifying and unlocking topological bottlenecks using SNAP and SDM solutions", in *2017 19th International Conference on Transparent Optical Networks (ICTON)*, IEEE, Jul. 2017, pp. 1–4. DOI: 10.1109/ICTON.2017.8025043.

[8] A. Ferrari, M. Cantono, U. Waheed, A. Ahmad, and V. Curri, "Networking benefits of advanced DSP techniques and hybrid fiber amplification", in *2017 19th International Conference on Transparent Optical Networks (ICTON)*, IEEE, Jul. 2017, pp. 1–4. DOI: 10.1109/ICTON.2017.8025170.

[9] A. Ferrari, M. Cantono, and V. Curri, "Routing Space Size Estimation for Reconfigurable Optical Networks". in *19th Italian National Conference on Photonic Technologies*, Fotonica 2017, IET, May 2017.

[10] M. Cantono, A. Ferrari, and V. Curri, "SNAP-Driven Updates of Physical Layer to Improve Performances of Photonic Networks". in *19th Italian National Conference on Photonic Technologies*, Fotonica 2017, IET, May 2017.

[11] M.Quagliotti, D. Cifuentes Arango, M. Schiano, A. Carena, M. Cantono, and V. Curri, "Spectrum Fragmentation Metrics and their Use in Optical Channel Allocation Algorithms". in *19th Italian National Conference on Photonic Technologies*, Fotonica 2017, IET, May 2017.

[12] A. Ferrari, M. Cantono, and V. Curri, "Networking Benefits of Advanced DSP Techniques". in *19th Italian National Conference on Photonic Technologies*, Fotonica 2017, IET, May 2017.

[13] M. Cantono, A. Ferrari, U. Waheed, A. Ahmad, H. Zaidi, A. Bianco and V. Curri, Networking benefit of hybrid fiber amplification for lightpath regenerators saving", in *2017 Optical Fiber Communications Conference and Exhibition*, OFC 2017 - Proceedings, OSA, Mar. 2017, Paper W4F.7. DOI: 10.1364/OFC.2017.W4F.7.

[14] M. Cantono, R. Gaudino, and V. Curri, "A statistical analysis of transparent optical networks comparing merit of fiber types and elastic transceivers". in *2016 18th International Conference on Transparent Optical Networks (ICTON)*, IEEE, Jul. 2016, pp. 1–4. DOI: 10.1109/ICTON.2016.7550511. Exhibition, OFC 2017 - Proceedings, OSA, Mar. 2017, Paper W4F.7. DOI: 10.1364/OFC.2017.W4F.7.

[15] M. Cantono, R. Gaudino, and V. Curri, "Data-rate figure of merit for physical layer in fixed-grid reconfigurable optical networks". in *2016 Optical Fiber Communications Conference and Exhibition*, OFC 2016 - Proceedings, OSA, Mar. 2016, Paper Tu3F.3. DOI: 10.1364/OFC.2016.Tu3F.3.

[16] V. Curri, M. Cantono, and R. Gaudino, "Elastic All-Optical Networks: A New Paradigm Enabled by the Physical Layer. How to Optimize Network Performances?". in *2016 European Conference on Optical Communication*, ECOC 2016 - Proceedings, VDE, Sep. 2016, pp. 274-276.

[17] M. Cantono, R. Gaudino and V. Curri, "Comparing networking benefits of Digital Back-Propagation vs. Lightpath Regeneration". in *2016 European Conference on Optical Communication*, ECOC 2016 - Proceedings, VDE, Sep. 2016, pp. 403-405.

[18] M. Cantono, R. Gaudino, and V. Curri, "The statistical network assessment process (SNAP) to evaluate benefits of amplifiers and transpon-

ders' upgrades". in *18th Italian National Conference on Photonic Technologies*, Fotonica 2016, IET, May 2016, DOI: 10.1049/cp.2016.0869.

[19] M. Cantono, A. Mecozzi, V. Curri, and R. Gaudino, "Optimal polarization launch for Raman depletion minimization in GPON and TWDM-PON coexistence". in *2015 Optical Fiber Communications Conference and Exhibition*, OFC 2015 - Proceedings, OSA, Mar. 2015, Paper Th2A.60. DOI: 10.1364/OFC.2015.Th2A.60.

List of activities and collaborations

- Collaboration with Cisco Photonics on innovative design strategies for transparent optical networks - *2015 - ongoing*
- Collaboration with SM Optics on impairment modeling in legacy 10G networks - *2016 - ongoing*
- Collaboration with Synopsys on simulation of optical communication systems - *2015 - ongoing*
- Summer Internship within the Optical Network Architecture and Operations Group - Google Inc. - *Summer 2017*
- Collaboration with the Physical Simulation Environment group of the Telecom Infra Project on the development of a vendor-agnostic QoT estimator - *2017 - ongoing*
- Collaboration with OpNear Lab at the University of Texas at Dallas on the development of a Quality of transmission estimation module to be integrated into the ProNet multilayer orchestrator - *2017 - ongoing*

Chapter 1

Introduction

In the last 50 years, the improvements made in terms of capacity, reliability, and flexibility of optical communication systems and networks have been extraordinary. Performances of optical communications systems have always been tightly related to the evolution of optical fiber cables and photonic technologies used to manipulate light. Based on this, in this thesis we consider how the awareness about photonic technologies capabilities and their impact on signal quality can be exploited in the process of designing, update and intelligently manage optical networks. In Chapter 1, an introduction about optical communication technologies and trends in communication networks will be given. Then in Chapter 2, different physical layer models will be presented and their effectiveness in network performance prediction will be discussed. Later in Chapter 3, a framework on physical layer aware network design will be presented, and several examples of application will be shown. Then, in Chapter 4, studies on physical layer aware management of networks will be presented. Finally, in Chapter 5 conclusions will be given and next steps will be discussed.

1.1 Optical Networks: an introduction

Optical networks are communication networks made of interconnected optical fiber cables and constitute the enabling backbone technology of the Internet as we know it today. In optical networks, information is transmitted

through light channels sent over optical fiber cables. Thanks to their unique properties such as low loss and ultra-wide bandwidth, optical fibers enable reliable, high capacity and long-distance communication.

One of the greatest leaps in optical communications has been represented by the evolution from point-to-point communication, where data are transmitted between only two nodes, to fully meshed networking, where optical channels[1] can be added, dropped, and routed at any node. Nowadays, modern optical network architectures provide both high-capacity backhauling to upper network layers, such as the Internet Protocol (IP) layer and the intelligence required for more complex network operations such as efficient routing, protection, and fast circuit restoration. All these capabilities have been enabled by the development of optical network elements and photonic technologies with the potentialities to handle such challenges in an efficient manner. In general, performances of optical networks are tightly related to the evolution of optical fiber cables and photonic technologies used to manipulate the light channels. In the last 50 years, the improvements made in terms of capacity, reliability, and flexibility are extraordinary.

The first deployments of optical communication technologies date back to 1977 when the first point-to-point optical links were installed in Turin (Italy) and Long Beach (US, California) to carry live telephone traffic [1]–[3]. In the 1980s, the steady reduction of fiber losses, and the development of Erbium Doped Fiber Amplifiers (EDFAs) [4] enabled an unprecedented increase in optical reach of point-to-point systems. As far as transceivers are concerned, data rates per channel have consistently grown with a Compound Annual Growth Rate (CAGR) of 20%[5], moving from few Mbps of Intensity Modulation with Direct Detection (IMDD) based transceivers, to 400 Gbps channels based on polarization multiplexed (PM) high order quadrature amplitude modulation (QAM) formats received using a polarization diversity coherent receiver. Thanks to digital signal processing (DSP) capabilities, modern transceivers allowed a relevant simplification of optical line systems thanks to the removal of in-line dispersion compensating units (DCUs) , allowing

[1] In this thesis, we will refer to optical channels, or wavelenghts, or lightpaths. In general, a channel is a portion of the optical spectrum carrying data between a transmitter and a receiver.

a relevant complexity reduction in link design and optical infrastructure management.

A further increase in capacity of optical systems has been enabled by the introduction of Wavelength Division Multiplexing (WDM) techniques. By centering optical channels around different optical frequencies, the fiber bandwidth is efficiently used by carrying multiple optical channels, thus increasing the total amount of carried data. In the 1990s, commercial WDM systems experienced an aggregate per-fiber capacity growth at a 100% CAGR, i.e. doubling capacity year by year. After the year 2000 and the infamous Telecom or Dot-Com bubble[6], [7], such growth has rapidly decreased to a 20% CAGR[5], following the same trend of single channel data rates. This means that practically, the number of WDM channels in commercial systems has been constant for almost two decades, being close to 100 channels. However, today such trend is changing, as C+L band systems that exploit close to 200 WDM channels are gaining traction [8], and commercial systems with these characteristics are nowadays available [9].

One of the most relevant advance in optical networking architectures has been represented by the introduction of add, drop and routing capabilities of optical channels at individual network nodes. This allowed to greatly simplify channels deployment, automating the time consuming and error prone practice of manually rearranging optical channels through optical demultiplexers and patch panels [10]–[13]. Furthermore, this empowered an unprecedented network agility that has been exploited to enable reliable and intelligent networks [14]. The network elements that enabled such progress, are optical add drop multiplexers (OADMs) . OADMs were first constructed from optical filters, allowing for independent wavelengths to be terminated at network nodes, or to bypass them. OADMs are based on prearranged and fixed optical configurations, thus one of their main disadvantages is their limited adaptability with respect to traffic and channels configuration variations. To solve this issue, reconfigurable optical add drop multiplexers (ROADM) have been proposed, and nowadays ROADMs are heavily deployed in the majority of existing optical networks, enabling fully agile, highly connected and dynamically reconfigurable photonic mesh.

1.2 Capacity Crunch and Revenue Compression in the Telecom Industry

Although the capability of photonic technology to carry more and more data has consistently grown in the last decades, the growth of global IP traffic has been even more impressive. Depending on sources, traffic and geographical taxonomies, network traffic growth is envisioned to grow at a CAGR that varies from 25% to 80% [5], [15]–[17]. High definition video applications and Machine-to-Machine (M2M) communications will represent the main drivers of such impressive growth [15], [18]. The Cisco Visual Networking Index (VNI)[15] is one of the most reputable sources for IP traffic volume forecasting. In its latest VNI report, Cisco states that the worldwide IP traffic will grow with a CAGR of 24% up to 2021, reaching a total of 232.7 Exabytes (EB)[2] per month in 2021. Breaking down the total traffic prediction by type, forecasts show that mobile traffic will increase by a 43% CAGR, whereas fixed Internet and managed IP services will grow by a 23% and 13% CAGR respectively [15]. As shown in Fig. 1.1a, fixed Internet traffic will represent the majority (68%) of the overall IP traffic across the considered 5 years. Managed IP services will instead decrease from 24% to 15% of the overall traffic. Mobile traffic will progressively increase from 7% to 17% of the overall traffic, overcoming managed IP services during 2020.

As forecasting results heavily depend on the underlying assumptions used to extrapolate data, it is interesting to analyze historical traffic data from Internet Service Providers (ISPs) and Internet Exchange (IX) consortia. Fig. 1.1b depicts the total (ingress+egress) average monthly traffic passing through the Amsterdam Internet Exchange (AMS-IX) over a 16 years time span, from July 2001 up to September 2017. Data depicted in Fig. 1.1b have been elaborated from the one publicly available in [17]. In 2001, the average monthly traffic flow was around 6 Gbps, corresponding to a total of 1950 Terabyte (TB) exchanged on average each month. In 2017, the average monthly traffic flow went up to 6.839 Tbps, corresponding to an average of 2216 Petabyte (PB) exchanged each month. This growth corresponds to a CAGR of 55%, that can be further split in a 120% growth from 2001

[2] An Exabyte corresponds to 10^{18} bytes, i.e. one billion gigabytes

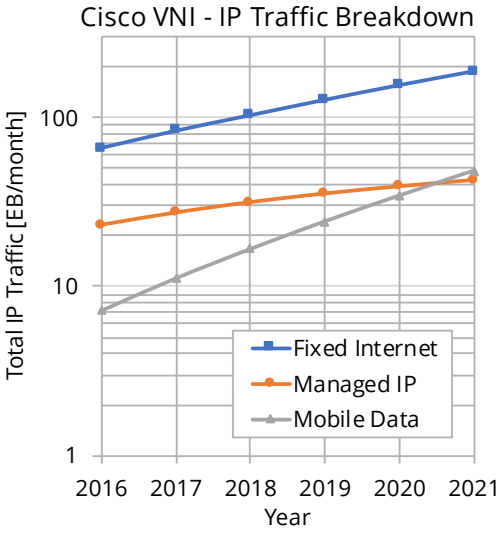

(a) Cisco Visual Networking Index global IP traffic predictions.

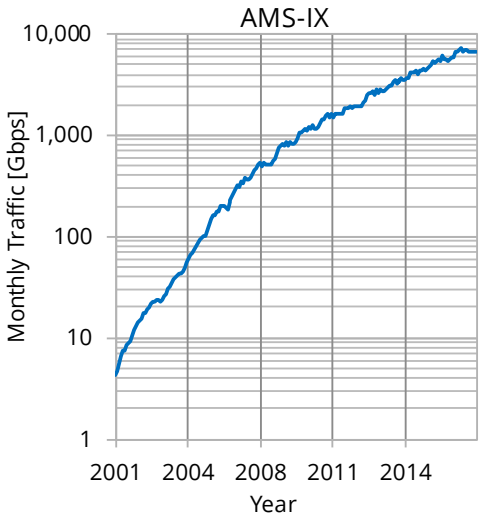

(b) Total monthly traffic of the Amsterdam Internet Exchange.

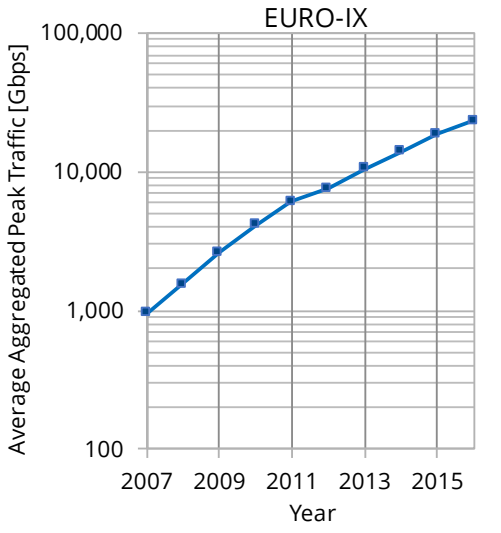

(c) Average aggregated peak traffic in the IXs of the Euro-IX consortium.

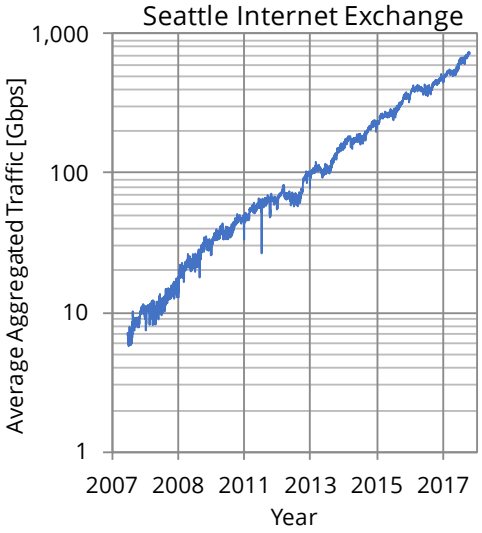

(d) Seattle Internet Exchange total aggregated IP traffic.

Fig. 1.1 Predictions and statistics for IP traffic from different sources. Data elaboration have been performed starting from the data reported by Cisco VNI [15], the Amsterdam Internet Exchange [17], the European Internet Exchange consortium [16], and the Seattle Internet Exchange [19].

to 2007 and a 30% growth in the next 10 years. A similar trend can be observed in the monthly averaged peak traffic aggregated over all IXs of the European Internet Exchange (EURO-IX) consortium depicted in Fig. 1.1c, with a 46% CAGR from 2007 to 2016, moving from 955 Gbps in 2007 to 23.2 Tbps in 2016. This trend can be further divided into a 60% growth from 2007 to 2011 and a 30% growth from 2011 to 2016. These double regimes in traffic growth can be attributed to the fact that several over-the-top (OOT) content providers such as Google, Netflix, Facebook started to perform private peering, thus not relying on public IX providers [20], [21] and use private content delivery networks (CDNs) and caches to serve their users directly from their private networks [22]–[25]. This entails that certain traffic types such as video streaming applications are bypassing public IXs, thus they are not taken into account into data volume statistics. This behavior is not present in the data of the Seattle Internet exchange (SIX) that are depicted in Fig. 1.1d, where the average aggregate traffic has been steadily growing in the last 10 years from 7 Gbps in 2007 to the current 707 Gbps with a 58% CAGR [19].

Optical communication technologies have been the key enablers of this impressive growth rate, but as of today, they are getting closer to approaching fundamental limits of optical system information capacity. Specifically, performances of optical systems are close to the nonlinear Shannon limit [26], that represents the ultimate limit for a point-to-point fiber optics communication system. Therefore maximum data rates of optical communication systems are starting not to keep up with the pace of growth of IP traffic [5]. This is putting a lot of pressure on the telecom industry to find economically sustainable solutions to accommodate such a high bandwidth demand. This requirement is even more stringent if one considers that revenues for telecom operators have been steadily decreasing in the last decade, and it has been predicted that cost per bit will exceed operator revenues [27] even though the cost per bit is decreased by 26% in the period between 2006 and 2013 [28]. As an example, Fig. 1.2 depicts the global operator revenues that are obtained from fixed voice and broadband services reported in [29]: a -2% CAGR is predicted up to 2019. Although operators are recovering from this losses by providing new services such as cloud computing and CDN services [28], they need to optimize their returns over investment (ROI) for optical net-

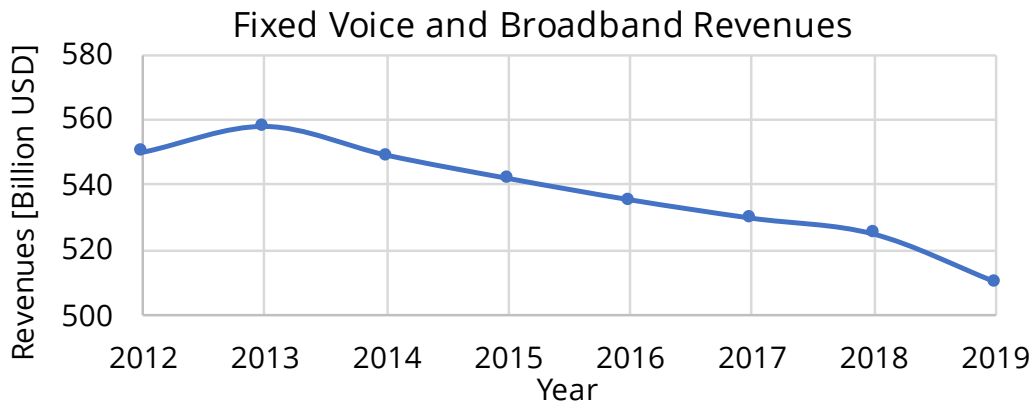

Fig. 1.2 Global Fixed Voice and Broadband revenues. Data taken from [29].

working equipment and installed fibers [30]. In particular, operators want to exploit as much as possible the existing fiber infrastructure that was mainly installed before the dotcom bubble in the 2000s, as replacing deployed fiber is extremely expensive [30].

Operators are therefore acting under two opposite forces: they need to be able to provide the infrastructure to sustain the growth in traffic while balancing costs and revenues. In this context, a clear assessment of the impact of photonic communication technologies in terms of network capacity improvement, improved network management opportunities and the related costs/benefits trade-offs is a firm requirement for both operators and vendors. The formers need to understand which technologies should be used in designing and upgrading new and existing topologies, the others need to understand which technology should they focus on for their future developments. Traditionally, the impact of transmission layer technologies is analyzed in the context of fully-loaded point-to-point links, but this constitutes an upper limit for network performances as wavelength and spectrum contention prevents a full usage of the spectrum in fiber links. One of the aims of this thesis is to provide a framework of analysis to fairly assess photonic layer technologies in the context of transparent, reconfigurable and flexible optical networks, starting from a detailed modeling of the physical layer impairments. Before digging into the main topics of this thesis, an overview of state of the art optical networking infrastructure will be given.

1.3 Flexible, transparent and reconfigurable optical networks

One of the main leaps in optical communications technologies has been represented by the introduction of DSP-based transceivers operating with multilevel modulation formats with coherent receivers and channel equalization [31], [32]. Thanks to them, backbone optical networks have changed in nature over the last decade. Due to the deployed transmission techniques based on direct-detection (DD) transceivers, optical links in legacy networks behaved like sealed data pipelines, not allowing much flexibility in reach or bitrate adaptation. This was due to the fact that DD transceivers required optimized dispersion compensation along optical links to achieve sufficient reach performances [33], [34]. However, such optimization was only effective for a given modulation format, bit rate, and WDM channel spacing. In this scenario, transparent wavelength routing was limited and forced to be established in the network design phase, and optical-electro-optical (OEO) traffic regeneration in nodes was heavily adopted due these inherent technological limitations. Thus, in general, transparency and flexibility at the logical network level were not met at the optical transmission level. Capacity and connectivity matrices in legacy networks were sparse and static [35], as optical capacity was immutably established during the network design phase due to the tight operative constraints imposed by dispersion management schemes.

During the last decade, the development of fast digital-to-analog (DAC) and analog-to-digital (ADC) converters , together with fast DSP units, has enabled an unprecedented flexibility in optical transmission [36]. The introduction of electronic dispersion compensation (EDC) [37], [38] and DSP-enabled equalization [39] allowed to easily compensate all linear propagation effects such as chromatic dispersion (CD) , and polarization mode dispersion (PMD) at the receiver stage. The introduction of DSP based transceivers enabled the development of adaptable optical transmitter and receivers that operate using different signal constellations that dynamically trade-off rate and sensitivity at a given spectral occupancy [40], [41]. More importantly, DSP-enabled transceivers allowed to remove DCUs from optical links with-

out performance penalties [42], making possible a decoupling of optical line systems and line terminals. A first direct consequence of this has been represented by an improved flexibility in transparent wavelength routing, as optical channels can be routed over different optical links as precisely tuned dispersion management is not necessary anymore, provided that their quality-of-transmission (QoT) is maintained above an in-service threshold that depends on the transceiver implementation. This capability drove the development of improved ROADM architectures that enabled reconfigurable and transparent optical networking [11].

Furthermore, DSP-enabled transceivers opened new disaggregation opportunities in the optical communications industry enabling the optimization of infrastructure's total cost of ownership (TCO) : open-line systems [43] and optical white boxes [44] have been introduced to resolve vendor lock-in decoupling of common optical line pieces of equipment such as fiber, amplifiers, optical switches, gain equalizers, etc., from line terminals, i.e. optical transceivers. Such practice has been taken from data center deployments. Data centers are built upon interchangeable, highly standardized node and network architectures rather than a sum of isolated solutions. This leads to a better utilization of line systems and faster innovation due to the decoupling of deployment cycles for line systems and transceivers, thus, in general, lower TCOs.

Fig. 1.3 and Fig. 1.4 represent the evolution of optical line systems enabled by disaggregation and decoupling of line terminals and line optics. Fig. 1.3 depicts a single-vendor legacy line system in which a vendor-provided controller was responsible for the management of both line and terminal equipment. In such scenario with vendor lock-in, operators had not much room for the development of custom controllers, as they had to rely completely on the vendor provided control software yielding an overall rigidity in the design and management of optical networks. This approach to line design was strictly related to the limitations imposed by legacy transceivers, but also the first generations of coherent transceivers have been marketed with the same approach with respect to line system integration. The following generation of coherent transponders and line systems have been proposed to leverage line disaggregation and multi-vendor interoperability. Fig. 1.4 represents one of such novel systems, where both line (such as Optical line

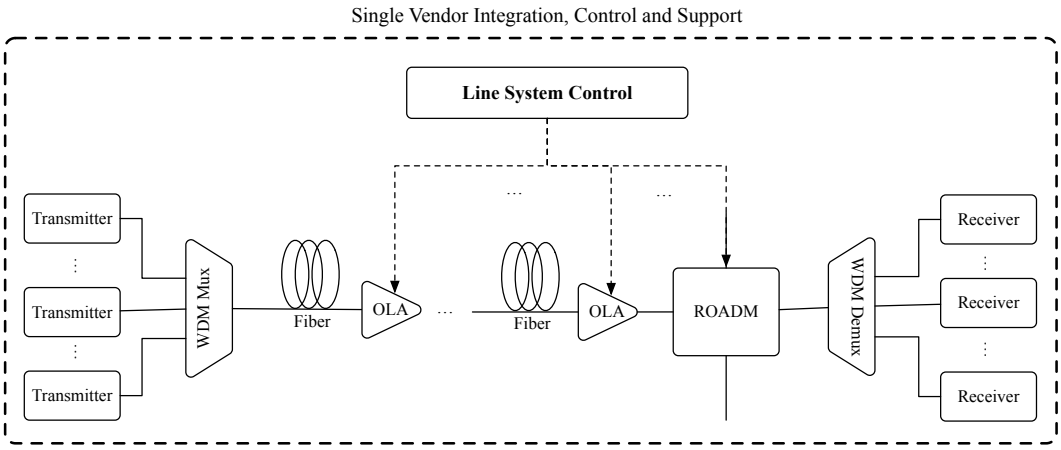

Fig. 1.3 Legacy line systems in optical networks with single vendor integration.

amplifiers (OLAs) and ROADMs) and terminal components can be managed and monitored through open Application Programming Interfaces (APIs) . Thanks to these software interfaces, optical equipment can be controlled and orchestrated by a centralized software intelligence that each operator and network manager can program based on its own personal use cases. If interfaces are kept equal among different vendors, multi-vendor interoperability is made possible. This is one of the motivations behind the different public initiatives and multi-source agreements (MSAs) that several operators have launched in the last 3 years to promote the development of common APIs and data models. Among these initiatives it is worth to mention OpenConfig (lead by Google) [45], the Telecom Infra Project (TIP) (lead by Facebook) [46], and OpenROADM (led by AT&T) [47]. Besides network disaggregation and software defined operations, network architectures evolved towards elasticity and flexibility especially in the spectral dimension. As early as 2008 [48], spectrally elastic optical network (EON) technology was advocated as a possible solution to Internet traffic growth, enabling a superior flexibility and scalability in spectrum allocation [49].

In this modern network scenario, capacity and connectivity matrices of optical networks are now full and elastic, i.e. modifiable over a short time scale [35]. Hence, state-of-the-art optical networks are indeed transparent at every level, and the orchestration [50] of logical and physical layer permits to adapt traffic allocation in order to properly respond to variations in traffic requests over a short time-scale enabling fast service provisioning. State-of-

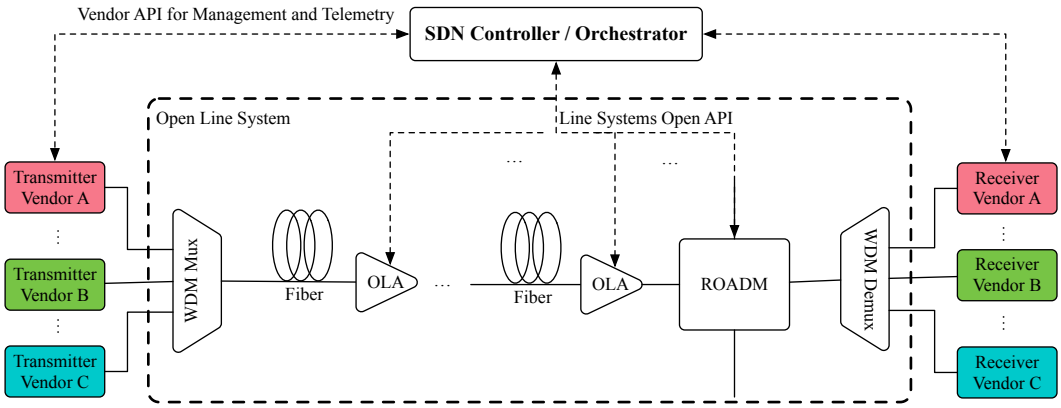

Fig. 1.4 Open line system approach with multi-vendor interoperability and centralized orchestration.

the-art modern optical networks are therefore truly flexible, reconfigurable and transparent as it is possible to: assign capacity dynamically, react to unexpected traffic variations or failures while routing transparently channels in the optical domain without relying on upper electrical layers. In such a novel context, every equipment and transmission technique at the physical layer impacts the overall network behavior. Hence, methods giving *quantitative* evaluations of individual merit of physical layer equipment at network level are a firm request during *network design* phases as well as during network lifetime, when it is essential for the *orchestration* of logical and transmission layers and for addressing selected upgrades to properly react to growth and modifications of traffic requests. Therefore *physical layer awareness* in network design and operation is fundamental to fairly assess the potentialities, and exploit the capabilities of different physical layer technologies in modern flexible, transparent and reconfigurable optical networks. Furthermore, such physical layer awareness has to be vendor agnostic, to be fully adaptable to disaggregated multi-vendor scenarios such as the ones of modern optical telecommunications infrastructure.

1.4 Outline of the remainder of this thesis

In this thesis, a design framework and example of applications of physical layer awareness in optical orchestration are proposed and discussed. All

of them are built upon detailed modeling of propagation impairments affecting optical signals transmitted over the previously described network architecture, as it represents a fundamental requirement to estimate capacity, and assess routing feasibility both at the design and operational phase of the network. Thus as a first step, in the chapter 2 the dominant propagation impairments in optical fibers are discussed. Then, several nonlinear modeling options to estimate nonlinear propagation impairments are reviewed and extended. Based on them, a simple power optimization approach is presented.

In chapter 3 a design framework called the Statistical Network Assessment Process (SNAP) will be presented and several examples of applications will be given.

Finally in chapter 4, an example of applications of the physical layer models discussed in chapter 2 for the implementation of a vendor-agnostic quality of transmission estimator will be given.

The main novelties reported in this thesis include:

- An assessment of the impact of Polarization Mode Dispersion on nonlinear interference generation
- A generalization of the Gaussian Noise (GN) for wideband scenario including spatial and frequency loss/gain profile variations, and its experimental validation
- The integration of the SNAP framework and examples of its application
- The integration of the GN model in orchestration platforms and for the unified design of multivendor network solutions within the TIP organization

Chapter 2

Physical Layer Modeling for Physical Layer Aware Networking

In this chapter, the linear and nonlinear impairments of fiber propagation are briefly discussed. Then different nonlinear modeling options for physical layer aware optical networking are presented. A review of the most common nonlinear models of fiber propagation is presented, and their pros and cons in terms of applicability to a networking scenario are discussed. Finally, a wideband extension of the Gaussian Noise (GN) model, the so-called Generalized Gaussian Noise (GGN) model , and its simulative and experimental validation are presented.

2.1 An introduction to optical propagation impairments

Light signals that propagate along multi-span amplified optical fiber links undergo several physical modifications that impair their capability of carrying information. Putting aside stochastic noise generated by transceivers such as - to mention a few - electrical, thermal, quantization, shot and laser phase noise, the root causes of signal degradation are Amplified Spontaneous Emission (ASE) noise generated by optical amplifiers, linear and nonlinear effects causing signal distortion [51]. Fig. 2.1 qualitatively highlights the

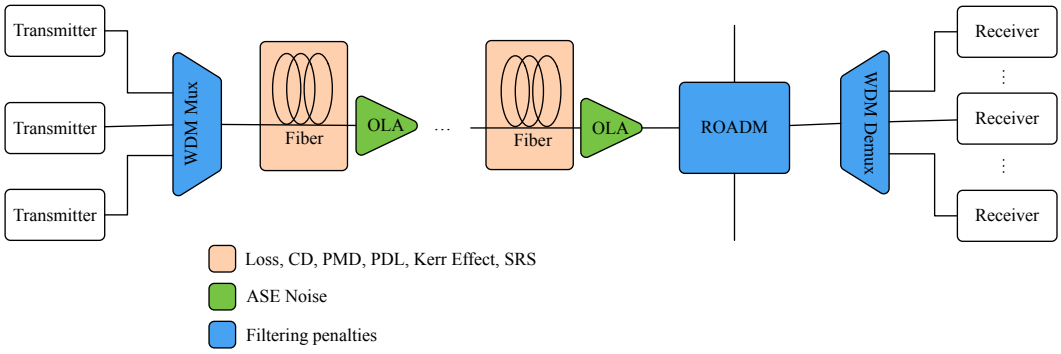

Fig. 2.1 Sources of propagation impairments in an optical communication system

.

sources of these different propagation impairments, i.e. fibers, amplifiers and ROADMs.

All propagation effects that depends linearly with the electric field are classified as linear ones. Linear effects include for example: chromatic dispersion (CD) i.e. a dependence of the group velocity of the signal and its optical frequency [51], polarization mode dispersion (PMD), i.e. a dependence of the group velocity of the signal and its polarization state [52]–[54], polarization dependent loss (PDL), i.e. a random dependence between signal attenuation and polarization [55], signal attenuation due to fiber attenuation, filtering and crosstalk effects at ROADM nodes [56]–[58]. All dispersion and filtering effects cause signal pulses to spread in time, yielding inter-symbol interference (ISI) that impairs the signal. However, the majority of them can be compensated using digital equalization through DSP at the receiver [31], [32], [37], [39], whereas fiber losses are easily recovered through optical amplification.

On the other hand, nonlinear effects are not in linear proportion to the electric field of the signal [51]. Among nonlinear effects is worth citing the Kerr effect, Stimulated Raman Scattering (SRS), and the Stimulated Brillouin Scattering (SBS). The Kerr effect, that causes signal phase distortion due to the dependence of the refractive index of the glass with the power of the optical signal traveling through it [51]. Due to fiber dispersion, such phase distortion is converted into amplitude distortion causing severe penalties. Furthermore, the Kerr effect imposes a limitation on the signal power that needs to be transmitted into an optical fiber link. To this purpose, optical

power optimization strategies are required to maximize the signal Quality-of-Transmission (QoT). As the Kerr effect is one of the most limiting propagation impairments in optical fiber communications, the prediction of its impact on signal quality and the derivation of optimal launch power strategies have been active fields of research over the last couple of decades. During this timespan, several nonlinear models have been developed to achieve this goal so as to facilitate planning, design, and management of coherent optical communication systems and networks. In section 2.5 we will review the broad family of the so-called Gaussian noise models, and highlight the most relevant ones to be used in the context of physical layer aware networking.

SRS [51], [59], [60] and SBS [51], [61] are related to a transfer of energy from the optical field to vibrational modes of silica. In case of SRS, optical phonons are excited, whereas for SBS acoustic ones. SBS is a narrow-band effect (few MHz) affecting, in general, a single channel [51] causing power depletion through the generation of a counter-propagating wave inside the fiber. Nevertheless, SBS is a weak effect for modern communications optical systems where optical signals have in general a spectral occupation much larger than the one for which SBS has peak efficiency. Furthermore, modern multilevel modulation formats have no carrier tones, which helps in further suppressing SBS. On the other hand, SRS is a wideband effect, as the scattering process is significant over spectral occupations of the order of few THz. In modern optical communication systems, SRS causes a power transfer between higher frequency channels to lower frequency one, thus producing a tilt in the power spectrum of the WDM channel comb [62]. As SRS efficiency in silica core fiber is maximum for signals with a frequency separation of approximately 13 THz [51], [60], it is a relevant effect for WDM systems operating over the full C-band and for future C+L band WDM systems [62], [63]. In such future wideband scenario, the interplay between different nonlinear effects like the Kerr effect and SRS needs to be understood. To this purpose, in this thesis, a novel nonlinear model to take this into account is proposed and validated via experiments and simulations.

In the next sections, first different metrics for QoT will be discussed, then a detailed description of different propagation impairments and how to model them will be given.

2.2 The Signal-to-Noise Ratio as a QoT metric

In optical communications, the QoT of a signal has been measured using several different metrics. In legacy scenarios with IMDD transceivers with dispersion compensation, the most widely used metric was the so-called Q-factor [64]–[66]. The Q-factor is directly linked to the BER of the channel under test by the following:

$$\mathrm{BER} = \frac{1}{2}\mathrm{erfc}\left(\frac{\mathrm{Q}}{\sqrt{2}}\right) \tag{2.1}$$

For IMDD, on-off keyed (OOK) signals, the Q-factor can be directly related to the mean levels of the 0 and 1 bit symbols and their standard deviation that can be directly measured from an eye diagram [65], [66]. BER and the Q-factor have been used in physical layer aware networking studies and been object of optimization in the last decade [67]–[69].

With the advent of transceivers with coherent detection, the reference metric for assessing the QoT of a signal has changed to the signal-to-noise ratio (SNR) . It should be noted that for QPSK and PM-QPSK signals, the SNR corresponds to the squared Q-factor. For higher order modulation format such relationship does not hold anymore. In digital transmission, for channels impaired by additive white Gaussian noise (AWGN) , SNR is defined as the ratio between the average power of the useful signal P_{ch}, and the average noise power P_{noise} impairing it [70], i.e.

$$\mathrm{SNR} = \frac{P_{ch}}{P_{noise}} \tag{2.2}$$

We usually consider both P_{ch} and P_{noise} as the signal and noise powers evaluated in the digital domain at the receiver, i.e. in a discrete time domain, after demodulation, equalization, match filtering and sampling. However, assuming ideal coherent transceivers, the transformation from analog to digital domain can be mapped as a linear transformation, therefore a one-to-one mapping between the power computation over these two domains exist. More specifically, with a coherent receiver, there is a one-to-one mapping between the analog optical domain and the electrical digital domain. For this reason, SNR is often related to the so-called Optical SNR (OSNR) , that is the

ratio between the power of the optical signal and the power of the optical noise. The main difference between the two, is due to the fact that in general OSNR is expressed with respect to a specific noise bandwidth B_{noise}, whereas the SNR always refers to the bandwidth of the matched filter used for the detection, i.e. the symbol rate of the signal R_s. The relationship between SNR and OSNR is the following:

$$SNR = OSNR \frac{B_{noise}}{R_s} \tag{2.3}$$

From Eq. 2.3, it is obvious that the SNR and the OSNR are equal when $B_{noise} = R_s$. Such difference between SNR and OSNR has historical reasons, as OSNR has been defined as a metric to express the ratio between signal power and ASE noise, i.e. AWGN. In this context, OSNR measurements are performed by means of an Optical Spectrum Analyzer (OSA) by evaluating the difference between the integral of signal level and the integral of the noise floor over a certain bandwidth, i.e. the noise bandwidth over which the OSNR is defined. A typical reference noise bandwidth is the 0.1 nm bandwidth, that in the C-band roughly correspond to 12.5 GHz.

Throughout this thesis, SNR will be assumed as the reference QoT metric, as it assumed that all noise-related propagation impairments can be modeled as AWGN. As detailed described in the next section such hypothesis holds well for both ASE noise and nonlinear disturbances generated by the Kerr effect, therefore SNR is a safe metric to use. Specifically, the so-called *generalized* or *effective* SNR [71] will be proposed.

Furthermore, SNR is also directly related to BER, and, more generally, to the quantity of information that can be transmitted over a link, i.e. its capacity. In the following section, we will describe how to model different propagation impairments in order to derive the SNR as QoT metric.

2.3 Modeling ASE noise

ASE noise is one of the main source of impairments in optical communication systems. As its name suggests, ASE noise arises from spontaneous emission of the gain medium in an optical amplifier. Considering Erbium Doped Fiber

Amplifiers, it is possible to model the ASE noise as additive White Gaussian Noise with bilateral PSD including both polarization [65], [72] given by

$$G_{ASE} = 2hf_0 n_{sp}(G-1) \tag{2.4}$$

where $h = 6.626 \times 10^{-34}\,J \cdot s$ is the Planck's constant, f_0 is the carrier frequency of the signal being amplified, G is the amplifier gain in linear units and $n_{sp} > 1$ is the spontaneous emission factor or inversion factor. n_{sp} is directed related to the atomic populations in the ground and excited states of the Erbium atoms [65] and specifies the noise performance of an amplifier. From a system perspective, such quantity is often expressed using the noise figure parameter F, that is given by

$$F = 2n_{sp} \tag{2.5}$$

therefore Eq. 2.4 can be expressed as

$$G_{ASE} = hf_0 F(G-1) \tag{2.6}$$

Besides EDFAs, in long-haul optical communications, Raman amplifiers (RAs) , and Hybrid Erbium-Doped and Raman Amplifiers (HFAs) are widely used, as they enable improved noise performance with respect to standard EDFAs. For both of them, it is possible to derive equivalent noise figures to describe the accumulation of ASE noise [51], [65], [73], [74], using Eq. 2.6 to assess noise PSD.

2.4 Modeling filtering penalties and SRS crosstalk

Filtering penalties and SRS-induced crosstalk represents two additional limiting factors to the capacity of transparent and reconfigurable optical networks such as the ones considered in this thesis. Filtering penalties can be relevant as optical channels may traverse multiple ROADMs along their path and thus undergoing bandwidth narrowing causing ISI at the receiver. Modeling such ISI-induced penalty is nontrivial as it depends on many parameters including channel spectral shape, modulation format, DSP receiver structure. For these reasons, in literature, filtering penalties and related compensation strategies are often measured experimentally [56],

[58], [75] on a fixed setup. Among possible compensation strategies for avoid penalties it is worth to mention channel spectral shaping [58], [75], and improved receiver DSP structures [76]. As a general model for filtering penalties is nontrivial to get, in optical networking studies filtering penalties have often been neglected or taken into account in a simplified way, such as imposing a maximum tolerable number of cascaded ROADMs that a signal can traverse [77], or by considering a fixed SNR penalty term for each traversed ROADM. In the networking analysis described in this thesis, filtering penalties will be neglected, unless otherwise explicitly stated.

On the other hand, SRS-induced crosstalk in coherent optical communication systems simply causes an inter-channel power transfer from higher frequency WDM channels to lower ones during propagation along the fiber, leading to a tilt of the overall WDM comb. For standard single mode fibers (SMF), the efficiency of this phenomenon is maximized for optical signals that are placed approximately 13 THz apart [51], but it is already visible for total spectral occupations of the order of few THz, corresponding to WDM comb made of at least 40 channels within the standard 50-GHz DWDM grid. Such power distortion effect can be easily modeled by considering an optical fiber as a filtering block, whose transfer function takes into account both losses and distributed gain/losses due to SRS. This means that given an input WDM comb with a PSD $G_{TX}(f)$, the PSD of the signal at the end of the fiber is given by

$$G(f,z) = G_{TX}(f)|\rho(z,f)|^2 = G_{TX}(f)\rho(z,f)^2 \tag{2.7}$$

where $\rho(z,f)$ represents the field gain/loss profile of the fiber taking into account losses and SRS-induced tilt. The term $\rho(z,f)$ can be estimated experimentally or numerically by solving a set of coupled differential equations in z. Notice that Eq. 2.7 can be used also for systems using Raman amplification [51], [65], [73], [74], in which a distributed gain amplifies the optical channels as they travel through the fiber due the power transfer induced by one or more high frequency and high power pumps approximately 13 THz away from the WDM channel comb. However, in general Raman amplifiers have optimized pump profiles to deliver flat gain [73], such that $\rho(z,f) = \rho(z)$. It should be highlighted that SRS crosstalk is causing frequency-dependent

SNR variations by tilting the signal PSD. For Raman amplifiers, noise addition should also be considered as described in Sec.2.3. However, since SRS is a distributed effect along the fiber longitudinal coordinate z, it must be understood how it affects other distributed effects, such as the nonlinear Kerr effect. Such novel analysis will be described in Sec. 2.7. Before doing so, an overview of the nonlinear Kerr effect will be given.

2.5 Modeling the nonlinear Kerr effect in coherent optical systems

In this thesis we consider wavelength routed optical networks operated with DSP-enabled transceivers and dispersion uncompensated amplified optical links. In this transmission scenario, it has been extensively shown that impairments of fiber propagation due to loss, chromatic dispersion, and Kerr nonlinearity can be *approximated* as a small perturbative additive Gaussian disturbance on any single frequency [71], [78]–[91]. This effect has been called non-linear interference (NLI) . While NLI has, in general, a phase-noise component [87], it was found that, under normal operating conditions, such phase noise has a long correlation [92] so that it can be almost completely compensated by standard receiver phase recovery circuits. This justifies the assumption of modeling NLI as an AWGN. This fundamental results enabled the development of the so-called Gaussian noise models, that are analytical perturbation models for NLI estimation. These models obtain approximate solutions of the nonlinear Manakov Schroedinger equation [51], [52] leveraging on the key simplifying assumption that each WDM channel can be treated as a Gaussian noise spectrally shaped as the signal [71], [86]. This approach to nonlinear modeling was firstly proposed back in 1993 [93] and adapted up to early 2000s [94], [95] to model nonlinear Kerr effect in IMDD systems. Then it was used to achieve the same goal in optical orthogonal frequency division multiplexing (OFDM) systems [96]. At the beginning of 2010s, the same idea was used for coherent optical systems [71], [79], [82], [84], [88]–[91], and the name GN-model was first used in [71].

The GN-model gives a formula to compute the power spectral density of the NLI – the so-called GN-Reference formula [71], [86] – that is a double integral derived from the Manakov Schroedinger equation [97]. Specifically the GN-reference formula is given by

$$G_{NLI}(f) = \frac{16}{27}\gamma^2 \int_{-\infty}^{+\infty}\int_{-\infty}^{+\infty} G_{TX}(f_1)G_{TX}(f_2)G_{TX}(f_1+f_2-f)\cdot \rho_{FWM}(f_1,f_2,f)df_1df_2 \tag{2.8}$$

where $G_{NLI}(f)$ is the nonlinear interference noise PSD in W/Hz at frequency f, evaluated at the end of a transparent[1] fiber span. $G_{TX}(f)$ represents the PSD of the transmitted WDM signal in W/Hz, γ the nonlinear fiber coefficient measured in 1/W/km. $\rho_{FWM}(f_1,f_2,f)$ represents the so-called Four-Wave Mixing (FWM) efficiency [98], i.e.

$$\rho_{FWM}(f_1,f_2,f) = \left|\frac{1-e^{-2\alpha L_s + j4\pi^2\beta_2 L_s(f_1-f)(f_2-f)}}{2\alpha - j4\pi^2\beta_2 L_s(f_1-f)(f_2-f)}\right|^2 \tag{2.9}$$

where α is the fiber field attenuation coefficient in 1/km, L_s is the span length in km, β_2 is the fiber dispersion coefficient in ps/THz/km. Eq. 2.9 is obtained assuming constant fiber loss coefficient vs. frequency, and lumped amplification at the end of the fiber. Later in Sec. 2.7 a generalization of Eq. 2.8 will be proposed, specifically varying the FWM efficiency given by Eq. 2.9 in order to include space and frequency variations of the gain/loss profile of the optical fiber.

Eq. 2.8, for uniform WDM combs – i.e. equal channels shaping and power levels – can be further simplified by normalizing $G_{TX}(f)$ with a power per channel term P_{ch}, yielding a NLI power on the channel at frequency f that can be written as

$$P_{NLI}(f) = \eta_{NLI}(f)P_{ch}^3 \tag{2.10}$$

where η_{NLI} is the so-called NLI efficiency.

[1] We call *transparent* a span in which all fiber and lumped losses (e.g. connector insertion losses) are recovered by amplification at the end of the span.

It should be noted that Eq. 2.8 does not make any assumption relatively to the channel modulation format but states that the NLI noise at any given frequency depends only on the spectral shape of the channels themselves and power levels, i.e. their PSD. Even though it has been highlighted that modulation format slightly affects the generation of NLI [99], [100], this characteristic of Eq. 2.8 allows to decouple QoT estimation and modulation format assignment. Furthermore, it has been widely demonstrated that Eq. 2.8 constitutes an *upper bound* for the PSD of NLI noise [71], [86], [99], therefore it yields moderately *conservative* QoT estimations. The root cause for NLI overestimation is due to the fact that the Gaussian signal assumption is valid *after* few kilometers of propagation. The fact that such assumption is not verified at the beginning of the fiber leads to an overestimation error of G_{NLI}, i.e. in a slight underestimation in QoT.

Eq. 2.8 does not describe how the nonlinear noise accumulates along a set of concatenated fiber spans. To this regard, the GN-model has been proposed into two different forms, i.e. a coherent and an incoherent form respectively. In the coherent GN-model, the GN-reference formula is extended to periodic multi-span link as follows:

$$G_{NLI}^{coh}(f) = \frac{16}{27}\gamma^2 \int_{-\infty}^{+\infty}\int_{-\infty}^{+\infty} G_{TX}(f_1)G_{TX}(f_2)G_{TX}(f_1+f_2-f)\cdot \rho_{FWM}(f_1,f_2,f)\chi(f_1,f_2,f)df_1df_2 \tag{2.11}$$

where $\chi(f_1,f_2,f)$ is the so-called phased array factor as it formally looks like a phased-array antenna radiation diagram [101], specifically

$$\chi(f_1,f_2,f) = \frac{\sin^2(2N_s\pi^2(f_1-f)(f_2-f)\beta_2 L_s)}{\sin^2(2\pi^2(f_1-f)(f_2-f)\beta_2 L_s)} \tag{2.12}$$

where N_s is the number of spans of the multi-span link, assuming all spans to be equal. Eq. 2.12 takes into account the coherent interference occurring at the receivers among the NLI generated in each single span. On the other hand, in the incoherent GN-model the coherent accumulation of NLI is completely neglected, and the NLI generated in each span is *independent* from the NLI generated in the previous ones. With such simplifying assumption, the PSD of the NLI generated at the end of a multi-span link made of N_s span is

simply given by:

$$G_{NLI}^{inc}(f) = \sum_{i=1}^{N_s} G_{NLI,i}(f) \tag{2.13}$$

If the multi-span link is periodic and uniform, i.e. all span being equal, Eq. 2.13 simply becomes:

$$G_{NLI}^{inc}(f) = N_s G_{NLI,i}(f) \tag{2.14}$$

As widely shown in literature [86], both Eq. 2.11 and Eq. 2.13 are upper-bound to NLI. The difference between $G_{NLI}(f)$ evaluated with Eq. 2.11 and Eq. 2.13 is increasing as N_s increase, as the NLI accumulation dictated by Eq. 2.11 is super-linear. Therefore, QoT predictions based on the coherent GN-model are more conservative than incoherent GN-model ones. However, the gap between the two predictions decreases with the increase of the number of channels. These trends are shown in Fig. 2.2 and Fig. 2.3. Consider for example Fig. 2.2 that shows $G_{NLI}(f)$ evaluated at $f = 0$ for a 21 channel system made of 32 GBaud channels with root raised cosine pulse shaping with 15% roll-off propagating over a multi-span system made of 40 spans of 100km SMF fiber with typical parameters as listed in Tab. A.1 with Eq. 2.11 and Eq. 2.13, and normalized with respect to the NLI evaluated generated in the first span. The two curves progressively separate, being up to 1.4 dB apart after 40 spans, i.e. 4000 km. The same gap however reduces to approximately 1 dB when considering full C-band systems. Fig. 2.3 shows the difference between Eq. 2.11 and Eq. 2.13 in dB displayed as a contour plot as function of the number of spans and number of channels. Fixing the span number, increasing the number of channel produces a reduction of the delta between the two versions of the model. For example, considering a 1000km – 10 spans – system, increasing the number of channels from 5 to a 100 produces a 0.6 dB reduction in gap between Eq. 2.11 and Eq. 2.13, moving from 1.3 dB to 0.7 dB.

Eq. 2.8 can also be expressed in many closed forms [86], [97], the most commonly used one is the following:

$$G_{NLI}(0) = \frac{8}{27}\frac{\gamma^2 G_{TX}^3 L_{eff}^2}{\pi|\beta_2|L_{eff,a}}\operatorname{asinh}\left(\frac{\pi^2}{2}|\beta_2|L_{eff,a}B_{ch}^2 N_{ch}^{2\frac{B_{ch}}{\Delta f}}\right) \tag{2.15}$$

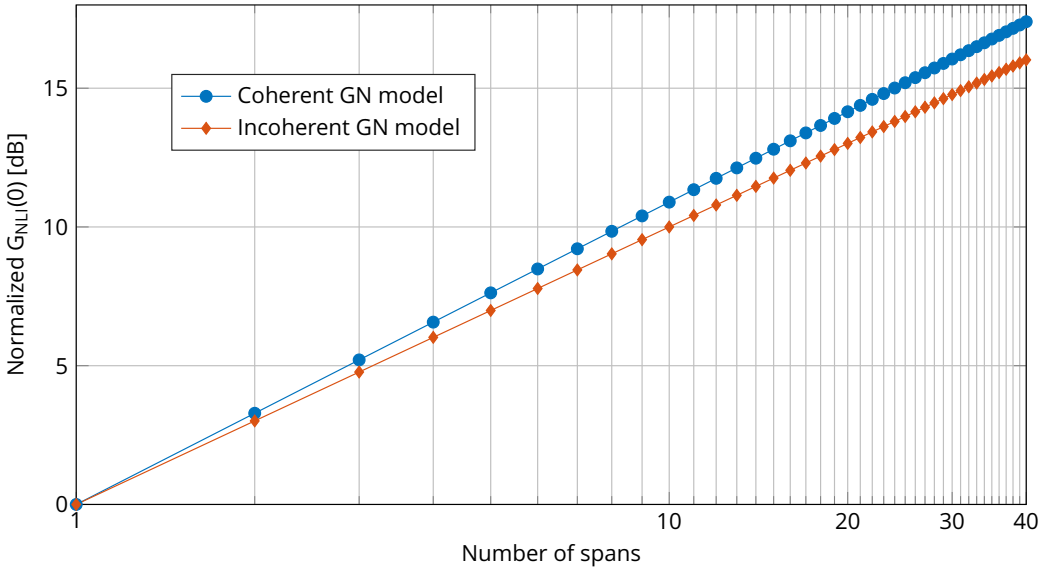

Fig. 2.2 Coherent vs Incoherent Accumulation of NLI for a 21 channel system.

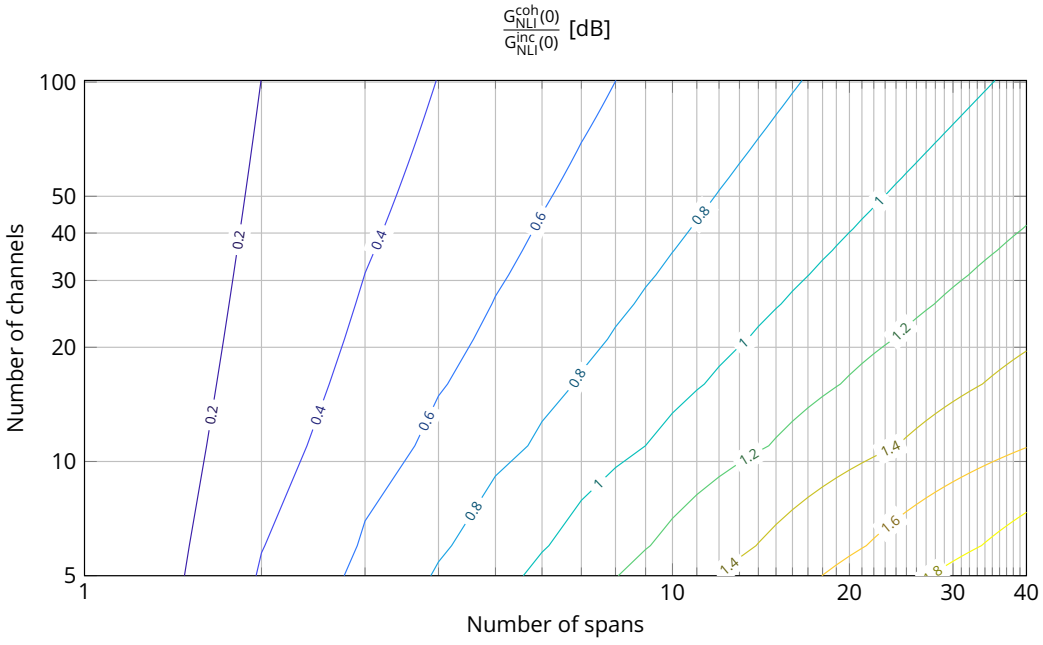

Fig. 2.3 Gap between coherent and incoherent GN-model vs number of spans and number of channels

that represent the amount the PSD of the NLI noise generated at the end of fiber span, at the center frequency of the WDM comb made of equal root-raised cosine channels with 3-dB bandwidth B_{ch}, and maximum (frequency-flat) PSD value given by G_{TX}. L_{eff} represents the fiber effective length, that is given by

$$L_{eff} = \int_0^{L_s} \rho(z, f)^2 dz \tag{2.16}$$

where $\rho(z, f)$ represents the field loss/gain profile at frequency f. Assuming a frequency-flat field loss coefficient α, the effective length can be written as:

$$L_{eff} = \int_0^{L_s} \exp(-2\alpha z) dz = \frac{1 - \exp(-2\alpha L_s)}{2\alpha} \tag{2.17}$$

$L_{eff,a}$ is the asymptotic effective length that is given by:

$$L_{eff,a} = \frac{1}{2\alpha}. \tag{2.18}$$

Closed form expressions for $G_{NLI}(f)$ with $f \neq 0$ are available, specifically Eq. 120 – Eq. 124 in [97].

Several more sophisticated variations to the GN-model have been proposed over the last years. Among this it is worth to mention the Enhanced Gaussian Noise (EGN) model, that improves GN-model predictions by applying a factor to Eq. 2.8 to take into account the non-Gaussianity of the signal at the beginning of the propagation [92], [99], [102]. Specifically, the EGN-model relies on the following equation

$$G_{NLI}^{EGN}(f) = G_{NLI}(f) - G_{corr}(f) \tag{2.19}$$

where $G_{NLI}(f)$ is computed through Eq. 2.8. The correction term $G_{corr}(f)$ depends on the modulation format of the considered channel and its neighbors, and it is – in general – quite elaborated to compute.

Given all the different modeling options based on the signal Gaussianity assumption, it is natural to ask which modeling framework is more suited for physical layer aware networking. This will be addressed in the next section, Sec. 2.8. However, before doing that the bandwidth limitations of these models will be discussed, and the generalized GN-model will be proposed.

2.6 The generalized SNR and related power optimization strategies

As described in Sec. 2.3 and Sec. 2.5, the two most relevant propagation impairments for coherent optical communication systems are ASE noise and NLI, and can be both represented as additive Gaussian disturbances to the transmitted signals. This property led to the definition of the so-called generalized or effective SNR, that is a QoT-metric that includes both ASE and NLI noise. The effective SNR can be written as

$$\mathrm{SNR} = \frac{\mathrm{P_{ch}}}{\mathrm{P_{ASE}} + \mathrm{P_{NLI}}} \tag{2.20}$$

that can be further written as

$$\mathrm{SNR} = \left(\frac{\mathrm{P_{ASE}}}{\mathrm{P_{ch}}} + \frac{\mathrm{P_{NLI}}}{\mathrm{P_{ch}}} \right)^{-1} \tag{2.21}$$

or

$$\mathrm{SNR} = \left(\mathrm{SNR_{LIN}^{-1}} + \mathrm{SNR_{NLI}^{-1}} \right)^{-1} \tag{2.22}$$

that is a scaled version of the harmonic mean of the linear and nonlinear SNR. Considering multi-span link, assuming *incoherent* accumulation of NLI, thanks to Eq. 2.22, the SNR of an optical channel after $\mathrm{N_s}$ spans can be written as

$$\mathrm{SNR} = \left(\sum_{\mathrm{i}=0}^{\mathrm{N_s}} \mathrm{SNR_{LIN,i}^{-1}} + \sum_{\mathrm{i}=0}^{\mathrm{N_s}} \mathrm{SNR_{NLI,i}^{-1}} \right)^{-1} \tag{2.23}$$

Notice that, as $\mathrm{P_{NLI}}$ is a function of $\mathrm{P_{ch}}$, Eq. 2.20 is a non monotonic function of $\mathrm{P_{ch}}$, i.e. a bell-shaped function vs $\mathrm{P_{ch}}$ [103]–[105]. One of such bell-shaped curves is depicted in Fig. 2.4 for 20x100 km SMF spans, followed by EDFA with a 5 dB noise figure carrying 41 PM-QPSK 32 GBaud system over a 50 GHz DWDM grid. These results are obtained from a full split step simulation. From this figure one can derive the optimal power per channel for the considered system, i.e. approximately 0 dBm.

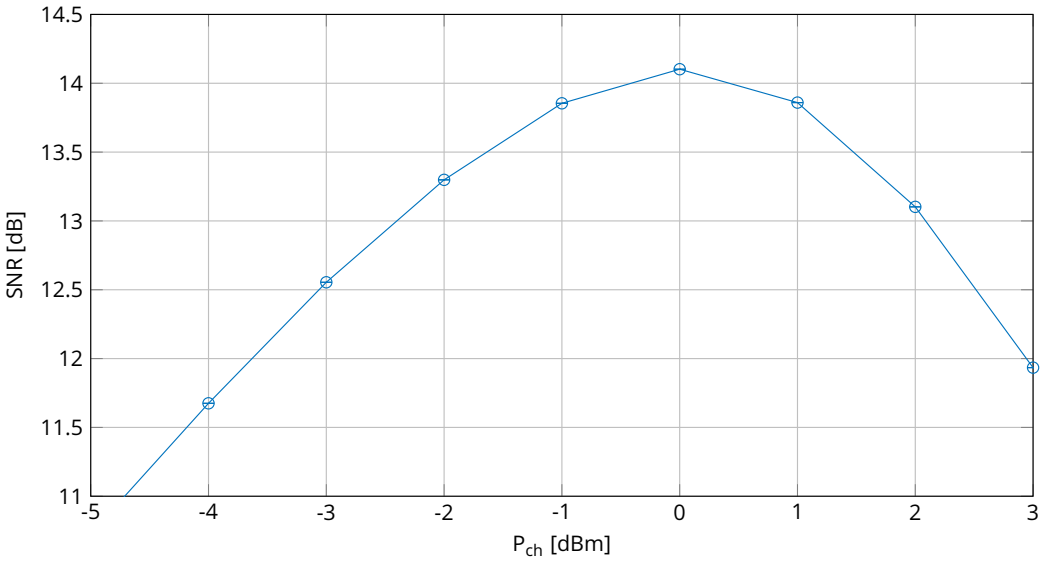

Fig. 2.4 Generalized SNR vs power per channel for a 41 PM-QPSK 32 GBaud system over a 50 GHz DWDM grid. Results are obtained from full split step simulations.

Assuming to model NLI with the GN-model, i.e. plugging Eq. 2.10 into Eq. 2.20, we can write:

$$\mathrm{SNR} = \left(\frac{\mathrm{P_{ASE}}}{\mathrm{P_{ch}}} + \eta_{\mathrm{NLI}} \mathrm{P_{ch}^2} \right)^{-1} \tag{2.24}$$

from which it is easy to derive the optimal power value $\mathrm{P_{ch}^{opt}}$ at the input of a single transparent span that is given by [71], [86], [97], [106]

$$\mathrm{P_{ch}^{opt}} = \sqrt[3]{\frac{\mathrm{P_{ASE}}}{2\eta_{\mathrm{NLI}}}} \tag{2.25}$$

where $\mathrm{P_{ASE}}$ is the ASE noise power generated at the end of the link, and η_{NLI} is the NLI efficiency of the fiber span itself. Due to the dependence on η_{NLI}, $\mathrm{P_{ch}^{opt}}$ is – in general – load dependent. Plugging Eq. 2.25 into 2.20 it can be derived that, according to the GN-model, at optimal power, the linear SNR should be twice as large as the nonlinear SNR [104], [107], [108]. Thus, at optimal QoT conditions, the major contributor to generalized SNR is the linear one. A fundamental consequence of this is that at optimal power, the gap between the generalized SNR and the linear SNR is 1.76 dB, i.e. the generalized SNR is 2/3 of the linear SNR at optimal power.

Considering a multispan link, and assuming incoherent accumulation of NLI and ideal amplifiers, i.e. amplifiers whose noise figure is independent of their gain, Eq. 2.25 holds for any span of the link. In particular, the optimal power at the input of every single span can be derived *independently* from the characteristics of all the other spans of the link, as the optimal power of the span depends only on the NLI and ASE noise generated in that span. This major consideration leaded to the formulation of the so-called Locally-Optimized Globally-Optimized (LOGO) [106], [109] approach. The LOGO principle states that it is possible to globally optimize the QoT of a multi-span link by locally optimize each span of the link. The same approach can be used in an optical networking context, as it is done in this thesis. This will be thoroughly explained in more details in Sec. 2.9.

It should be noted that such simplified approach does not hold if the amplifier noise figure depends on its gain, as a coupling among all the spans building up an optical link will occur, thus increasing the complexity of the optimal power derivation. Even if it is possible to have optical amplifiers that approximate this gain-noise figure independence assumption fairly well, this is not the case for most commercially available EDFAs, as typically the noise figure quickly increases when reducing the gain. When a variable NF is considered, Eq. 2.25 does not hold anymore, and more complex expressions for the optimal launch power can be derived [110]. In this thesis, for sake of simplicity, ideal amplifiers will be always assumed, however, it is worth to mention that the LOGO principle can be extended to more commercially relevant conditions, by applying local optimization at a multi-span link level (ROADM-to-ROADM), and not on a span level (amplifier-to-amplifier) [110]. Therefore the methods proposed in this thesis can be extended to such realistic scenarios, without loss of generality. This being said, in Sec. 2.9 the implications of using a LOGO-based approach for networking studies will be better highlighted, stressing out the strengths and weaknesses of this approach.

2.7 The Generalized GN-model for NLI modeling in wideband systems

As highlighted in Sec. 2.4, SRS-induced power crosstalk is a distributed effect that whose impact on system performance gets worse as the total bandwidth occupation increases. As C+L systems are gaining traction [8], [9], it is important to estimate the interplay between SRS and NLI generation and extend the GN-model to take this into account to further optimize performance. However, before doing that, it is important to understand if the assumptions on which this model is based are valid for wide-band scenarios where NLI and SRS could interact. In Sec. 2.5, nonlinear model based on the Gaussian assumption of NLI have been presented. As stated there, such models rely on the use of the Manakov equation for their derivation. The Manakov equation (ME) [51], [52] is obtained by averaging out random birefringence, neglecting rapidly varying birifringence thus PMD, from the coupled, dual polarization, nonlinear Schroedinger equations (DP-NLSE). This averaging procedure is justified by assuming that the local orientation of birefringence axes is a weak function of frequency. So, formally, results derived from the ME hold only on its limited bandwidth determined by the strength of the PMD itself according to the so-called PMD coherence bandwidth [52], [111], [112] that is given by:

$$B_{coh} = \sqrt{\frac{3}{4\pi^2 \delta_{PMD}^2 L_{eff}}} \tag{2.26}$$

where δ_{PMD} is the fiber PMD coefficient [65] in $ps/\sqrt{km}$, and L_{eff} is the fiber effective length. On the other hand, recent experimental investigations [113], [114] on transmission over bandwidths exceeding the C-band presented measurements of NLI generation scaling logarithmically with the exploited bandwidth as predicted by ME-based models [71], [79], [87], i.e. far beyond the ME validity. However, these experiments used Gaussian-distributed channels, and so such a behavior is theoretically predictable as a 4-dimension Gaussian random process does not modify its statistical properties with rigid rotations of its basis [70]. The impact of PMD over NLI generation when propagating fully modulated non-Gaussian distributed multilevel modulation

formats has been studied in [115] for both dispersion managed and dispersion unmanaged systems. The authors showed that for dispersion managed systems, PMD helped reducing the effect of interchannel nonlinearity generation, while worsening self-channel one. The studies performed in [115] were carried out relying on numerical integration of the Manakov-PMD equation, that is a simplified version of the DP-NLSE for faster numerical simulation of optical systems [52]. However, the studies in [115] did not consider large spectral occupation, considering only up to 9, 28-GBaud channels. Therefore a general assessment of NLI generation in presence of PMD when propagating fully modulated non-Gaussian distributed multilevel modulation formats over wideband systems, and a comparison with ME-based simulations and models is still lacking. In the next subsection, simulative results aimed at giving an assessment of these open problems will be presented.

2.7.1 Assessing the impact of PMD on NLI generation

In order to understand the impact of PMD on NLI generation, we study the scaling of the generalized SNR as a function of the exploited optical bandwidth and different PMD values. To do so, we exploit a MATLAB® based library that we have developed in the OptCom group for solving the ME and DP-NLSE with a Split Step Fourier Method (SSFM) [51] exploiting Graphic Processing Units (GPUs): the fast fiber simulation software (FFSS) library [116]. We do not rely on the Manakov-PMD equation [52] to study the impact of PMD on NLI generation but rather we rely on the DP-NLSE, i.e. the most general mathematical formulation of signal propagation in optical fibers. FFSS library integrates the well-known coarse step method (CSM) [52] to emulate the random birefringence causing PMD into the SSFM for solving the DP-NLSE. Such method approximates the continuous birefringence variations of a realistic fiber by a concatenation of fixed length birefringent sections, each of them characterized by a random orientation of its principal state of polarization (PSP) axis and a given differential group delay (DGD) [52]. In order to avoid resonance effects, we randomized the section length as suggested in [117], [118]. Such polarization variation is integrated into the linear step of SSFM calculation when applying chromatic dispersion and

loss to the signal. This is legit, as the DP-NLSE is given by:

$$\frac{\partial \mathbf{E}(z,\omega)}{\partial z} = -j\bar{\bar{\beta}}(\omega)\mathbf{E}(z,\omega) - \alpha(\omega)\mathbf{E}(z,\omega) + \\ -j\frac{\gamma}{3}\mathfrak{F}\left\{\begin{bmatrix} 3|E_x(z,t)|^2 + 2|E_y(z,t)|^2 & E_x^*(z,t)E_y(z,t) \\ E_y^*(z,t)E_x(z,t) & 3|E_y(z,t)|^2 + 2|E_x(z,t)|^2 \end{bmatrix}\mathbf{E}(z,t)\right\} \tag{2.27}$$

where $\mathbf{E}(z,\omega)$ represents the two components in the angular frequency ω of the optical signal in the chosen orthogonal polarization basis – x and y –, traveling along the fiber longitudinal direction z. $\mathbf{E}(z,t)$ is the optical field in time, and it is given by the inverse Fourier transform $\mathfrak{F}^{-1}\{\mathbf{E}(z,\omega)\}$. $\bar{\bar{\beta}}(\omega)$ represents the dispersion matrix that includes chromatic dispersion and random birefringence inducing PMD. α is the fiber attenuation coefficient, and γ is the non-linear coefficient for the Kerr effect. The right-hand side of Eq. 2.27 can be rewritten as a summation of a two operators applied to the optical field. A linear operator D accounting for dispersion, polarization effects and loss, and a nonlinear one N accounting for the Kerr effect.

$$\frac{\partial \mathbf{E}(z,\omega)}{\partial z} = D(\mathbf{E}(z,\omega)) + \mathfrak{F}\{N(\mathbf{E}(z,t))\} \tag{2.28}$$

N can be applied in the time domain to avoid computing a double convolution in frequency. In the SSFM, Eq. 2.27, is solved by assuming that, over a small distance Δz, the linear and non-linear operators act independently. Thus, at every step Δz the fiber is first assumed completely linear and then nonlinear, hence the D and N operators are applied one after the other. For $\Delta z \to 0$, the solution of SSFM tends to the exact solution of Eq. 2.27.

To properly assess the impact of PMD on NLI generation, the choice of the step size Δz in the SSFM is essential: the step size must be set to the smallest value between the CSM step size needed to correctly emulate PMD [52], and the nonlinear step size that is computed to have a maximum tolerable nonlinear phase shift that was set to $4 \cdot 10^{-4}$ rad. Thanks to signal attenuation during propagation, the nonlinear step size can be adapted vs z. On the other hand, the CSM step size is not adaptive, therefore DP-NLSE-based simulations are much longer than ME-based ones. Furthermore, in order to properly emulate the effect of PMD, Monte Carlo simulations for

different PMD realizations must be considered, making the overall process even more time consuming and challenging. Finally, to properly simulate wideband optical systems in presence of dispersion, the propagated signal is truncated in time to remove all transient effects due to filtering effects including chromatic dispersion. The same effect can be achieved by properly tuning the step size in order to limit the maximum walk-off between two channels at the edge of the simulated spectrum [119].

The setup of the simulated link is depicted in Fig. 2.5. We simulated a 20x100km SMF link, with in-line EDFA amplifiers with 5 dB noise figure fully recovering the fiber loss. The fiber parameters for SMF are reported in Tab. A.1. The system carries up to $N_{ch} = 61$ PM-QPSK or PM-16QAM channels over the standard 50 GHz grid, for a total spectral occupation B_{WDM} close to 3 THz. We consider transmitters generating signals at 32 GBaud, shaped with a root-raised-cosine (RRC) filter with 15% roll-off. At the receiver, we consider the center channel of the WDM comb as channel-under-test (CUT), and apply a polarization and phase diversity coherent receiver. After photodetection and digital conversion, signals are equalized by a fully data-aided LMS adaptive equalizer with 17 taps, and the generalized SNR is evaluated on the equalized constellation. Since lasers are assumed ideal, and we are solely interested on NLI generation assessment [87], no carrier phase estimation (CPE) is performed. Then, the generalized SNR is directly inferred from the signal constellation [66]. The DSP receiver parameters were carefully tuned to properly compensate for linear PMD effects. To do so, we simulated the system of Fig. 2.5 in linear condition, i.e. $\gamma = 0$, for all the analyzed scenarios to match the measured SNR after propagation with the back-to-back one for both ME and DP-NLSE implementations. With the aforementioned parameters, the gap from back-to-back values was found to be smaller than 0.01 dB, proving the considered DSP structure to be sufficiently accurate for linear PMD compensation. This being said, any performance variation in terms of SNR between the ME and DP-NLSE will be solely caused by nonlinear effects and their interaction with PMD.

We simulated propagation relying on the ME or DP-NLSE. For DP-NLSE, we considered two different PMD values: state-of-the-art value of 0.05 $ps/\sqrt{km}$ and a very large value of 1 $ps/\sqrt{km}$. While the first value represents a typical value of modern SMF fibers, the latter is an overly high

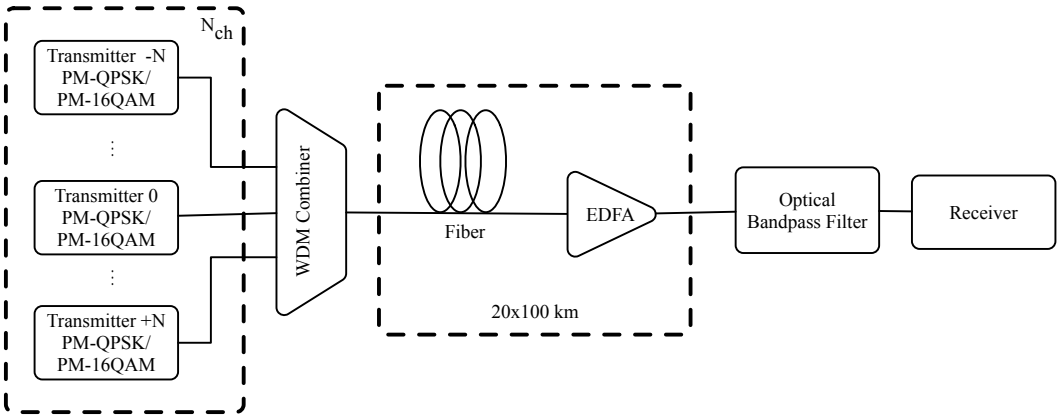

Fig. 2.5 System setup considered for the assessment of PMD impact on NLI generation.

value that we set to have a polarization coherence bandwidth (cf. Eq. 2.26) over the fiber effective length as small as 65 GHz. This was chosen to trigger any possible interaction between PMD and NLI generation out of the ME validity bandwidth, i.e. beyond the limits of NLI generation modeling. For each value of PMD, up to 20 Monte Carlo simulations with different statistical realizations of random birefringence were used. This was enough to estimate a stable standard deviation on the generalized SNR, that resulted to be smaller than 0.03 dB for all the analyzed cases, and so negligible.

We first consider a scenario with $N_{ch} = 41$ corresponding to $B_{WDM} \approx 2$ THz, performing simulations at different power per channel P_{ch} for both PM-QPSK and PM-16QAM scenario. The corresponding generalized SNR vs P_{ch}, comparing results obtained from the ME, DP-NLSE with the two different PMD values, and GN-model predictions are displayed in Fig. 2.6. As expected, GN-model predictions are conservative with an SNR underestimation slightly higher for PM-QPSK with respect to PM-16QAM: 0.6 dB vs. 0.5 dB. The most interesting aspects of novelties in Fig. 2.6 lie in comparing ME results with DP-NLSE ones. While at low P_{ch}, where performance is ASE-limited, all three cases give the same SNR, increasing P_{ch}, DP-NLSE results shows a *slight* decrease in SNR with respect to ME-results. This suggests that PMD slightly increase the power of generated NLI noise. At optimal power, $P_{ch}^{opt} \approx 0$ dBm, the SNR difference between ME and DP-NLSE with $\delta_{PMD} = 0.1$ ps/$\sqrt{\text{km}}$ is 0.21 dB for PM-QPSK and 0.13 dB for PM-16QAM. From a practical point of view, we observe that NLI generation happens

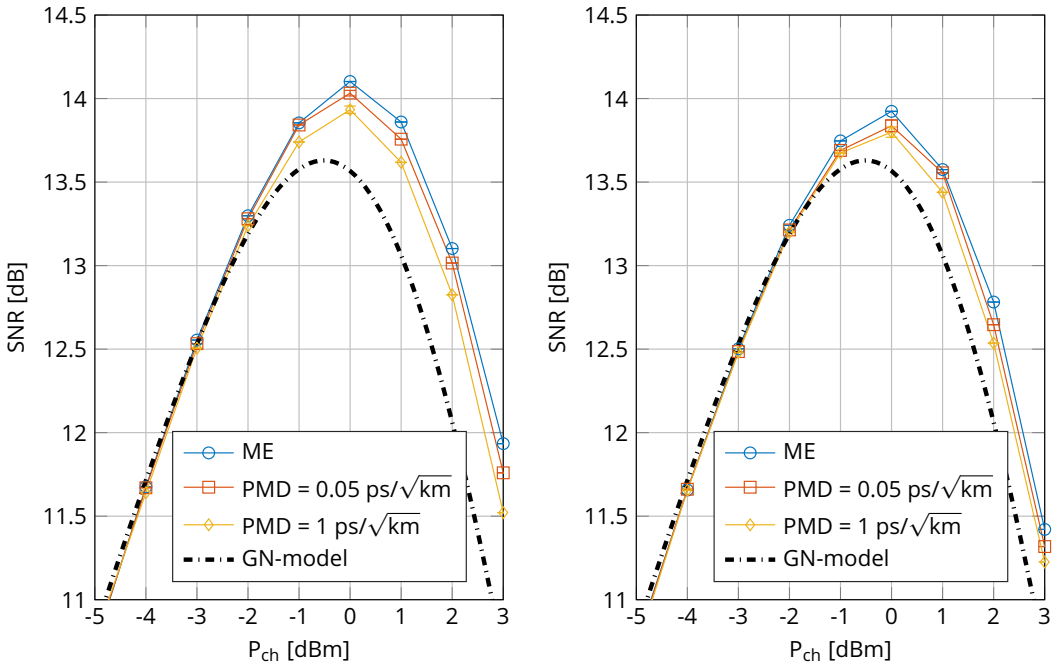

(a) PM-QPSK (b) 16-QAM

Fig. 2.6 Generalized SNR for PM-QPSK and PM-16QAM for different values of PMD in a system with 41 32-GBaud WDM channels in a 50 GHz grid, and comparison with GN-model predictions

also far beyond the ME validity bandwidth, and that presence of PMD only slightly closes the gap between actual performances and GN-model predictions. A possible explanation is that the PMD adds signal distortion on top of the one induced by chromatic dispersion, thus enabling GN-model-predicted results at shorter distances. To verify this possible explanation, we run a numerical simulation over a PMD-only fiber, i.e. an optical fiber without attenuation, dispersion and Kerr effect. The simulation was run over 23 km of fiber, which corresponds approximately to the effective length of SMF. We then measured the signal histograms before and after propagation. As a modulated signal is a cyclo-stationary random process [120], with periodicity equal to the symbol rate, one needs to create several histograms of the signal at different time instants inside a symbol, obtaining a result very similar to an eye diagram. Results obtained considering 20,000 symbols are shown in Fig. 2.7. For this simulation, PMD has been further increased to a very large value of 5 ps/$\sqrt{\text{km}}$ to exacerbate the PMD-induced signal distortion, and allow a *qualitative* inspection of the eye-diagram. As seen in the figure, after 23

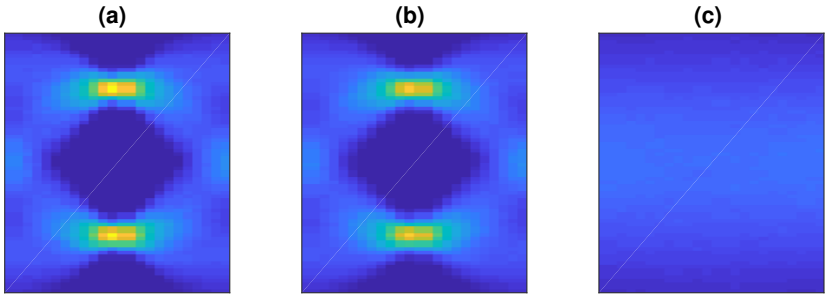

Fig. 2.7 Eye-diagram of a 32-GBaud PM-QPSK signal before (a) and after 23 km propagation on a PMD-only fiber (b) and a CD-only fiber (c).

km PMD "scrambles" the signal making it closer to be Gaussian-distributed. Thus PMD assists CD in "Gaussianizing" the signal, enabling the generation of slightly additional NLI.

To understand the scaling of this effect with the total optical bandwidth of the system B_{WDM}, we performed simulations at constant power $P_{ch} = 0$ dBm varying the number of channels N_{ch} from 11 to 61. Results are depicted in Fig. 2.8, and shows that NLI generation is slightly affected by PMD even at larger bandwidth occupation, but no relevant variations vs B_{WDM} can be observed. It should also be noticed that the generalized SNR scales logarithmically with bandwidth as predicted by many NLI prediction models [71], [87].

From a practical perspective, these results show that PMD has *negligible* effects over NLI generation *independently* from optical bandwidth occupation. Thus this allows to (i) simulate propagation effects in optical systems carrying polarization-multiplexed multi-level modulation formats through the ME, (ii) scale ME-based models for NLI estimation well-beyond ME bandwidth validity. Therefore this latter result allows us to generalize an ME-based model such as the GN-model, to take into account propagation impairments that are triggered by large bandwidth occupation, such as SRS-induced power crosstalk.

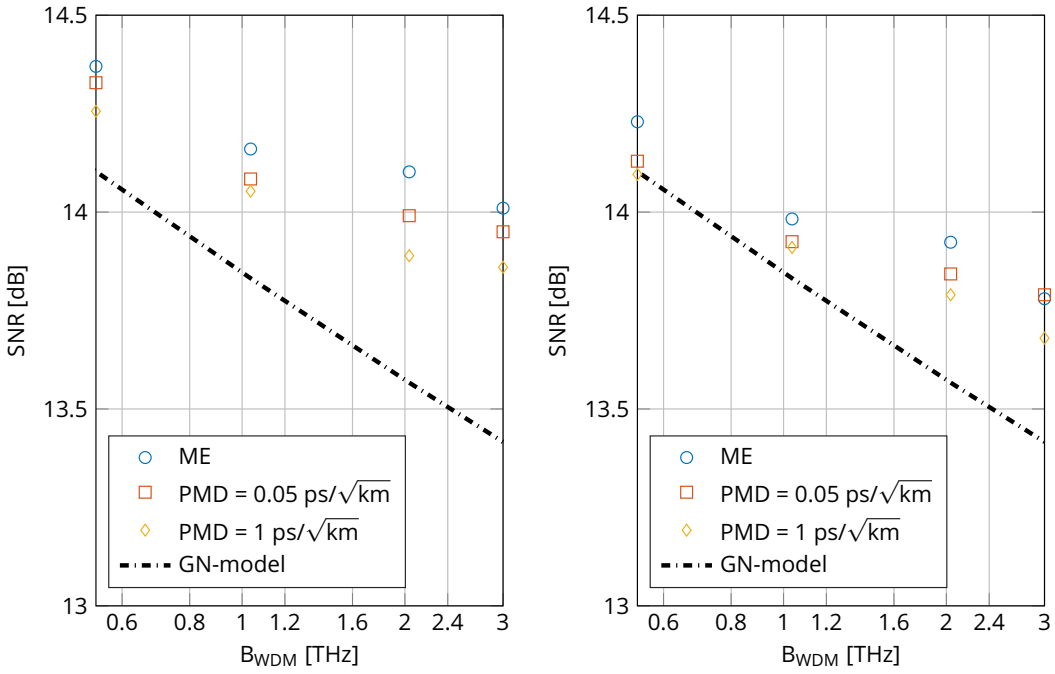

(a) PM-QPSK (b) 16-QAM

Fig. 2.8 Generalized SNR for PM-QPSK and PM-16QAM vs. number of channels, and comparison with GN-model predictions.

2.7.2 Introducing the Generalized Gaussian Noise Model

The Generalized GN-model (GGN) model was firstly proposed in [121] and later in [122] to include in the GN-model spatial and frequency power variations along the fiber. The impact of such generic spatially and frequency distributed loss/gain profiles along the fiber on NLI generation is of special interest when considering full C-band and beyond systems, as SRS-induced inter-channel power crosstalk is not negligible in such transmission scenarios. Specifically, as the optical signal travels through the fiber, a power transfer from higher to lower-frequency spectral components takes place, yielding the well known SRS-induced tilt. For silica-core single-mode fibers, the efficiency of this phenomenon is maximized for optical signals that are placed approximately 13 THz apart, but it is already visible for total spectral occupations of the order of few THz, corresponding to WDM comb made of at least 40 channels within the standard 50-GHz DWDM grid. Similar spectral distortion effects can be caused by poorly optimized Raman am-

plified links, where different frequencies undergo different Raman gains, yielding a distortion of the transmitted optical spectrum during propagation. As described in Sec. 2.4, these phenomena can be well described by a field loss/field amplitude profile, function of both space and frequency, $\rho(z, f)$.

To study the interplay between these power-variation phenomena and NLI generation we extend the GN-model as follows. Starting from the GN-model derivation [97], we generalize its formulation considering a generic gain/loss profile $\rho(z, f)$ for the optical field, that is a function of both the fiber spatial coordinate z and frequency f. A similar problem has been addressed in [63], where the authors proxies the impact of $\rho(z, f)$ on NLI by introducing a frequency-dependent effective length used to scale the amount of NLI generated by a fiber having a frequency-flat loss profile. This strategy represents a relatively simple engineering approach to propagation impairment modeling, but it ultimately lacks in precision as it will be described later in Sec. 2.7.4 since the impact of $\rho(z, f)$ over the Four-Wave Mixing (FWM) efficiency is neglected. The full derivation of the GGN-model is presented in App. B. The main result of this, is what we define as the GGN reference formula, describing the power spectral density of the NLI at frequency f at the end of a fiber of length L_s, before amplification, i.e.

$$\begin{aligned} G_{NLI}(L_s, f) = & \frac{16}{27}\gamma^2 \rho(z, f)^2 \iint_{-\infty}^{+\infty} G_{TX}(f_1) G_{TX}(f_2) G_{TX}(f_1 + f_2 - f) \\ & \left| \int_0^{L_s} \exp(+j4\pi^2 (f_1 - f)(f_2 - f)[\beta_2 + \pi\beta_3(f_1 + f_2)]\zeta) \cdot \right. \\ & \left. \frac{\rho(\zeta, f_1)\rho(\zeta, f_1 + f_2 - f)\rho(\zeta, f_2)}{\rho(\zeta, f)} d\zeta \right|^2 df_1 df_2 \end{aligned} \tag{2.29}$$

where $G_{TX}(f)$ is the PSD of the transmitted signal at frequency f, β_2 and β_3 are the dispersion parameters of the fiber. The key differentiating element in the GGN-model equation with respect to the GN-model is the expression of the FWM efficiency, that in Eq. 2.29 is expressed by the absolute square of the inner spatial integral made by the product of a phase matching condition with a term expressing the amplitude profile at the different frequencies $(f, f_1, f_2, f_1 + f_2 - f)$ referenced in the outer integrals. Eq. 2.29 can be integrated numerically in few minutes over a standard CPU.

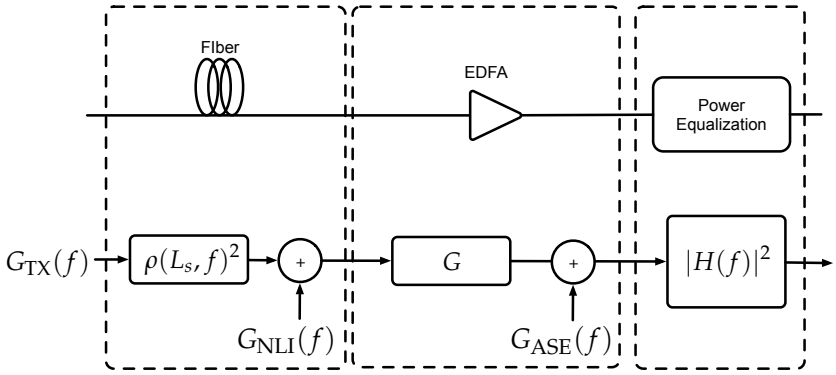

Fig. 2.9 Equivalent block scheme of a fiber span for generalized SNR calculations using Gaussian-noise models.

Similarly to the incoherent GN-model described in Sec. 2.5, Eq. 2.29 can be used to estimate the total amount of NLI of multi-span links by incoherently adding every single contribution of each span in the link. To this purpose, it is useful to describe a fiber span made of an optical fiber followed by an amplifier and eventually a filter for power equalization, using the equivalent block scheme of Fig. 2.9. The optical fiber is represented by a filtering block accounting for both SRS-induced tilt and fiber loss, followed by an NLI addition block. Thus, each fiber is modeled as a block attenuating the input signal PSD $G_{TX}(f)$ by a factor $\rho(L_s,f)^2$, followed by NLI addition. The PSD of this NLI source $G_{NLI}(f)$ is given by Eq. 2.29. The amplification stage is modeled by a gain block with gain G followed by ASE noise addition. We define the PSD of ASE noise as G_{ASE}. If span transparency is assumed, the amplifier has a gain equal to the fiber nominal loss, i.e. in dB $G_{dB} = \alpha_{dB} L_s$, where α_{dB} is the fiber attenuation coefficient in dB/km. All frequency-dependent characteristics of the amplifier such as gain ripple and tilt are not considered for sake of simplicity, but they can be easily integrated into this block model. Finally, the optional power equalization stage is modeled as a filter with transfer function $H(f)$. If such filter recovers the ratio between the fiber transfer function $\rho(Ls,f)^2$ and its nominal loss, then $|H(f)|^2 = (10^{-\alpha_{dB}\frac{L_s}{10}})\rho(L_s,f)^{-2}$. In the next paragraphs, the experimental validation of the GGN-model using commercial transceivers will be discussed.

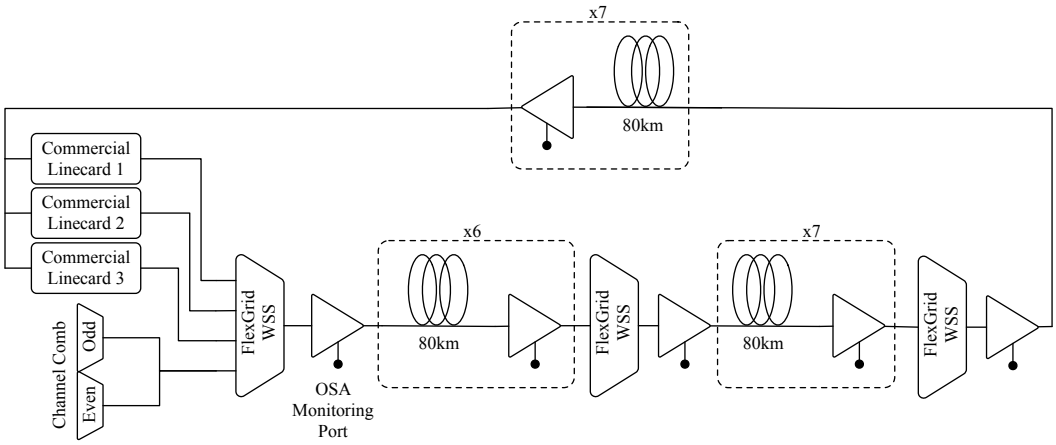

Fig. 2.10 Orange Lab testbed and setup used for experimental validation of the GGN-model.

2.7.3 Experimental Validation of the GGN-model

The validation of the GGN-model was performed over the Orange laboratory testbed, depicted in Fig. 2.10. The testbed consists of 20 spans of 80-km Corning SMF-28e+® optical fiber and is typically used for the performance evaluation of the transponders deployed in Orange networks. A total of 58 channels were configured, 3 of them being current 32-Gbaud 100-Gb/s PM-QPSK commercial transponders. The remaining 55 channels are generated from a comb of lasers modulated by two 28 GBaud 100-Gb/s PM-QPSK laboratory transmitters to modulate the odd and even interfering channels. A Wavelength-Selective Switch (WSS) is used to combine the channel comb with the commercial transponders over the standard 50 GHz Dense WDM (DWDM) grid and 2 additional equalizers are used during transmission every 6 span to equalize the propagating spectrum. No amplifier pre-tilt or WSS pre-emphasis is applied for the measurements reported in this section.

Real-time measurements of pre-Forward Error Correction (FEC) Q-factor were performed with the commercial 32-GBaud transponders. The Q factor was measured by tuning the transponder over the 6 following frequencies [192.95; 193.35; 193.65; 194.00; 194.35; 194.75] THz so that the effect of SRS-induced tilting on system performance is characterized across the C band. In order to map the measured Q-values to the generalized SNR, the transponder back-to-back response was characterized for each of the 6 frequencies under

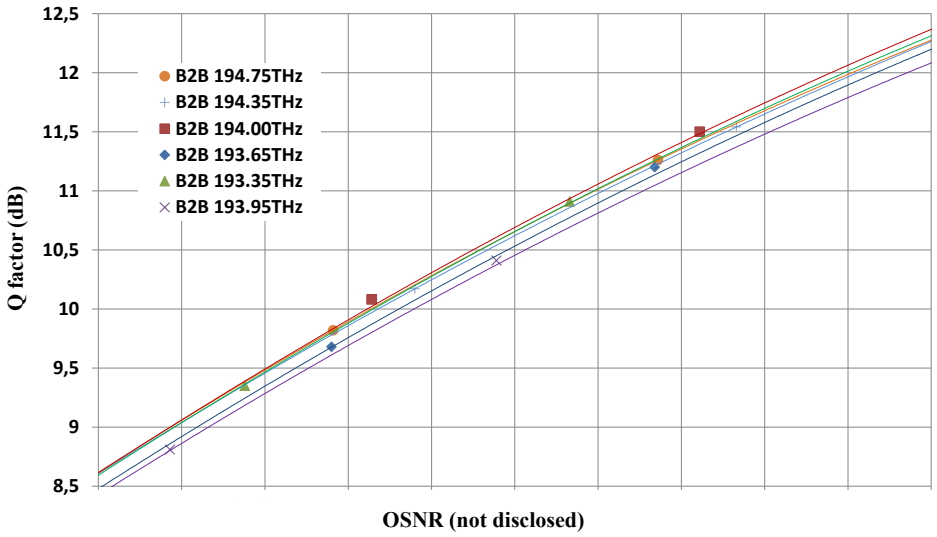

Fig. 2.11 Back to back (B2B) Q vs OSNR response of the transponder for all measured frequencies. Actual OSNR values not disclosed.

test (Fig. 2.11) at a constant received power of −17 dBm. Back-to-Back responses are shown in Fig. 2.11, where the Q-factor is plotted vs OSNR. OSNR data are not disclosed due to nondisclosure agreements with the manufacturer of the commercial transponders. Even though the same transponder was used by tuning its frequency, a significant difference (up to 0.5 dB in OSNR) in back-to-back response across the C-band was recorded. Such unexpected difference is probably caused by inaccuracies in the manufacturing process causing a physical response vs frequency of the components of the commercial cards. This emphasizes the need for a well-calibrated experimental setup when assessing performance variation due to propagation impairments over different frequencies.

The full, 58 channels WDM comb was propagated over the 20×80 km link, and the channel power excursions were recorded before each span at the amplifier monitoring port using an Optical Spectrum Analyzer (OSA). Variations in power levels are reported in Fig. 2.12. The nominal channel launch power was 0.4 dBm, corresponding to a total 18 dBm at the output of the amplifiers. The power per channels of the 58 channels along the first 6 spans is reported in Fig. 2.12a. SRS-induced tilt is clearly visible as a linear tilt (in dB) from higher to lower frequencies. Accumulation of amplifiers' ripple is also clearly visible at low and high frequencies, superimposed to

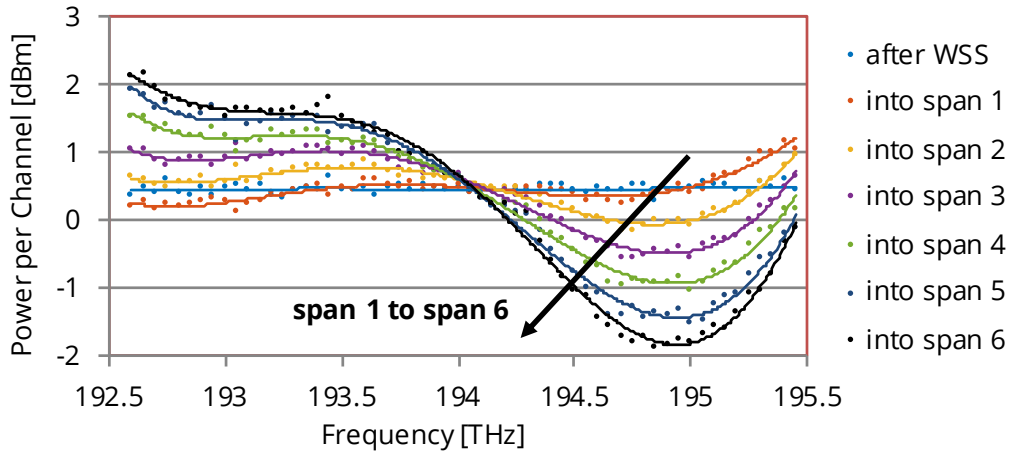

(a) Channels power excursion for the first 6 spans over the Orange testbed.

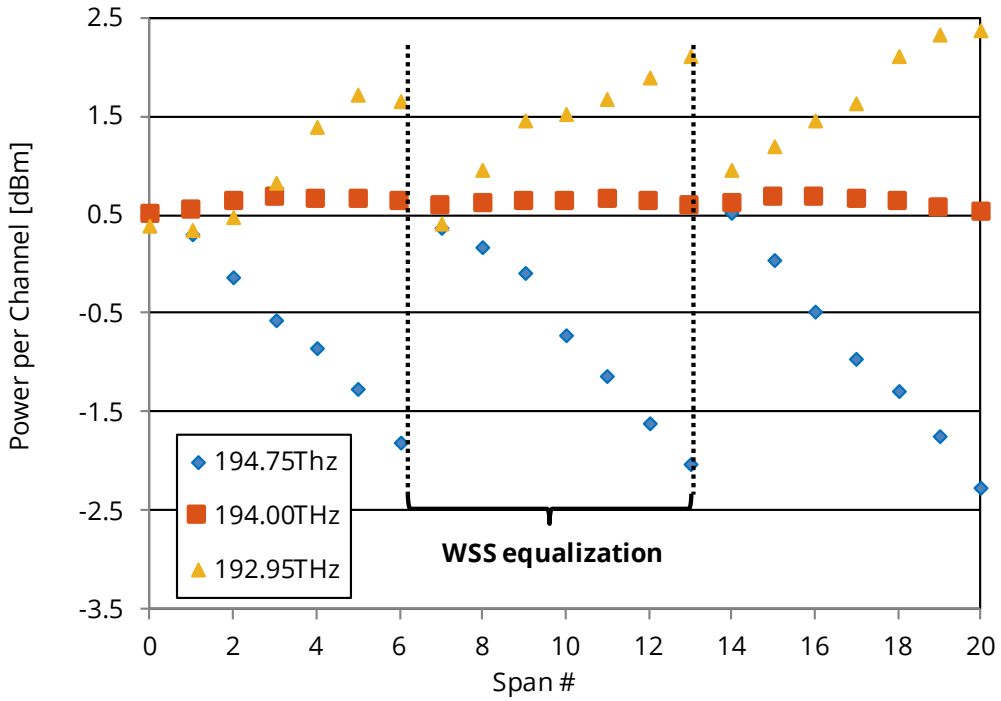

(b) Power per channel evolution for three channels (blue, green and red) at the beginning of each span of the Orange testbed.

Fig. 2.12 Power evolution due to SRS and amplifier ripple along the testbed.

SRS-induced tilt. The power variations for 3 of the 6 channels under test along the whole link are displayed in Fig 2.12b: SRS-induced power transfer from higher to lower frequencies is evident.

The measured Q values after propagation were mapped to generalized SNR, exploiting the back-to-back characterization of transceivers, assuming no nonlinear and dispersion penalties in the DSP implementations of the linecards. In order to extract nonlinear SNR measurements from the generalized SNR ones, the inverse linear SNR that considers ASE noise only was subtracted from the inverse generalized SNR. The linear SNR was directly measured with an OSA at the receivers. The resulting generalized SNR, nonlinear and linear SNR are reported in Fig. 2.13a. All values are scaled over the symbol rate of the channels under test. Values of nonlinear SNR show that higher frequency channels benefit from SRS-induced power depletion, which reduces the amount of generated NLI. The opposite happens with lower-frequency channels. The central channels are the best performing ones, even though they do not respect the optimality conditions derived in Sec. 2.6 as the linear SNR is not 3 dB higher than nonlinear SNR. This highlights the need for modeling frameworks as the GGN-model, taking into account distributed power distortion along the fiber in the nonlinear SNR calculation, to derive new and more general power optimization strategies to be applied across the full optical bandwidth.

The experimental measurements for nonlinear SNR were then compared to the ones obtained using the GGN-model. The comparison is shown in Fig. 2.13b. For this comparison we used datasheet fiber parameters for Corning SMF-28e+®, as reported in Tab. A.1. In order to take into account the strong ripple effects exhibited by the line amplifiers, we plugged into Eq. 2.29 the exact PSD levels launched at the beginning of each span derived from OSA measurements. The measured power profiles were also used to numerically estimate SRS crosstalk, deriving $\rho(L_s, f)^2$ for each span starting from the well-known pump-and-probe equations describing SRS [51]. The estimated SRS tilt is well matched with the experimental data. A major unknown for the experimental validation is represented by the connector loss of the fiber connectors. As an experimental characterization is not feasible, we used typical connector loss values in the range 0.5 to 1 dB, and we selected the value giving the best results. Such value was found to be

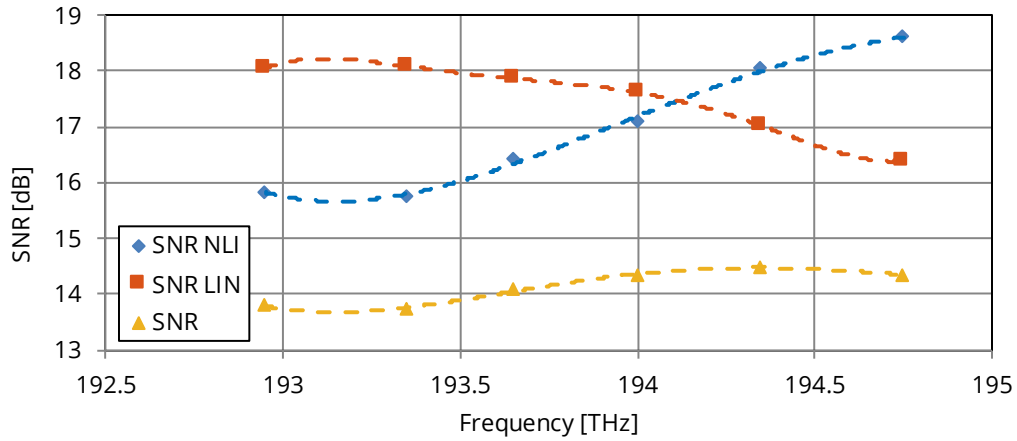

(a) Experimental linear, nonlinear and generalized SNR for the 6 measured frequencies with commercial transponders of the Orange testbed.

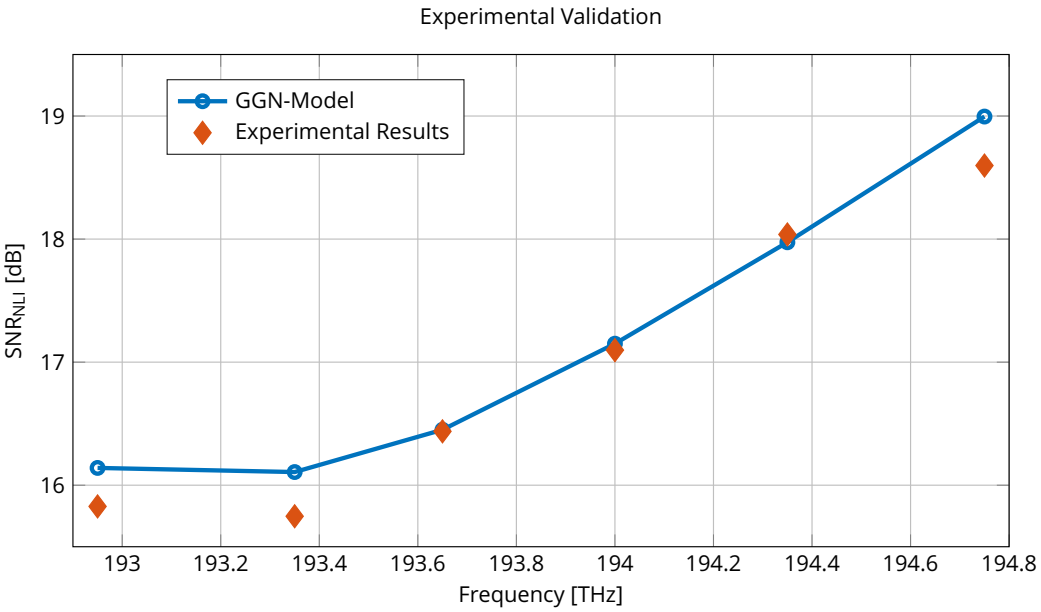

(b) Comparison of experimental and GGN-modeled nonlinear SNR. 0.75 dB fiber connector loss is assumed.

Fig. 2.13 Experimental results for the GGN-model validation. Fig. 2.13a shows the linear, nonlinear and generalized SNR values obtained from experimental data. Fig. 2.13b depicts the comparison of the GGN-model with the experimental nonlinear SNR values.

0.75-dB. Results obtained with Eq. 2.29 are represented in the blue curve of Fig. 2.13b. For all channels, estimation errors are smaller than 0.5 dB, and, more importantly, the slope of the nonlinear SNR is well matched to the experimental results. The average error across the different channels is smaller than 0.3 dB. Therefore the GGN-model is correct in predicting how NLI generation is influenced by SRS and can be used to estimate system performance of wide and ultra-wide-band optical systems.

2.7.4 Comparing the GGN-model with the GN-model

In this section we compare different simplified engineering approaches to model NLI in presence of SRS, showing how the GGN-model represents the best option among these approaches in terms of accuracy across the WDM band. We consider four different modeling approaches and compare their outcome with the nonlinear SNR experimental measurements described in the previous section. For this comparison, we do not exploit the exactly measured power profiles, but we just consider the nominal launch power value i.e. 0.4 dBm plus a 0.75 dB connector loss. We purposely apply this assumption to test the validity of these models in the context of network operations, where only nominal channel power values are often accessible. To relax a little bit such limitation, we consider a ± 0.5 dB region around the experimental results as a region of goodness for the modeling estimations: if estimations fall inside this region, they should be considered good.

The following modeling options are tested:

(i) The Incoherent Gaussian Noise Model, i.e. Eq. 2.13 without considering the SRS-induced power crosstalk. This is equivalent to use the block scheme of Fig. 2.9 with $\rho(z, f)^2 = \rho(z)^2 = \exp(-2\alpha z)$;

(ii) The Incoherent Gaussian Noise Model with SRS tilting, i.e. assuming at the beginning of each span a power profile that has been tilted due to SRS. This is equivalent to applying the block scheme of Fig. 2.9 estimating $G_{NLI}(f)$ via Eq. 2.13;

(iii) Analytical Incoherent Gaussian Noise model with frequency-dependent effective length. Similarly to what is done in [63], we consider closed-

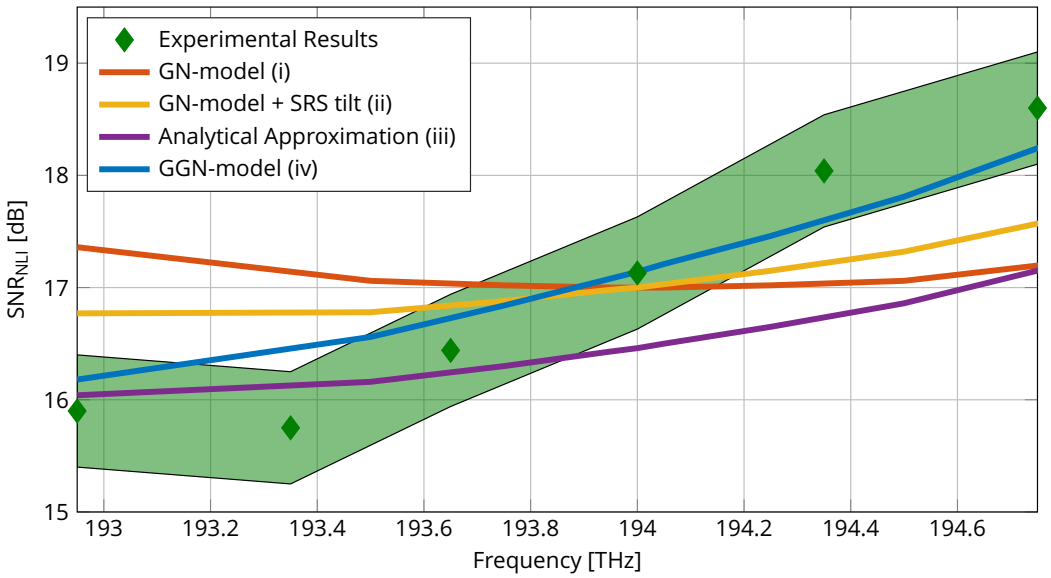

Fig. 2.14 Comparison of different approaches to NLI and SRS interplay modeling.

form expression for the GN-model (Eq. 120 – Eq. 124 in [97]) using a frequency-dependent effective length obtained by numerical integration of $\rho(z, f)$ to couple NLI generation and SRS. Effective lengths associated with the lowest and highest frequency channels have been found to vary from 22.6 km and 21.9 km respectively.

(iv) The GGN-model, i.e. Eq. 2.29.

Results are reported in Fig. 2.14. Considering Fig. 2.14, it can be seen that all different modeling options besides the analytical approximation (iii) well match the experimental nonlinear SNR of the center channel. However, across the WDM spectrum, the slope of the nonlinear SNR is well-matched only by the GGN-model (iv). Focusing on the first approach, i.e. the incoherent GN-model (i) depicted with the orange curve, the small estimation error over the center channel (<0.2 dB) is not replicated over the side channels, where large (>1.4 dB) under/overestimations are obtained for high/low-frequency channels respectively. This approach delivers results falling in the $\pm$ 0.5 dB region only at the center channel. The second approach depicted with the yellow curve, slightly improve the estimation errors: 0.6 dB for high frequency channels, and 0.9 dB for lower frequency ones, but, yet again, the overlap with the shaded region is limited to the central portion of the spec-

trum. The third method that includes effective length variations vs channel frequency is represented by the purple curve in Fig. 2.14. This approach yields very good agreement for lower frequency channels with errors smaller than 0.4 dB, as estimations fall inside the green-shaded $\pm$0.5 dB validity region. These accuracy levels are however not met at higher frequencies were the error grows up to 0.95 dB, and the overlap is lost. On the other hand, the GGN-model (blue curve) yields good approximation of the nonlinear SNR across the full WDM spectrum, with prediction inaccuracies that are smaller than 0.3 dB for all channels but channel at 193.35 THz, where amplifier ripple is clearly visible yielding a 0.6 dB error, corresponding to a small spectral interval of non overlap between the $\pm$0.5 dB region and the estimation curve. Better accuracy can be obtained by considering accurate power level estimations across the full channel comb. However, for this aspect to be feasible, monitoring interfaces of commercial devices should be improved to allow more precise measurements and easier gathering of useful system parameters. These aspects will be further elaborated in Ch. 4, where further comparisons of nonlinear models with commercial equipment will be described.

These results show how common engineering approaches fail to reliable estimate NLI generated on side channels due to the interplay between SRS and NLI generation. The GGN-model, on the other hand, overcomes such limitation, achieving good NLI estimation across the full WDM band, even by operating it only with the knowledge of the nominal power levels of the channels. In the next section, an example of application of the GGN-model will be described, testing different power tilt profiles to equalize the generalized SNR of a WDM comb of a full C-band system.

2.7.5 An example of application of the GGN-model.

In this section, an example of application of the GGN-model is presented. Specifically, we show how the GGN-model can be used to assess the impact of power pre-emphasis through amplifier tilting on channel performance in wide-band optical communication systems. This effort is motivated by the fact that experimental measurements performed over the Orange testbed described in Sec. 2.7.3 showed an improvement in channel SNR when ap-

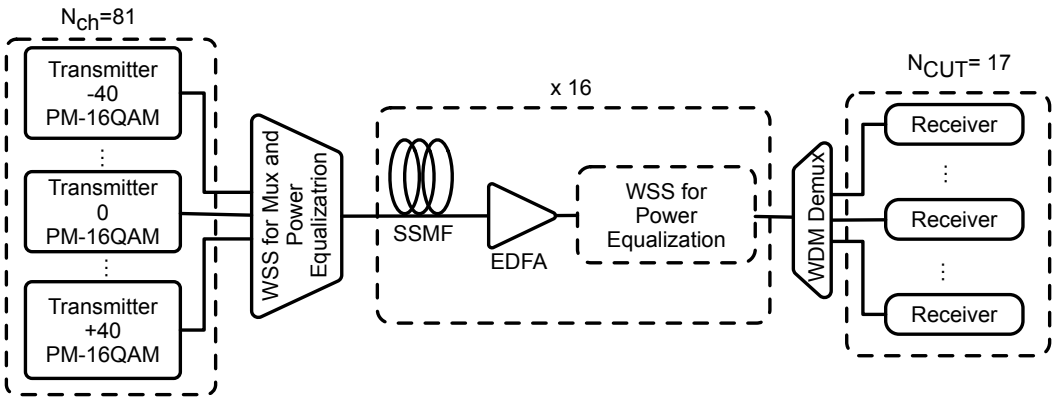

Fig. 2.15 System setup for the GGN-model example of application.

plying power pre-emphasis via amplifier tilting. Specifically, a -1.2 dB tilt showed up to 0.3 dB gain in SNR, even though amplifiers ripple gets worse as the gain is non-flat anymore. Starting from this preliminary qualitative results, we used the model to test the effectiveness of pre-tilt with respect to generalized SNR improvement. For this task, we do not aim at achieving global optimality across the full WDM comb as done for example in [123], but we aim at showing that the GGN model can be a starting point to achieve this.

We modeled a system made of 81 WDM channels, each modulated with a PM-16QAM signal at 32 GBaud with raised cosine spectra with 15% roll-off, and transmitted over 16 100-km spans of standard SMF, with typical fiber parameters as reported in Tab. A.1. The channels are spaced on the standard DWDM grid (50 GHz), obtaining a total modulated optical bandwidth of $B_{WDM} \approx 4$ THz (full C-band). The nominal launch power per channel is -0.8 dBm. At the end of each span, an EDFA with noise factor $F = 5$ dB fully recovers span loss and applies a tilt to counteract the effect of SRS. EDFAs are assumed to have flat gain, thus no gain ripple is considered. Every 4 span a WSS equalizes the power of each WDM channel.

At first, we calculated the power profile spatial evolution before each WSS caused by SRS crosstalk of the full WDM spectrum without any EDFA gain tilting. To do so, we solved numerically the pump-and-probe coupled equations [51] for SRS. After 4 spans, the SRS-induced tilting was of the order of 2 dB. We considered this measurement as the baseline reference

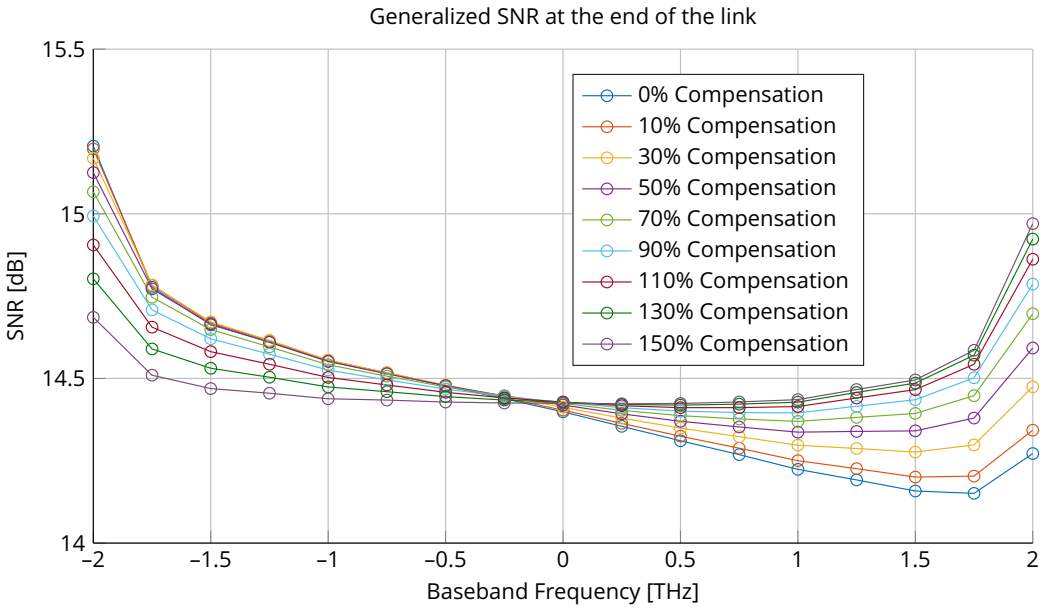

Fig. 2.16 SNR vs pre-compensation percentage. Results obtained with the GGN-model.

to compute tilt profiles for compensation. Then, we considered different percentages of the inverse of this tilt deriving different profiles to test. Each profile was equally distributed across every EDFA in between two WSS. For instance, 0% pre-compensation means that the EDFA gain profile is flat and the SRS-induced tilting is compensated only at each WSS. On the other end, 100% pre-compensation means that each EDFAs pre-compensate 25% of the overall SRS tilting, obtaining an almost flat power profile at the beginning of each WSS.

On Fig. 2.16 we show the generalized SNR of 17 WDM channels equally spaced across the total WDM comb, with different levels of pre-compensation, estimated with the GGN-model. It can be noted that with no compensation, the generalized SNR shows approximately a 1 dB tilt in SNR. As pre-compensation is applied, the SNR tilt reduces: lower frequency channels undergo a decrease in generalized SNR, whereas higher frequency ones an improvement. At 90% compensation, a 0.3 dB improvement in the worst SNR channel is achieved. At 150% pre-compensation, i.e. with a 50% over-compensation, overall SNR flatness is reached, but there is a slight decrease in minimum SNR with respect to the 130% case.

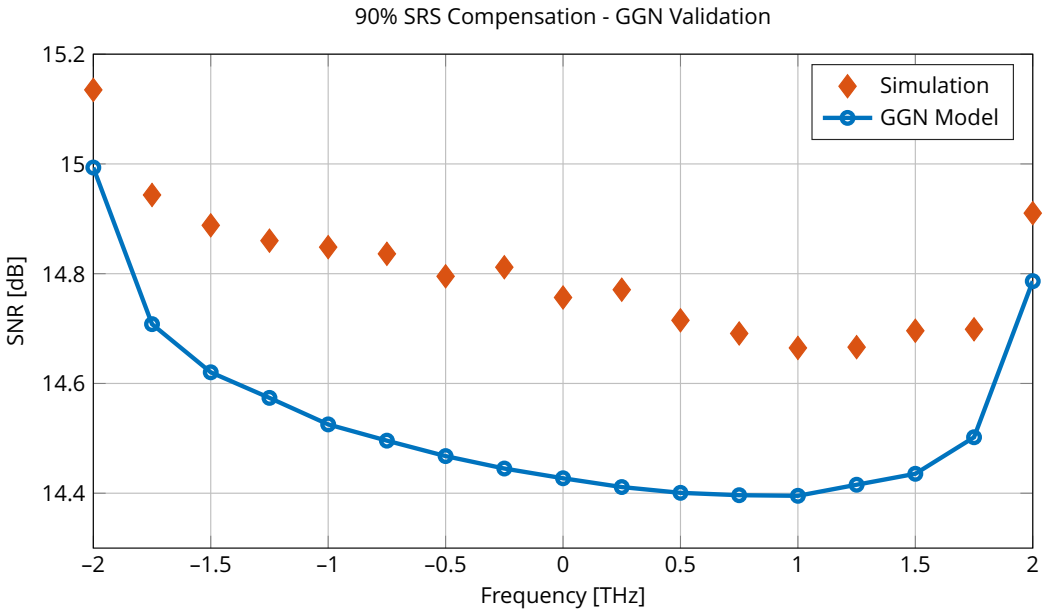

Fig. 2.17 Comparison between the GGN-model and a full split-step simulation for 90% pre-compensation.

In order to better isolate the effect of SRS on NLI generation, we compared GGN-model based estimations against simulative results obtained through FFSS [116]. In order to simulate SRS, we modified the SSFM of FFSS by introducing, in each linear step a non-flat gain/loss profile to be applied to the optical field. Such profile is obtained by solving the pump and probe equations for SRS [51]. This approach represents a simplified way of taking into account SRS into an SSFM based simulator, as it neglects all time-dependent related SRS effects such as cross-gain modulation and relative intensity noise transfer. Such assumption is however reasonable, considering that time-dependent SRS effects can be well-modeled with an equivalent noise transfer from high frequencies to lower ones. The characteristics of such transfer are governed by a low-pass transfer function with corner frequency much smaller than 500 MHz, as chromatic dispersion averages out higher frequencies. Thus, for channels with optical bandwidths much larger than such frequency value, as modern coherent raised cosine shaped optical systems, the additional impairment is irrelevant [124], [125].

As validating the full set of results of Fig. 2.16 would have been excessively time-consuming, we focused on simulating through FFSS a 90%

pre-compensation equally distributed across every EDFA. The 17 WDM channels-under-test (CUT) were generated with 12 repetitions of different 2^{14} PRBS sequences, while the other channels were generated with random PM-16QAM symbols. At the receiver, each CUT has been independently filtered with a fully-data-aided 17-tap LMS adaptive equalizer, then the generalized SNR is evaluated directly on the received constellation. No phase recovery is applied since lasers are assumed ideal.

Simulation results, compared with predictions of the GGN-model, are shown in Fig. 2.17. The GGN-model once again is in a good agreement with simulation results, correctly estimating the slope of the SNR across all channels. It should be noted that the model shows a *conservative* 0.2 dB gap from simulation results. This is due to the well-known conservative assumption made by the GN-models family. This is not shown in the experimental validation campaign, as in this case, it is not possible to isolate SRS-induced effects as it can be done via SSFM based simulations, as experimental uncertainties erode such margin.

2.8 Nonlinear models for Physical Layer Aware Networking

The selection of a nonlinear modeling framework for physical layer aware networking needs to be addressed based on the type of the considered applications. Focusing on physical layer aware optical networking we can highlight two main application domains: *network design*, and *network orchestration*. During network design, operators and vendors need to assess the capability of their infrastructure to carry information, therefore they are asked to assess the capability of different physical layer hardware solutions performing trade-off analyses between cost and performance both in green-field and brown-field scenarios. For network orchestration, physical layer modeling can be used for quick performance estimation for optical feasibility calculations both for circuit deployment and restoration.

During the network design phase, several key assumptions are often made in order to evaluate network performance. These are mainly related

to traffic patterns agnosticism, and worst-case or End-of-Life (EOL) design. As long-term reliable traffic predictions are extremely difficult to obtain [126], [127], network architects do not usually rely too much on them for physical layer aware network design, and traffic agnostic network analyses are usually performed, even though they could imply a certain degree of hardware over provisioning [127]. At the same time, as deploying optical infrastructure on a vast geographical scale requires a very high level of capital expenditure (CAPEX) , designs need to be resilient and able to absorb unpredictable traffic variations that are often not intercepted by traffic forecasting. For the same reason, physical layer performance in networking context is often evaluated considering full bandwidth occupation, in order to avoid performance degradation due to increased nonlinear interference among channels, or variation of working points or replacement of hardware components such as amplifiers. Even though recent theoretical studies [128] have shown that computing optical performance based on the *exact* spectral occupation may yield some cost savings, however, realistic hardware limitations are imposing to develop worst-case reliable designs. As detailed explained in Sec. 2.9, in this thesis, realistic worst-case bandwidth allocation will be always considered. Moreover, high CAPEX forces operators to exploit the optical infrastructure for many years (often more than 10) to yield a decent return on the investment (ROI). Such a requirement imposes strong constraints on network architects that needs to design optical networks whose performance, both in terms of capacity and reliability, do not vary over time. To satisfy this constraint, performance metrics of different network design are evaluated both for beginning-of-life (BOL) condition, and end-of-life ones i.e. degraded components parameters due to aging.

2.9 The LOGO Strategy for Optimal Power Settings in Network scenarios

In this thesis we will mainly use the Gaussian noise model to compute degradation caused by nonlinear propagation impairments, assuming incoherent accumulation of NLI. This key assumption allows to greatly simplify the way propagation impairments can be computed in the context of optical

networking. Namely, each fiber span is introducing noise (NLI and ASE) whose characteristics are independent with respect to the previous spans crossed by the signal comb. This assumption is fundamental, also considering that in a transparent networking context, channels might share the same ROADM-to-ROADM link only once, as they can be re-routed to other fibers, and different channels could be added/dropped at each ROADM. In such a scenario, assuming coherent noise accumulation would entail a strong coupling between QoT estimations and routing, and wavelength/spectrum assignment, as a complete knowledge of the routes of each channel would be needed to compute the generalized SNR. For similar reasons, more complex, yet accurate, models that include second order effects such as modulation format dependency cannot be used for QoT estimation in transparent and reconfigurable optical networks as full spectral details (channel frequency, channel routes, modulation formats, etc.) of propagating channels would be needed to obtain SNR estimations. As the SNR itself is needed to assign modulation formats and select routes, adopting more complex nonlinear models would entail a recursiveness in the problem's definition that would be difficult to solve without generating network design extremely specific and tied to a specific traffic profile. For these reasons, in this thesis the incoherent GN-model is adopted, as it represents a conservative, yet accurate, modeling tool for transparent and reconfigurable optical networks. Furthermore, we use the GN-model assuming *full-spectral load*, in order to obtain worst-case NLI values. As widely discussed in [86], [106], [109], [129], the full-load assumption entails a performance underestimation for sparsely populated link or networks, however such underestimation can be at maximum equal to 33% in reach. This limited penalty is compensated by the lower operational complexity of the control plane, and a complete independence of physical layer working point (e.g. amplifiers' configuration) from traffic profiles and network loading.

As an incoherent noise accumulation assumption is made, it is possible to characterize every span of an optical network by a noise-related quantity that expresses the amount of QoT degradation introduced by the span itself. Referring to Eq. 2.23, and considering ASE and NLI as main sources of impairments, we can adopt as such metric the inverse generalized SNR, that

we define as

$$\mathrm{ISNR} = \mathrm{SNR}_{\mathrm{LIN}}^{-1} + \mathrm{SNR}_{\mathrm{NLI}}^{-1} = \frac{1}{\mathrm{SNR}} \tag{2.30}$$

where $\mathrm{SNR}_{\mathrm{LIN}}$ and $\mathrm{SNR}_{\mathrm{NLI}}$ are the linear and nonlinear SNRs respectively. ISNR can be simply defined as an SNR degradation term that expresses how much the SNR is degraded due to ASE and NLI generated in the considered fiber span. In this way, the generalized SNR of a channel traveling across a multi-span route going from a node A to node B on a transparent network is simply given by the inverse of the summation of all SNR degradation terms of all the spans making up the path, i.e.

$$\mathrm{SNR}_{\mathrm{AB}} = \left(\sum_{i=1}^{N_s} \mathrm{ISNR}_i \right)^{-1} \tag{2.31}$$

where N_s is the number of spans making up the path from node A to node B, each of which is characterized by an SNR degradation term ISNR_i. Notice that Eq. 2.31 can be generalized to include additional sources of degradation (e.g. filtering penalties) provided that their net impact on QoT can be modeled by means of an *additive* SNR degradation. As an example, filtering penalties could be roughly modeled this way [130]. Eq. 2.31 can also be rewritten by aggregating span contribution at the link level, i.e. at each ROADM-to-ROADM fiber connection, that can be made of several amplified spans. Starting from this consideration, an optical network can be naturally represented as a graph, i.e. a set of vertices or nodes pairwise related by an edge. Vertices represent ROADMs, and edges represent fiber links in between them. From a QoT perspective, each edge can be weighted by an SNR degradation coefficient and used accordingly to easily derive the QoT of a path traversing multiple nodes. This is a powerful yet elegant abstraction as it allows to use existing graph theory and algorithms for QoT evaluation in an optical networking context. To the best of our knowledge, this abstraction was firstly proposed in [131]. In the next chapter, SNR degradation will be used as a routing metric to rank paths in terms of QoT when when performing RWA. This abstracted network graph representation is pictorially described in Fig. 2.18, where each node-to-node edge is weighted by a SNR degradation term ISNR. Supposing to compute the QoT of a transmission

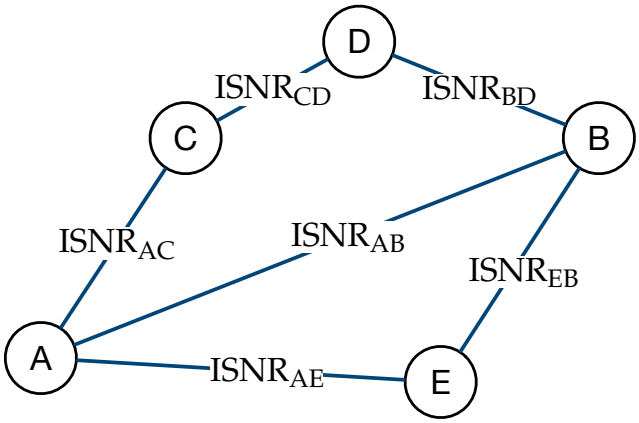

Fig. 2.18 Network representation for QoT calculations

from node A to B, along the path A-C-D-B, one can simply compute it as:

$$\mathrm{SNR}_{\mathrm{AB}} = [\mathrm{ISNR}_{\mathrm{AC}} + \mathrm{ISNR}_{\mathrm{CD}} + \mathrm{ISNR}_{\mathrm{BD}}]^{-1} \tag{2.32}$$

The same network representation can be used to re-interpret the well-known LOGO power optimization strategy [106], [109]. This strategy states that global optimization of SNR over a generic network can be reached by locally maximize the SNR – i.e. minimize its degradation – at the span [106], [109] or ROADM-to-ROADM [110] level. This implies minimizing the weight of each edge in the equivalent graph representation. As QoTs of all possible network routes are made by linear combinations of such weights, to minimize the total SNR degradation and therefore maximize the SNR itself, one needs to minimize each weight. To do so, the launch power at the beginning of each span is set to its optimal value, given by Eq. 2.25, assuming full spectral load, and using as common reference for all channels, the NLI generated on the central channel of the WDM comb, i.e. the channel that suffer the majority of NLI [86] when SRS is not taken into account. In this way, a *single* optimal power value for all the WDM comb is obtained. Recently more complex power optimization strategies have been proposed considering a per-channel power optimization and taking into account exact traffic matrices [123], [128], [132]–[135]. However, these solutions, although enabling moderate capacity gains with respect to a LOGO-like worst-case approach, are in general very *rigid* as they are obtained starting from a fully defined traffic pattern. Furthermore, a per-channel power optimization entails a much

larger management complexity in RWA policies with respect to the LOGO approach, and much tighter amplifier requirements with respect to gain flatness, ripple, and stability to unequal spectrum loading and add/drop adaptation. This being said, a worst-case, frequency independent, optimal SNR degradation metric assigned to each graph edge allows a good trade-off between complexity and capacity optimization, and for this reason it will be always used in this thesis. It should be noticed that the LOGO approach can be generalized to wideband scenarios including SRS-induced power crosstalk exploiting the GGN-model. Such effort is still an open research problem that is not addressed in this thesis, but we envision to use the GGN-model to define optimal power profile yielding optimal flat QoT-levels across the full spectrum.

In the next chapter, a framework of analyses to assess the impact of different physical layer technologies on network performance that leverages on the detailed physical layer modeling tools discussed in this section will be introduced.

Chapter 3

Assessing the Impact of Physical Layer Technologies on Network Performance

In this chapter, a framework of analyses called the Statistical Network Assessment Process (SNAP) will be presented. SNAP is a software tool developed to assess the impact of physical layer technologies on network performance, enabling, therefore, their comparisons in a networking context. Performance enhancement merit and ultimate limit [26] of physical layer technologies can be easily determined in the context of point to point communications, however, it is unclear how to achieve the same in a networking context. To try to fill this gap, we propose the SNAP framework, that can be used to compare potentialities and critical aspects of different technologies, enabling network-level informed decisions about them both in the design and upgrade phase of optical networks.

3.1 A novel perspective on analyses frameworks for optical networks

Research activities related to the design of optical networks have mainly focused on the design of optimal design solutions and to the definition

of RWSA heuristic method to optimize precise networking design aspects. These works include capacity, cost, energy, or multi-objective optimizations [132], [133], [136]–[138]. Such optimization procedures are often extremely specific as they target *precise* objective, exactly fixing the boundary conditions of the analysis, including traffic matrices, and RWA strategies. Such *specificities* allow to obtain tightly optimized solutions, but – on the other hand – they prevent a general assessment and comparison of different physical layer technologies, as these optimization strategies that are mainly related to how traffic is allocated are often adapted to the transmission layer technologies themselves. On the other hand, more general frameworks of analysis are required by operators and vendors to first assess the potentialities and critical aspects of physical layer technologies and network architectures to drive technology selection, design iterations, and finally *specific* optimization. This is clearly tackled in the context of point-to-point optical links, but not in a networking one. Such an aspect is often overlooked in literature, but we believe it to be fundamental for an *effective complexity abstraction* of the network design process. For these reasons, in this chapter, we aim at describing a novel method to achieve this, called the Statistical Network Assessment Process.

SNAP performs optical network architecture load tests: these sort of "stress tests" allow to explore the potentialities of the physical layer independently of specific traffic allocation patterns. To do so, SNAP analyzes a progressive loading of networks according to a defined model for traffic requests and an established routing, wavelength or spectrum assignment (RWSA). SNAP performs a Monte Carlo analysis (MCA) by generating several realizations of progressive random traffic requests coming from the logical to the optical transmission layer. Requests are allocated up to network saturation according to the given RSWA algorithm, and network status is progressively stored for each generated realization of traffic requests, enabling the derivation of the statistics of several network metrics. Contrary to typical analyses aimed at deriving optimal solutions, given the traffic matrix to be allocated and the knowledge of a strategy to do so, SNAP does not assume such a knowledge *a priori*, so enabling to probe strengths and weaknesses of physical layer solutions independently of specific traffic allocation strategies. SNAP outcomes are both static for a given traffic and dynamic

versus loading, so allowing a quantitative comparison of the effectiveness of physical layer solutions both in improving fundamental *capacity* limits and in enhancing performances up to a maximum acceptable blocking. SNAP also drives out weaknesses of networks, as, for instance, links' congestion, consequently addressing specific physical layer and/or RSWA updates. In the next section, the SNAP flowchart will be presented in details, then different examples of applications will be shown.

3.2 Introducing the Statistical Network Assessment Process

In this section, we introduce the Statistical Network Assessment Process (SNAP). SNAP framework has been introduced in [131], [139], [140], to statistically characterize the strengths and weaknesses of different physical layer technologies in reconfigurable optical networks. The flowchart of Fig. 3.1 describes the SNAP algorithm. SNAP is a Monte Carlo based algorithm that can be described as a nesting of two main loops: an inner network loading loop in which the network is progressively loaded, and an outer loop for different Monte Carlo iterations. SNAP requires the following input information:

1. **Traffic model description**.
   Depending on the selected traffic model, SNAP can be used to perform given-traffic or progressive-traffic analyses as described in the following.

   - **Given-traffic analysis**
     A traffic matrix D is defined, in which each element $D_{l,m}$ may represent either a connections' request or a bidirectional data-rate request between nodes l and m. In the former case, the element $D_{l,m}$ serves as the number of circuits or lightpaths (LPs) to be allocated between nodes l and m. In the latter, it is a request for transport between node l and m of *groomed* traffic of size R_G expressed in Gbps that the physical layer is expected to satisfy according to the assumed transceiver technology and spectral grid

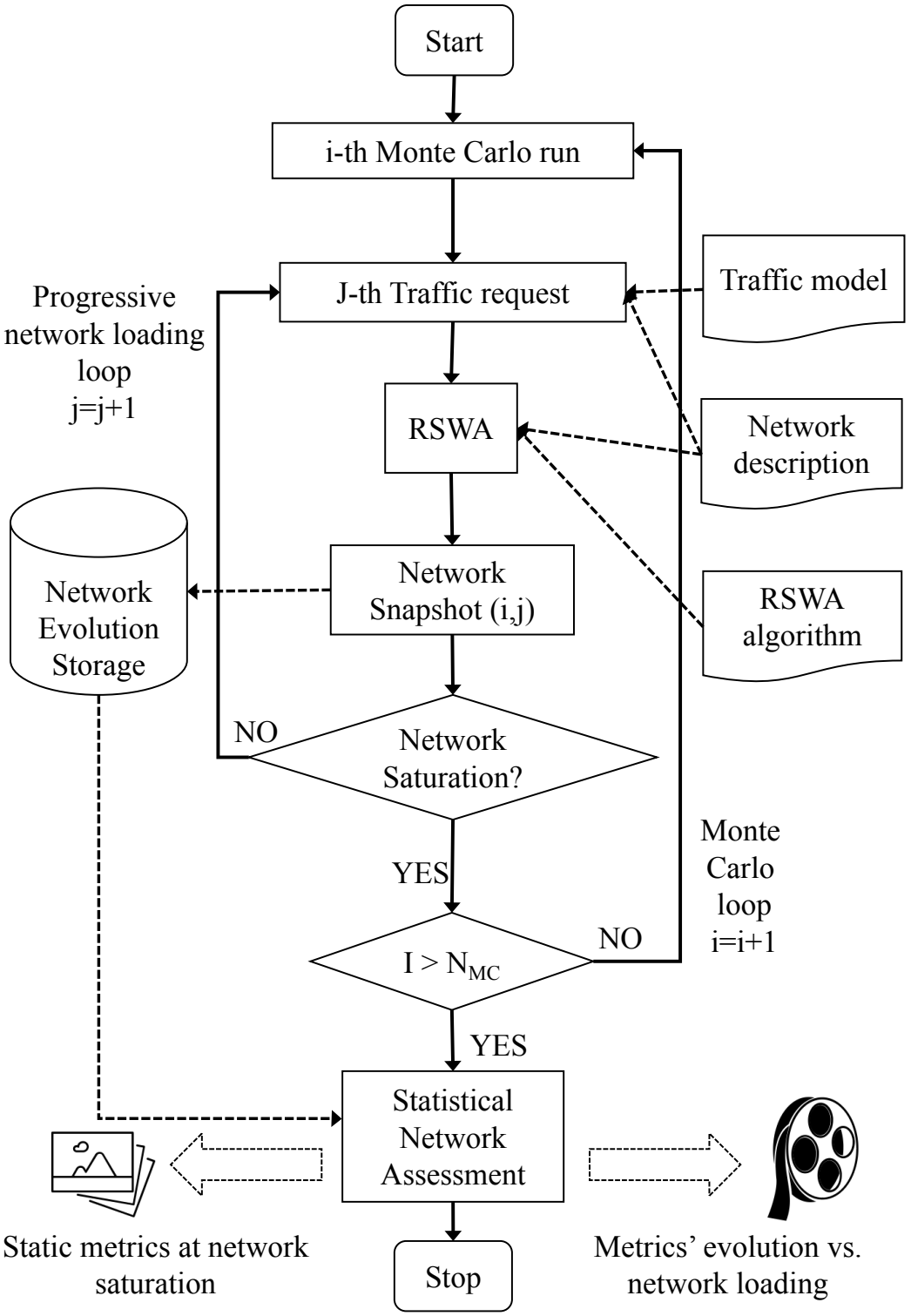

Fig. 3.1 Flow chart for the Statistical Network Assessment Process.

use. For the given-traffic analysis the randomness – Monte Carlo loop in Fig. 3.1 – is in the order the elements $D_{l,m}$ are considered for allocation. The network loading loop ends when all $D_{l,m}$'s are considered by the RSWA algorithm. This analysis is more suitable for derivation of static metrics from network status at the end of every loading loop.

- **Progressive-traffic analysis**
  In this case, the traffic model generates requests evolving indefinitely with the progressive loading loop on j of Fig. 3.1. So, the model is indeed a traffic distribution, namely a bivariate probability mass function in the source/destination node space, expressing the probability that a request for connection between two nodes might occur at j. As for the given-traffic analysis, the type of request can be either a LP-connectivity without rate-size or a data-rate request. For the latter, the request size can be either fixed and defined by the traffic grooming at the logical level or randomly generated according to a specific probability density function. For this analysis, the loop on network loading terminates at network saturation, i.e., when several subsequent requests for connection are blocked. This kind of traffic model is suitable for the estimation of both static and dynamic metrics, as at the end of the Monte Carlo loop we can either derive statistics for each loading level or at saturation.

2. **A full description of network topology and physical layer.**
   For topology definition, we consider number of nodes, connectivity and preexisting network loading due to possible legacy traffic. While, as physical layer characteristics we take into account fiber type, amplification method, power optimization strategies, available optical bandwidth (C-band or L-band, etc.), fix- or flex-grid spectral use, grid size, and transceiver characteristics and placement. Physical layer parameters are needed to compute the figure of merit for the QoT, i.e., the generalized SNR via the GN-model as described in Chapter 2.

3. **Characteristics of the Routing and Spectrum/Wavelength Assignment (RSWA)** algorithm, i.e., the routing policy. Namely, the way in which

fiber paths between nodes' pairs are computed and ranked and spectral slots assigned to connection requests. For example, a shortest path or smallest number of hops routing could be adopted.

During each Monte Carlo iteration, the network is loaded according to the traffic model of choice as in the following. In case of given-traffic analyses, the order of requests for traffic allocation is shuffled and each of them is tentatively allocated according to the selected RSWA, exploiting the analyzed transceiver technology and spectral use defined by the network description. For each Monte Carlo loop, the allocation ends when the full list of demands has been considered. For *progressive-traffic* analyses, traffic between random source-destination pairs is generated according to the input traffic model and tentatively allocated according to the input RWSA policy. In such case, the allocation process ends either when the network is fully saturated, or a maximum number of consecutively missed allocations is reached. For both types of analyses several networks metrics can be computed and stored at each j-th tentative allocation during each i-th Monte Carlo run. Among others, the set of metrics may include the ones listed and described in the following.

- The average bitrate per lightpath $R^i_{b,\lambda}$ that is given by

$$R^i_{b,\lambda} = \frac{1}{N_{L,i,j}} \sum_{n=1}^{N_{L,i,j}} R_{b,n} \quad \text{[Gbps]} \tag{3.1}$$

  where $N_{L,i,j}$ is the number of allocated lightpaths during the i-th Monte Carlo run up to the j-th demand and $R_{b,n}$ is the bit-rate of the n-th allocated LP.

- The spectral saturation of each fiber link, i.e., details about spectral occupation of each node-to-node fiber connection.

- Blocking information such as the number of blocked demands for each node or link, and the causes of such missed allocations.

- Acceptance information such as the number of demands accepted in each node.

The set of metrics to be considered can be modified in order to target specific alternative network aspects. In this sense, SNAP can be easily extended providing a relevant flexibility in the characterization process. Due to the traffic randomization, the allocation process of each Monte Carlo run may differ from previous runs, thus the output results of each run will be – in general – *stochastic*.

After the maximum number of Monte Carlo iterations N_{MC} has been reached, each metric can be statistically characterized with respect to the random traffic generation or scrambling. This means that the probability density functions (PDF) of each analyzed metric can be derived, thus obtaining a *statistical* insight on network capabilities and critical aspects. Statistics of network metrics can be used to derive *probabilistic* information on network performances, such as the probability that the spectrum of a given link will be saturated over a certain percentage, *independently* on how traffic will be allocated on the network. Although Monte Carlo based algorithms [141]–[143] and network load tests [142], [144], [145] have already been used in network analyses, to the best of our knowledge, the approach proposed here is original and innovative, as it represents a whole unique framework of analyses for optical network for the assessment of the merit of physical layer technologies on network performance. In addition to this, exploiting SNAP one can focus on the statistics of results either at the end of the allocation processes, thus obtaining *static* metrics representing the network status, or versus the loading evolution in order to obtain a *dynamic* representations of network conditions. Both analyses can be performed independently from the traffic type, but in general, the *dynamic* one is more relevant in case of progressive-traffic due to the larger number of demands that are generated in that case. Similarly, the given-traffic case is more likely to be analyzed considering static metrics. Both kinds of metrics representations will be considered, applying the static ones to given-traffic analyses and the dynamic ones to progressive-traffic scenarios. In the next sections, several examples of applications of the SNAP framework will be given, showing how SNAP can be used to compare different physical layer technologies and derive qualitative and quantitative results highlighting potentialities and critical aspects of different network designs and topologies.

3.3 Given Traffic Analyses on Sparkle Pan-European Topology.

In this section, a SNAP given-traffic analysis is considered to test the merit of different physical layer technologies on network capacity. We analyze a Pan-European Telecom Italia Sparkle topology whose data have been taken from the EU-funded project Idealist [146]. The full description of the topology is reported in App. A. We apply SNAP using a *given traffic* analysis, and we assess the average bitrate per LP – $R_{b,\lambda}$ – as a static metric, i.e. at the end of the allocation process. As traffic model we consider an any-to-any connectivity matrix D, i.e. $D_{l,m} = 1 \; \forall \; l, m$ and $D_{l,m} = 0$ for $l = m$. As RWA policy we consider a QoT-based k_{MAX}-shortest-path routing policy with first fit wavelength assignment, exploiting for SNR calculations the network abstraction under a full-load assumption over the C-band (80 channels at 32 GBaud over the standard 50 GHz grid) described in Sec. 2.9. EDFA transparent amplification with 5 dB noise figure is assumed. ROADM nodes are assumed to introduce a 10 dB loss that is recovered by an additional booster EDFA, while filtering penalties and add/drop limitations are neglected. As a baseline scenario, SSMF fiber spans are assumed. Using the proposed QoT-based routing policy, paths are ranked based on their generalized SNR, and the best k_{MAX} (highest SNR) are selected. Such policy is simply aimed at greedily optimizing capacity during lightpath allocation, by choosing paths having the largest possible QoT, and therefore Shannon capacity [26]. Such routing policy has been implemented by using the well-known Yen's algorithm [147], using it over the network graph described in Sec. 2.9, i.e. a graph whose edges are weighted by an additive SNR degradation term that includes both linear and nonlinear effects. When a connection demand is successfully allocated, a modulation format, and thus a bitrate, is assigned to it based on a given sensitivity curve (spectral efficiency vs SNR) describing a target transceiver. After the completion of the allocation process of a single Monte Carlo run, i.e. when all elements of matrix D have been tentatively allocated, the average bitrate per LP is calculated by means of Eq. 3.1, and stored to be statistically characterized independently from the way LPs are allocated on the network.

We consider two different implementations of flexible-rate transceivers as reference for bitrate assignment: time division hybrid modulation format (TDHMF) based transceivers, and flexible pure format transceivers. Both transceivers families implement elastic bitrate adaptation, allowing for trade-off spectral efficiency (SE) vs required SNR at constant bandwidth occupation. In pure format based elastic transceivers, bit rate adaptation is achieved by switching PM-M-QAM formats, delivering *quantized* SE values. On the other hand, TDHMFs permit to tune with continuity SE vs SNR, by time switching different PM-M-QAM modulation formats. A more detailed description of TDHMF is out of the scope of this thesis, but can be found in [41], [143], [148]. The sensitivity curves of SE vs SNR for these two transmission technologies at a pre-Forward Error Correction (pre-FEC) bit-error rate (BER) target of $4 \cdot 10^{-3}$ are reported in Fig. 3.2. This pre-FEC BER level is not referred to any specific standard or commercial product, as it has been selected to derive reasonable quantitative results. Considering *specific* FEC implementations, larger values of pre-FEC BER could be considered. A 32 GBaud gross symbol rate corresponding to a net symbol rate $R_s = 25$ GBaud per channel due to protocol and coding overhead is assumed. It should be noted that only PM-M-QAM squared formats (QPSK, 16-QAM, 64-QAM) are considered in Fig. 3.2, i.e. the ones that are able to be used with threshold-based receivers. Although flexible transceivers including non-squared formats such as 8-QAM and 32-QAM can be implemented increasing the DSP complexity, they have not been considered in this study. Moreover, non-squared constellations are not uniquely defined – e.g. star-8- QAM vs. rectangle-8-QAM [149] – thus introducing additional degrees of freedom to the considered analysis.

We focus our analyses on two main aspects: (i) the importance of NLI estimation for performance estimation and correct tuning of the network control plane (Sec. 3.3.1) , (ii) the assessment of different network upgrades performed at a node level, specifically optical amplifiers (Sec. 3.3.2), and ROADMs (Sec. 3.3.3). Throughout these sections, we will consider the two aforementioned implementations of bitrate flexible transceivers. Over the recent years several authors have performed similar analyses [143], [150]–[154], however a comprehensive study based on a *single* framework such as SNAP is still missing. As described in the introduction of this chapter, many optimization procedures have been proposed to optimize the deployment

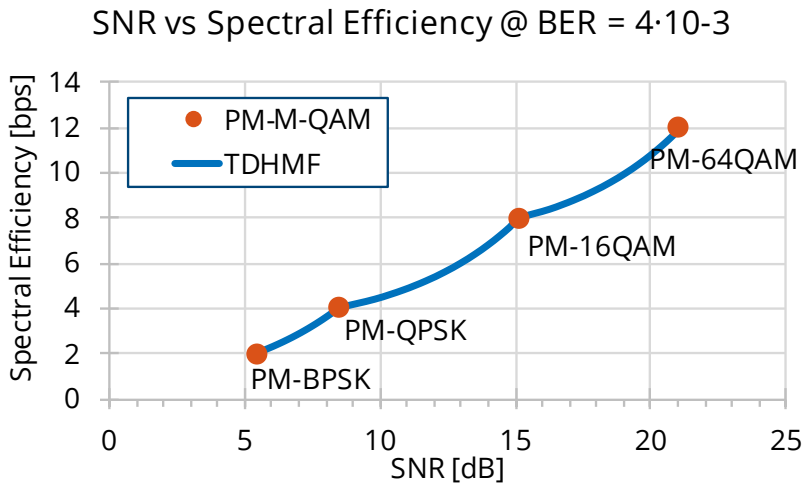

Fig. 3.2 Sensitivity curve for bitrate elastic transceivers.

of a given technology, but no *general* assessment are given. This aspect represents the main purpose and novelty of SNAP.

3.3.1 Merit of NLI on network performance and flexible rate transceivers.

In this example of application of SNAP we assess the impact of NLI penalty on network capacity, and the capacity penalties deriving from drift from LOGO power settings.

As a first step of the analysis, we verified the convergence of the Monte Carlo analysis, i.e., the number of Monte Carlo iterations N_{MC} needed to obtain statistically stable results. To this purpose, we consider the PDF of the average bit-rate per LP given by Eq. (3.1) obtained with $N_{MC} = 10^3$ and $N_{MC} = 5 \cdot 10^4$. Results reported in Fig. 3.3a are obtained considering TDHMF and selecting as feasible paths between two nodes only the path having largest SNR, i.e., $k_{MAX} = 1$. In Fig. 3.3a, a Gaussian fit for the two PDFs is also reported, showing good agreement with the simulative results. We can notice that $R_{b,\lambda}$ is Gaussian-distributed with respect to the lightpaths' allocation process. The PDF of $R_{b,\lambda}$ converges towards a truncated Gaussian due to the central limit theorem. $R_{b,\lambda}$ is in fact computed by summing a large set of random bit-rates, that – for TDHMF – are distributed almost

uniformly in the interval [50 Gbps, 300 Gbps]. We will consider $R_{b,\lambda}$ average value as *figure of merit* (FOM) to compare the two different implementations of flexible bitrate transceivers. From Fig. 3.3a it is intuitive to understand that independently of the order in which LP demands are allocated, the considered network topology is able to deliver on average 211 Gbps per LP. This means, 4.4 bpS per polarization, that is a value larger than the one delivered by a PM-16-QAM modulation format. We also remark that the variance of $R_{b,\lambda}$ is strictly related to the network blocking. In particular, since the complete set of LP demands cannot be allocated, the set of blocked LP demand will differ in each Monte Carlo run, so the quantity $R_{b,\lambda}$ will be stochastic. Under the same test conditions, in particular, $k_{MAX} = 1$, if the physical layer was able to allocate all requests, the variance of $R_{b,\lambda}$ would be zero. This happens because all possible LP requests would be allocated on the best SNR path, thus giving a deterministic $R_{b,\lambda}$. Increasing the set of feasible paths – i.e., increasing k_{MAX} – expands the variability of the overall allocation process, thus increasing the variance of $R_{b,\lambda}$. Thus, in general, the stochastic behavior of $R_{b,\lambda}$ is caused by two factors: network blocking and routing strategy ($k_{MAX} > 1$). In addition to the PDF of $R_{b,\lambda}$, we report in Fig. 3.3b its mean and standard deviation – indicated as $< R_{b,\lambda} >$ and $\sigma_{R_{b,\lambda}}$, respectively – versus N_{MC}. It can be noted that the mean value of the average bit-rate per LP already converges for $N_{MC} \geqslant 100$, whereas the standard deviation converges for $N_{MC} \geqslant 1000$. Hence, we safely set $N_{MC} = 2500$ to perform the following analyses.

We start evaluating the impact of NLI on the considered network level FOM, i.e. the average $R_{b,\lambda}$. With such a purpose, we set the transmitted power per channel on each network span P_{ch} to

$$P_{ch} = P_{ch}^{opt} + \Delta P \quad [\text{dBm}] \tag{3.2}$$

with $\Delta P \in [-4, +4]$ dB, and P_{ch}^{opt} being the optimal LOGO power given by Eq. 2.25. Each Monte Carlo analysis was performed either considering or neglecting the effect of NLI, i.e. by neglecting the nonlinear contribution in the SNR degradation formula given by Eq. 2.30, thus operating over a network graph whose edges are weighted an SNR degradation term that does not include nonlinear terms. As far as the routing policy is concerned,

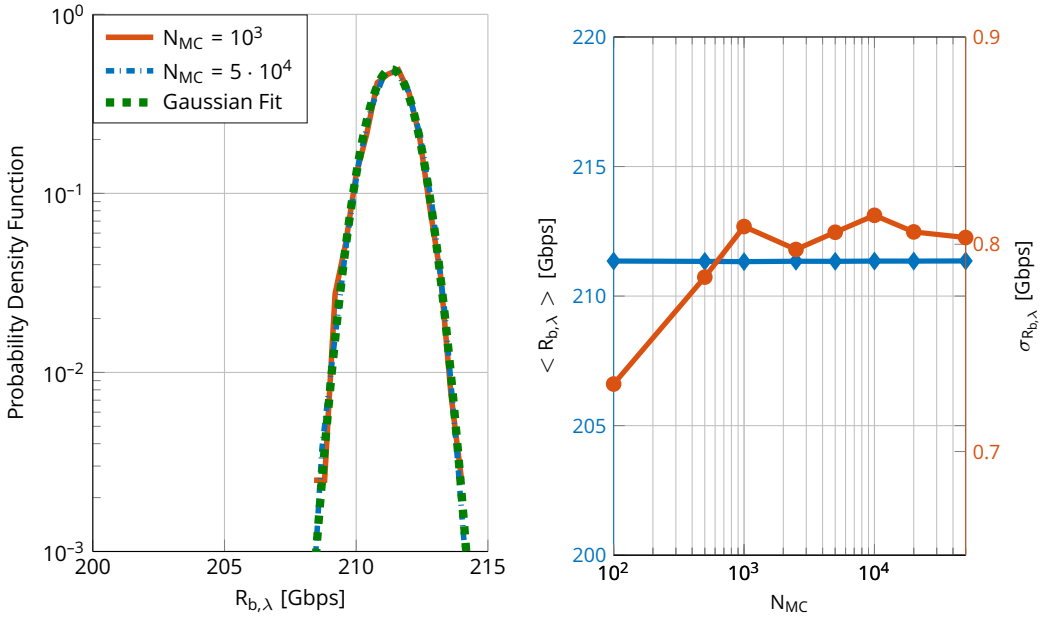

(a) Probability density function.

(b) Mean (left axis – diamond markers) and standard deviation (right axis – circular markers).

Fig. 3.3 Convergence analyses of the average bitrate per LP vs number of Monte Carlo runs assuming TDHMF and $k_{MAX} = 1$.

k_{MAX} was set to 1. Fig. 3.4 reports the mean value of the average bitrate per LP $< R_{b,\lambda} >$ versus ΔP for each of the two transceivers implementations, both considering (solid curves) and neglecting NLI (dashed curves). Focusing on results that include NLI, the pure format transceivers curve displays an $< R_{b,\lambda} >= 172$ Gbps at optimal launch power, while TDHMF based transceivers enables reaching $< R_{b,\lambda} >= 211$ Gbps as already shown in Fig. 3.3a, showing a 23% advantage at the selected pre-FEC BER. Using a more powerful FEC would probably increase the mean average bitrate per LP for both TDHMF and pure formats, but the general result, i.e. that TDHMF outperforms flex PM-M-QAM would still hold. Such noteworthy improvement is enabled by TDHMFs allowing a better exploitation of SNR available on LPs, that is however traded off by an increased complexity of the DSP electronics of the transceivers, thus an increased CAPEX for node equipment. Although being elastic, the pure format approach allows a poor granularity in SNR vs. SE, since, for instance, approximately 6 dB SNR increase is required to move from, say, PM-QPSK to PM-16-QAM. TDHMFs

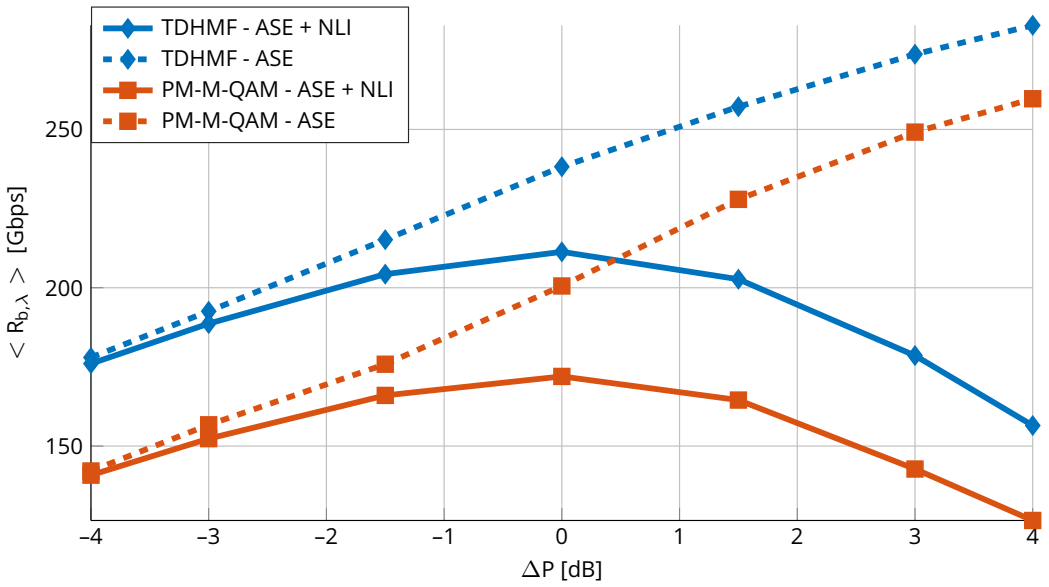

Fig. 3.4 Average $R_{b,\lambda}$ vs ΔP for two flexible bitrate transceivers with and without NLI.

allow to overcome such limitation, thus supporting a relevant performance improvement at a network level. Moving away from the optimal power by ± 1.5 dB, $< R_{b,\lambda} >$ decreases of approximately 5% for both transceivers technologies. This gap increases to approximately 36% at $\Delta P = 3$ dB. The penalty is smaller ($\approx$12%) in the linear regime, i.e. $\Delta P = -3$ dB. Focusing now on the curves for which NLI is neglected, i.e. the dashed plots in Fig. 3.4, it can be observed that neglecting NLI, $< R_{b,\lambda} >$ is overestimated of 13% and 16% at optimal power when considering TDHMF or pure formats transceivers, respectively. In both cases the error grows up if we move away from the optimal power: 27% overestimation for TDHMF and 38% for PM-M-QAM at $P_{ch} = P_{ch}^{opt} + 1$ dB.

The relevance of these results is threefold: Fig. 3.4 shows the penalties on network capacity independently from how traffic is allocated on a network due to (i) optimal power selection errors, (ii) NLI estimation errors, and (iii) their joint effect. Neglecting NLI yields to a large capacity overestimation, that gets exacerbated for power values larger than the optimal one. These results, obtained with a novel approach, therefore highlight the importance of correctly estimating propagation impairments to optimize power levels in optical networks to obtain reliable network designs.

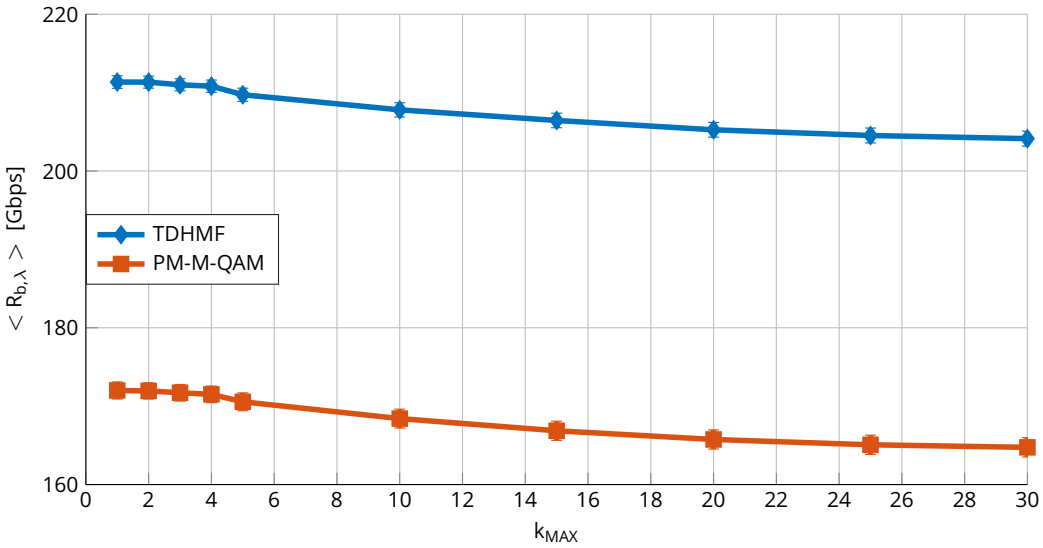

Fig. 3.5 Average $R_{b,\lambda}$ vs k_{MAX} for TDHMF and PM-M-QAM based flexible bitrate transceivers.

In addition to this type of analysis, to further compare the considered transceiver implementations we have estimated how varying the routing policy characteristics affects the considered network FOM. With such an objective, we have varied the parameter k_{MAX}, thus the number of ranked routes between two nodes that can be considered as suitable during the routing and allocation process of the SNAP algorithm, from 1 up to 30. As depicted in Fig. 3.5, a decrease in the average $R_{b,\lambda}$ at optimal launch power and an increase in its variance take place for increasing k_{MAX}. This behavior can be explained by considering that as k_{MAX} increases, several paths with non-maximum QoT will be considered as suitable during the RWA process, thus reducing the average SNR per LP and the corresponding average bit-rate per LP as well. Moreover, increasing k_{MAX} enlarges the set of possible paths between nodes' pairs. This provides more candidate paths for demands' allocation thus reducing the blocking ratio and expands the variability of the RWA's outcome between different Monte Carlo runs. Hence, the variance of $R_{b,\lambda}$ increases with k_{MAX}. Finally, referring to Fig. 3.5, it can be remarked that the performance advantage of TDHMF with respect PM-M-QAM formats is independent of k_{MAX}, remaining constant around to 23%.

3.3.2 Merit of amplifier noise figure on network performance.

In this section, we consider the effects of different amplifier technologies on the considered network level capacity FOM. In particular, we consider the variation in $R_{b,\lambda}$ due to the reduction of the noise figure in optical line amplifiers moving from the 5 dB reference value, down to 0 dB. We perform such upgrade in all spans with loss larger than 15 dB, simulating an upgrade of amplification systems moving from EDFA solutions towards Hybrid Fiber Amplifiers, i.e. amplifiers exploiting Raman amplification in conjunction with EDFAs. We do not consider spans whose loss is smaller than 15 dB as HFA amplifiers do not deliver consistently better noise performance than EDFAs in this condition [74]. We assume to use HFAs with counter propagating pumping scheme in the so-called *moderate pumping regime*, in which Raman amplification is used to recover approximately the 60% of the span loss. Under these assumptions, gain frequency dependence and pump depletion are negligible. Furthermore, the NLI coefficient and equivalent noise figure (ENF) are independent of the power per-channel [74], thus the ENF can be safely changed independently from it. Thanks to this power stability, the moderate pumping regime is indicated for reconfigurable optical network scenarios where channels are continuously added and dropped. Furthermore, as we consider such moderate pumping regime scenario, the incoherent GN model can be safely used to derive the LOGO power settings, without resorting to the more complex GGN model. Fig. 3.6a shows the average bitrate per LP for both transceiver technologies vs ENF. The data for ENF < 4 dB corresponds to HFA systems. Fig. 3.6b depicts the percentage of variation in average $R_{b,\lambda}$ vs the reduction of ENF. It can be noted that the relation between these two quantities is linear: for each dB reduction of ENF, there is a 3% increase in average $R_{b,\lambda}$ for TDHMF and a 4% increase for PM-M-QAM based transceivers. Halving the ENF, moving from 5 dB to 2 dB, the capacity improvement in terms of average bitrate per LP is 12% for TDHMFs and 10% for PM-M-QAM. Such gains are compatible with the one recently obtained in [155]. The performance gap between the two transceiver implementations decreases with decreasing ENF, from 23% at ENF = 5 dB to 17% at ENF=0 dB. The reason for such behavior is due to the fact that with low ENF, there is a smaller number of LPs with poor QoT that can experience

a greater benefit from the continuity in bitrate vs SNR tuning granted by TDHMF, so the gap between the two formats wears thinner.

These results highlight that *uniform* upgrades of amplification technologies can yield relevant capacity improvement – 15% at least with relatively rigid transceivers such as PM-M-QAM based ones – but at a high CAPEX. Later in Sec. 3.5, we will discuss how to use SNAP to *selectively* identifying locations over which deploy upgraded OLEs, in order to trade-off capacity increase and CAPEX.

3.3.3 Merit of ROADM node insertion loss

In this section, we evaluate the impact of different ROADM insertion loss on network performance. To this purpose we varied the ROADM loss from the reference value of 10 dB in an interval from 7 dB up to 20 dB. The results are shown in Fig. 3.7a, where an improvement of average $R_{b,\lambda}$ is obtained by decreasing the ROADM loss for both TDHMF and PM-M-QAM implementations. Fig. 3.7b represents the percentage of average bitrate per LP variation vs the variation of the ROADM loss. In such case the relation between these quantities is not linear. The pure formats display a larger gain vs the decrease of the ROADM loss from the reference 10 dB value than TDHMFs. Such gain is around 1.5%/dB. When the ROADM loss is instead increased, pure formats undergo a larger average $R_{b,\lambda}$ worsening than TDHMF (around $-3\%/\text{dB}$ vs $-1\%/\text{dB}$) due to their poor SE vs granularity. This result shows how the network capacity improvement enabled by ROADM insertion loss upgrade is not so relevant, thus operators and vendors should not focus their effort on this technological aspect.

3.4 Progressive traffic analyses: a topology stress test

In this section, progressive traffic analyses are introduced. They differ with respect to given traffic analyses as they consider a progressive loading of the network topology, thus not imposing any hard limitations on the number

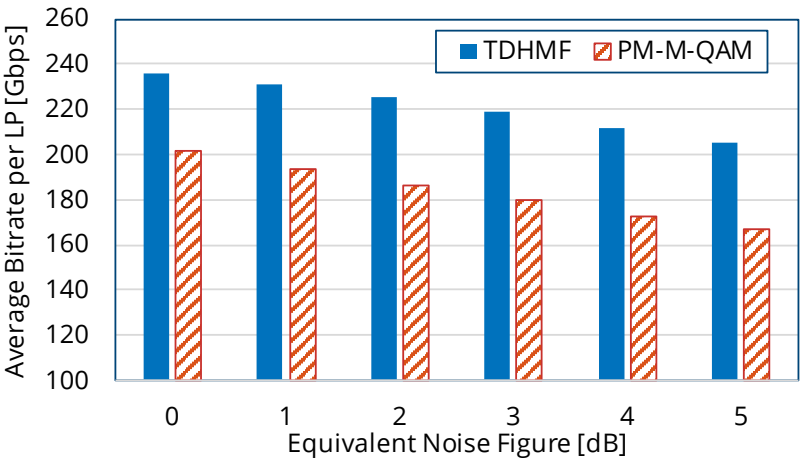

(a) Average $R_{b,\lambda}$ vs ENF.

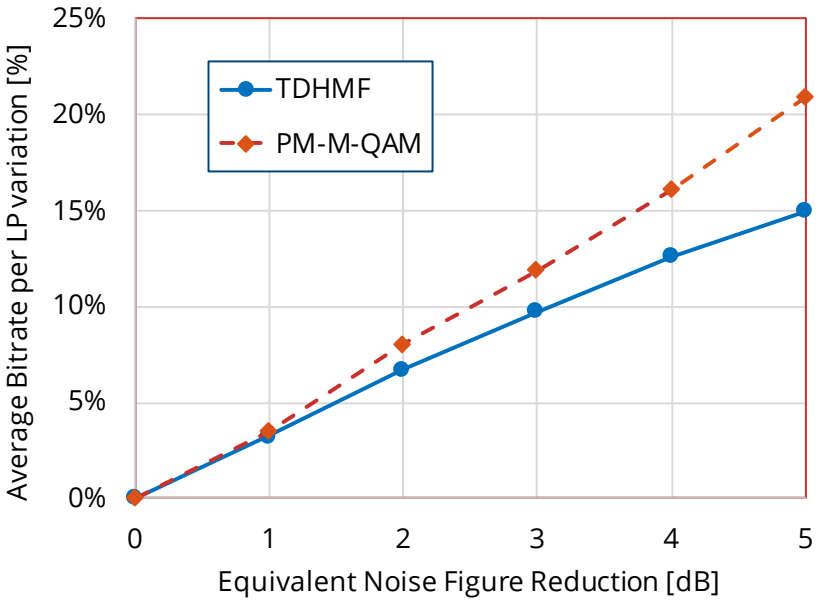

(b) Average $R_{b,\lambda}$ improvement vs ENF reduction.

Fig. 3.6 Impact of amplifier noise figure on network capacity.

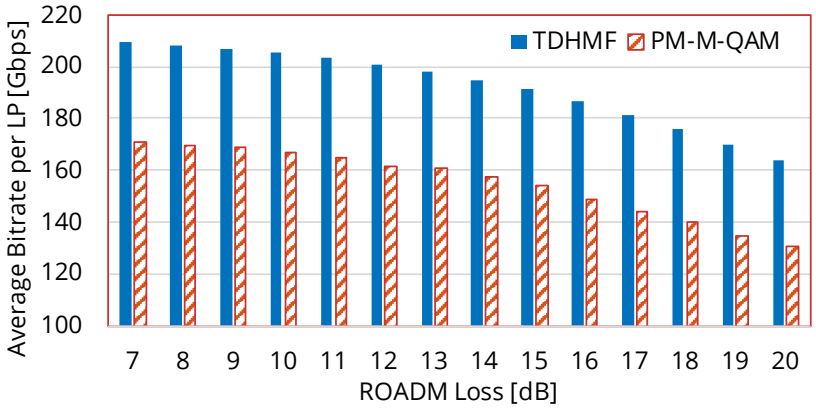

(a) Average $R_{b,\lambda}$ vs ROADM insertion loss.

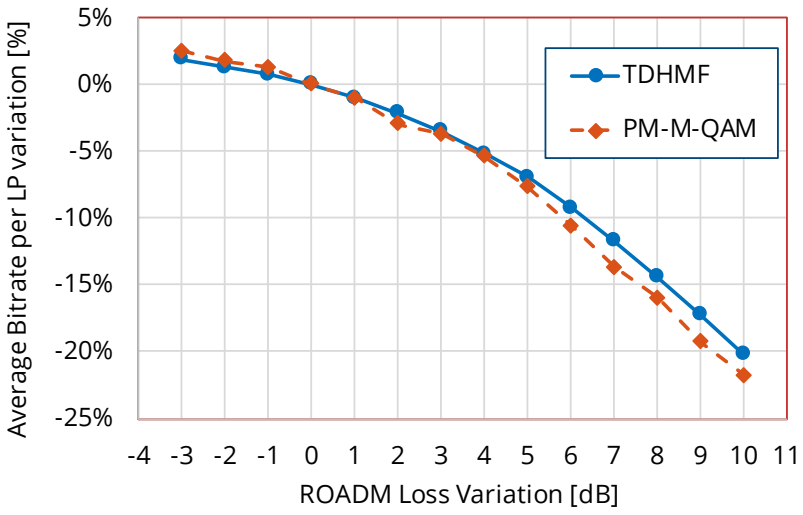

(b) Average $R_{b,\lambda}$ improvement vs ROADM insertion loss reduction.

Fig. 3.7 Impact of ROADM insertion loss on network capacity.

of lightpaths that can be loaded on the network. Network allocations are blocked at network saturation, i.e. when no more connections can be allocated in the network. Such kind of analysis represents a sort of stress test for network infrastructure, aimed at identifying ultimate topological bottlenecks, design critical aspects, and suggest possible upgrade solutions. These insights are useful to network operators and vendors both for green and brown field scenarios, as they yield a general assessment of network infrastructure potentialities. SNAP results being statistical, the outcomes of the analyses are independent of specific traffic realization, therefore absorbing up to a certain degree, the uncertainties that are inherent in assuming to operate with precisely defined traffic matrices. This approach is feasible as SNAP is not aimed at delivering optimized solutions to specific problems, but rather at yielding general technological comparisons. In the next paragraphs, dynamic metrics estimation will be targeted by focusing on quantities such as blocking probability and links' saturation vs the total progressively allocated traffic.

In this section we apply SNAP-based progressive traffic analyses to two different network topologies: a 17 nodes, 26 links network topology and a Pan-European 28-nodes, 41 links network. In both scenarios we assume the amplified node-to-node fiber links to be in pairs, providing bidirectional connectivity between nodes such that networks are considered as undirected graphs. We assume uniform, uncompensated and amplified fiber links with lumped EDFAs fully recovering fiber losses and characterized by a noise figure of 5 dB. We assume fiber spans to be made of SSMF with parameters reported in Tab. A.1. We suppose all nodes to be equipped with ROADMs introducing a routing loss of 18 dB, fully recovered by an additional EDFA at the output of nodes. We do not consider any further impairment on channel spectra caused by filtering effects of ROADMs. We assume that the physical layer operates WDM transmission on the C-band set to Bopt = 4 THz exploiting the 50 GHz ITU-T fix-grid, consequently enabling a maximum of Nch = 80 lightpaths – channels at given wavelengths – per fiber. Additional details about these network topologies are reported in App. A.

As RWA algorithm we assume the same QoT-based k_{MAX}-shortest-path routing policy with first fit wavelength assignment described in Sec. 3.3. For the following, $k_{MAX} = 50$ has been assumed, thus operating on a wide

portion of the routing space, i.e. limiting as much as possible wavelength contention introduced by limited path options.

As traffic model, we assume that requests generated at every j-th iteration of the SNAP network loading loop are random and uniformly distributed among nodes. It means that the probability of getting a request for a data connection between two nodes is constant and equal to $1/[N_n(N_n-1)]$ for each nodes' pair, for each j. N_n is the number of network nodes generating and receiving traffic. We assume that all nodes are generating traffic. We assume requests to be defined by their traffic-grooming size R_G, being either 100 Gbps or 200 Gbps for each connection requested between each nodes pair. To accommodate these traffic request we consider two different transceiver families: fixed-rate rigid transceivers and bitrate and bandwidth flexible transceivers. We assume rigid transceivers to operate using either PM-QPSK or 16-QAM, delivering 100 Gbps or 200 Gbps respectively. On the other hand, bitrate and bandwidth flexible transceivers are equivalent to the pure-format flexible transceivers discussed in Sec. 3.3, with the additional feature of switching the signal symbol rate between 32 and 64 Gbaud, addition of being able to able to change switch both modulation format using either PM-BPSK, PM-QPSK, PM-16QAM or PM-64QAM and symbol rate, allowing for better SNR sensitivity at the cost of spectral efficiency. As an example, with this family of transceivers, a 200 Gbps request can be accommodated either using a single 32 GBaud PM-16QAM signal or a 64 GBaud PM-QPSK signal, if the path QoT does not allow to accommodate for a PM-QPSK signal. No high baudrate implementation penalties have been considered, thus, 32 GBaud and 64 GBaud signals have equal SNR sensitivity. A pre-FEC BER level of $4 \cdot 10^{-3}$ was chosen for reference sensitivity calculations. For both transceiver families, a 25% overhead including both FEC and protocol overhead has been assumed.

For the following analyses, the observation of network performances down to a blocking probability of 0.1% has been targeted. To this regard, we set the number of Monte Carlo iterations $N_{MC} = 10000$, to perform a proper statistical evaluation of dynamic metrics. Moreover, as the number of traffic request is not limited, we established exit conditions for the network loading loop of SNAP. To this purpose, we defined to perform random progressive allocations up to the network status for which more than 5000 requests

have been generated and more than 50of them is blocked. We consider the following dynamic metrics:

- Blocking Probability (BP), that is the probability of demand $j+1$ being blocked after demand j. BP expresses the Grade-of-Service (GoS) of the network under progressive loading, as it is expressed as a function of j
- Total allocated network traffic computed by summing the number of allocated requests up to the j-th demand. Selecting a target GoS, one can evaluate the average maximum traffic that the network can sustain at that target GoS.
- Links' saturation or utilization, i.e., the number of the occupied LPs over the total available bandwidth in each network link.

Fig. 3.8a represents the growth of average BP vs. average total allocated network traffic for two different grooming values and the fixed- or flexible transceivers for the German topology. As it can be expected, BP progressively grows as the network is progressively loaded by allocating random traffic requests. The smaller-size German topology, when operated with a traffic grooming of 200 Gbps achieves better performances than the $R_G = 100$ Gbps case, independently of the transceiver configuration. This is due to physical layer characteristics and to the network size enabling an average QoT of LPs that is well matched to the SNR sensitivity required to fulfill 200 Gbps requests: operating with smaller grooming entails a waste of network achievable throughput close to 50%. Moreover, it can be noted that the flexible transceivers do not enable benefits with respect to the fixed-rate ones since a very small number of requests have to be split into multiple channels due to QoT constraints. This is represented by the overlap of the solid (fixed rate) and dashed curves (multi rate) in Fig. 3.8a. The vast majority of requests can be transparently carried using PM-16QAM, delivering 200 Gbps per LP, thus no symbol rate flexibility is exploited. Always referring to Fig. 3.8a, setting a GoS-BP level equal to 1%, the average maximum achievable network throughput up to that BP value can be evaluated. In case of 100 Gbps grooming this value is around 80.5 Tbps, whereas for $R_G = 200$ Gbps it is 160.3, quantitatively confirming that in this case, a grooming of

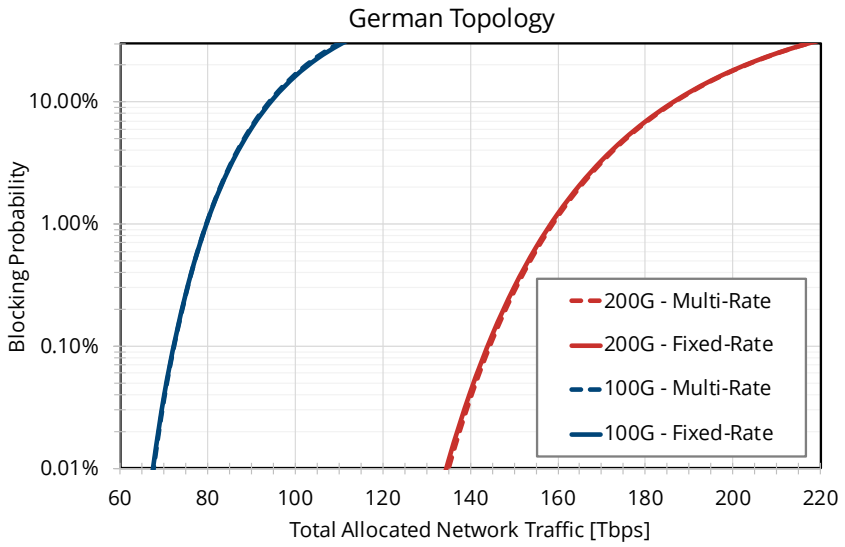

(a) Average blocking probability vs. average total allocated network traffic.

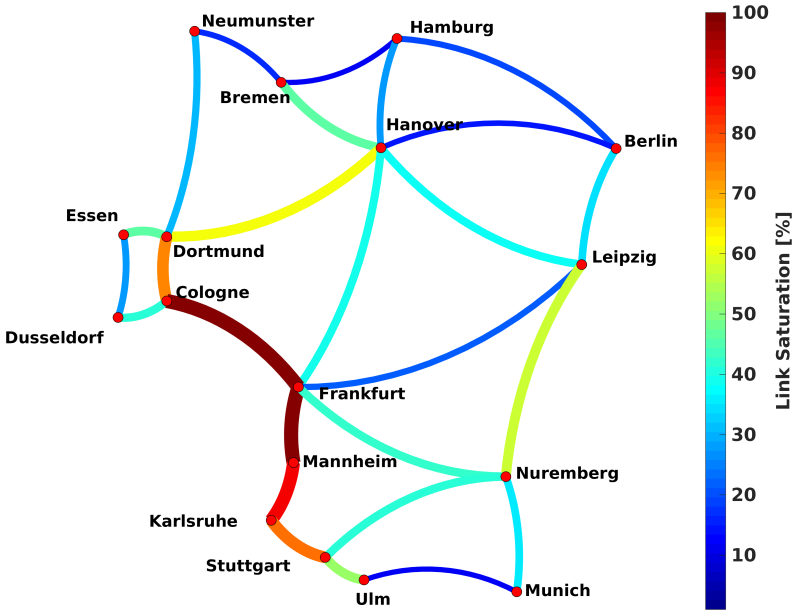

(b) Average links' utilization at BP = 1%. The ticker the lines the more saturated the links.

Fig. 3.8 Progressive-traffic analyses for a German topology.

100 Gbps implies a wasting of almost 50% of the total achievable network throughput.

Fig. 3.8b depicts the average link saturation obtained at GoS-BP of 1% for 200 Gbps grooming and flexible transceivers. Note that this is a static result, but from SNAP outcomes, one could observe the animated representation showing how links progressively saturate on average as the network gets increasingly loaded. An example video of this can be found in Ref.[156]. Referring to Fig. 3.8b one can immediately identify some of the network striking features and critical aspects. Notice for example the high average saturation of the eastern links (from Cologne to Stuttgart) and the low saturation of the northern ones (from Neumunster to Hamburg). These pieces of information can convey advice to network designers and operators: eastern links are more critical in terms of reliability since they carry a large percentage of total network traffic; the northern ones are scarcely used since they are penalized in routing ranks due to their higher SNR degradation, thus they should be improved at the physical layer. Notice that this happens independently of traffic realizations, as these results are averaged over the full set of 10000 Monte Carlo iterations. Such kind of analyses and considerations allow therefore to shed light on the merit of physical layer on networking performances and crucial facets, creating a strong support for physical layer-driven network upgrades and design strategies. An example of this will be described in Sec. 3.5. Fig. 3.9a shows average BP vs. average total allocated network traffic for the Pan-European topology. Notice that the curve for the case of $R_G = 200$ Gbps and fixed-rate transceivers is not shown since a very small portion of LPs has QoT large enough to be operated by PM-16QAM yielding for this case a high average BP larger than 50% already for limited traffic. In general, for this topology, 200 Gbps, and 100 Gbps grooming sizes cannot be ranked in a unique way. For BPs smaller than 1%, 100 Gbps grooming with fixed and flexible transceivers can guarantee better performances than 200 Gbps grooming. As BP increases, this ranking is reversed: for higher blocking, requests groomed at 200 Gbps operated via flexible transceivers permit to achieve a higher throughput, on average. The explanation for such a behavior is that for very low BP, QoT of LPs is dominant with respect to wavelength availability contention: in the low BP regime, LPs are blocked only when they cannot be allocated due to QoT con-

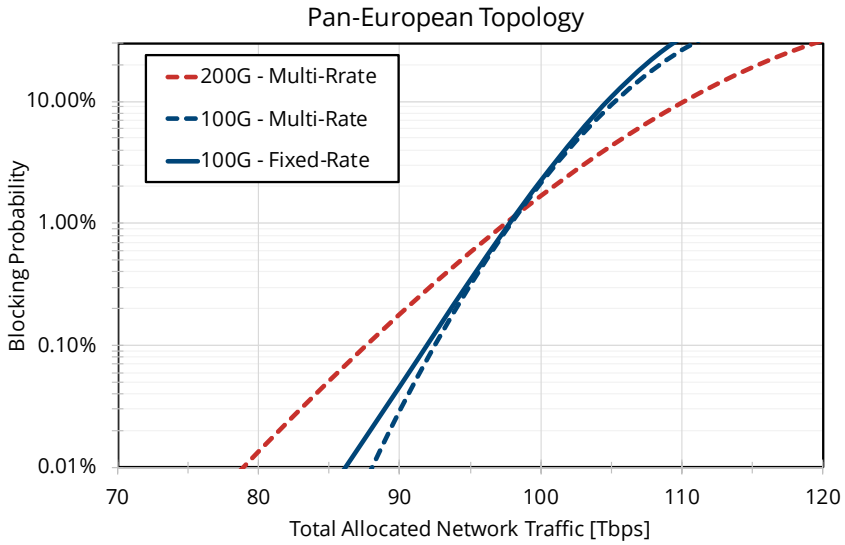

(a) Average blocking probability vs. average total allocated network traffic.

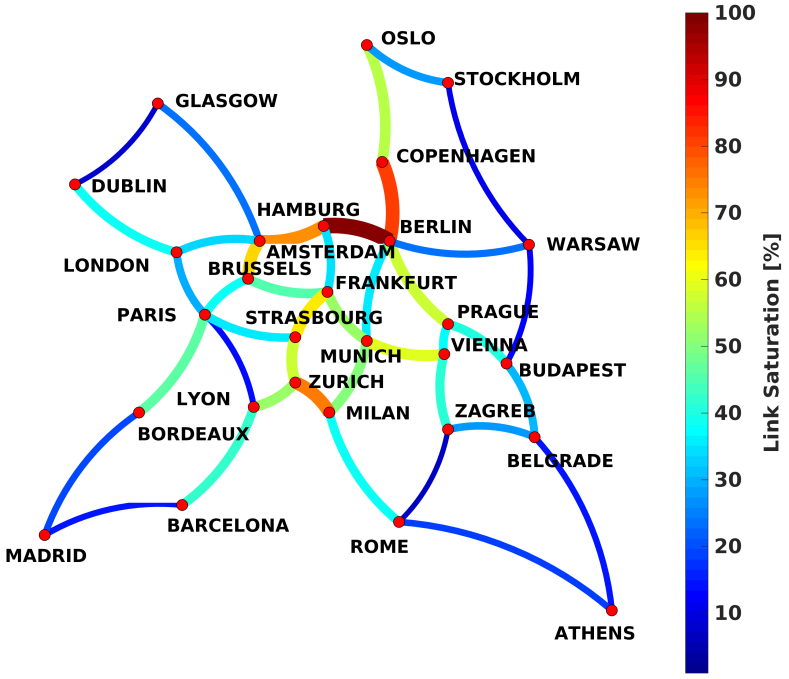

(b) Average links' utilization at BP = 1%. The ticker the lines the more saturated the links.

Fig. 3.9 Progressive-traffic results for a PAN-European topology.

Table 3.1 Average Network Throughput at BP=1% for different transceiver families and grooming sizes.

Transceiver Type	German Topology		Pan-EU Topology	
	100G	200G	100G	200G
Fixed Rate	80.5	160.3	98.3	N/A
Flexible Rate	80.5	160.3	98.3	98.0

straints because the average network saturation is still very low and plenty of wavelengths are available. In such a scarcely-loaded network status, 200 Gbps requests are more likely to be blocked due to QoT constraints rather than 100 Gbps requests, that are less SNR demanding. In the high BP regime, we are facing an heavily-loaded network, so wavelength blocking becomes dominant with respect to QoT blocking, and both 100 and 200 Gbps requests will have similar blocking probabilities. However, since 200 Gbps requests carry a traffic that is double with respect to 100 Gbps, 200 Gbps will enable a higher allocated network traffic in such high BP regime, thus reversing the low-BP ranking. The crossing point between the two regimes is close to BP = 1%, for which the average total allocated network traffic is around 98.3 Tbps.

Fig. 3.9b represents the average link saturation of the Pan-EU topology obtained at GoS-BP of 1% for 200 Gbps grooming and multi-rate transceivers. Once again, network most critical links can be identified: in such case links of the northern-EU area connecting Hamburg, Amsterdam, Berlin, and Copenhagen are more saturated than the others. At the same time, the most peripheral ones are less used, once again due to the large SNR degradation they introduce. In Sec. 3.5, some possible upgrades derived from these progressive-traffic analyses are presented.

3.5 SNAP Driven Upgrades

In this section, starting from the quantitative and qualitative evidence of Fig. 3.8b and Fig. 3.9b we evaluate the impact of selective upgrades on network throughput. We consider two different upgrade strategies: HFA

introduction for QoT enhancing, and spatial division multiplexing (SDM) introduction via fiber doubling or overlaying.

3.5.1 Selective HFA Introduction

As first selective upgrade strategy, we consider the introduction of amplification equipment to enhancing QoT of underutilized links. In particular, we upgrade links whose saturation is lower than 20% from EDFA to HFA solutions, enhancing the QoT of the links. The same assumptions of Sec. 3.3.2 are used to compute the benefit of HFA solutions. In particular, we assume HFAs having a 5 dB noise figure. Such selective QoT enhancing strategy is aimed at enabling larger capacity by improving low QoT-ranked paths, thus enabling increasing network throughput. The number of links upgraded in the German topology is 5, whereas it is 9 for the Pan-European topology After applying the selected upgrades, we re-run SNAP to verify variations in BP vs total allocated network traffic curves. Results are reported in Fig. 3.10 and Fig. 3.11, for the German and Pan-EU topology, respectively. Whereas the red and white striped histograms of Fig. 3.12-3.13 show the average saturation per link at BP=1%, compared to results before the upgrade (filled histogram).

Referring to results for the German topology of Fig. 3.10a and Fig. 3.10b, it can be noted that selectively upgrading to HFA 5 links out of 26 (19%), enables an improvement in average total allocated network traffic at BP = 1% of 4%, moving from 160.1 Tbps to 166.3 Tbps. This relatively modest increase is mainly due to the high spectral saturation of links between Cologne and Karlsruhe. The lack of available wavelengths in these links creates a bottleneck for new requests, that are blocked because of the absence of alternative routes with adequate QoT. In the next section, fiber overlays will be used to unlock such bottlenecks. Referring to Fig. 3.10b, it can be observed that the HFA upgrade is useful in increasing the saturation of the northwest links of the German network, but the effectiveness drops for the southern links due to the aforementioned bottleneck. Fig. 3.11 refers to the upgraded Pan-European network scenario, where 9 links out of 41 have been selected for HFA upgrade. Observing Fig. 3.11a, it can be noted how selective upgrades in the amplification technology enable an increase in average total

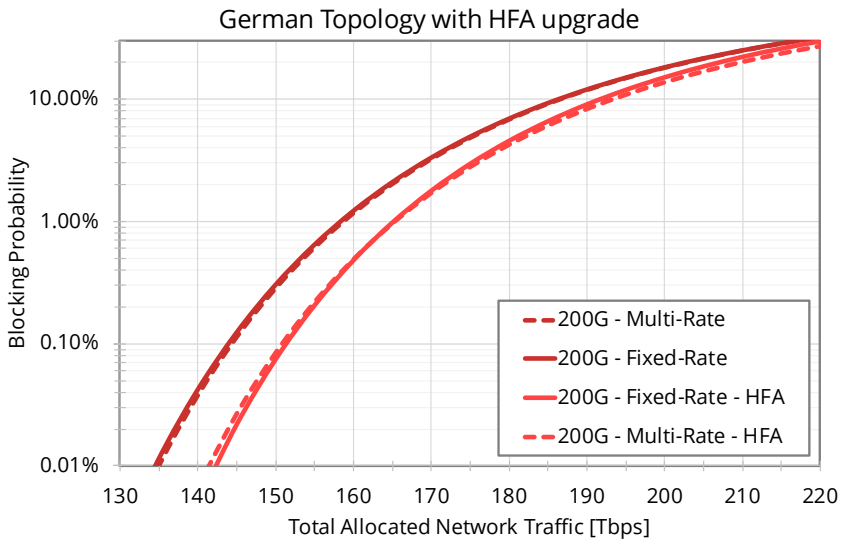

(a) Average blocking probability vs. average total allocated network traffic

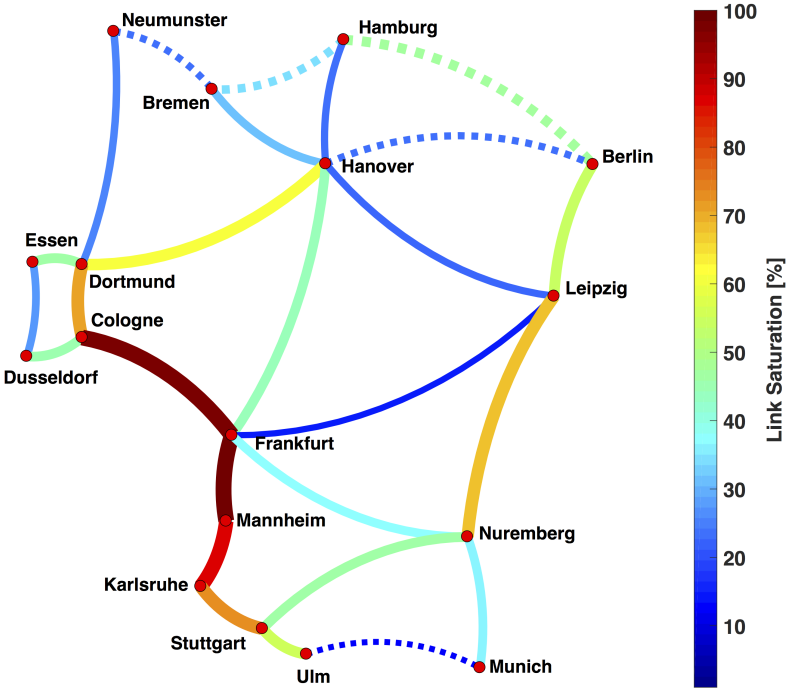

(b) Average links' spectral load at BP = 1%. The ticker the lines the more saturated the links. Dashed lines indicates HFA-upgraded links.

Fig. 3.10 Progressive-traffic results for the German topology post HFA upgrade.

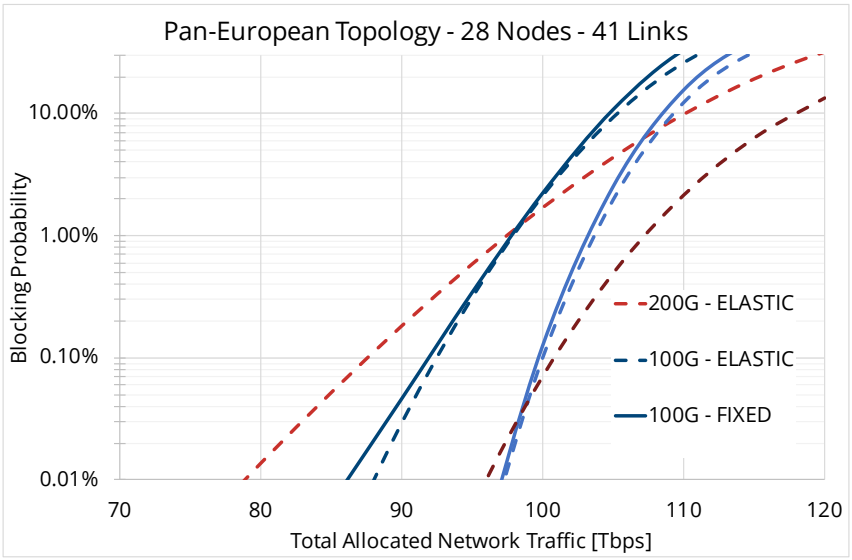

(a) Average blocking probability vs. average total allocated network traffic

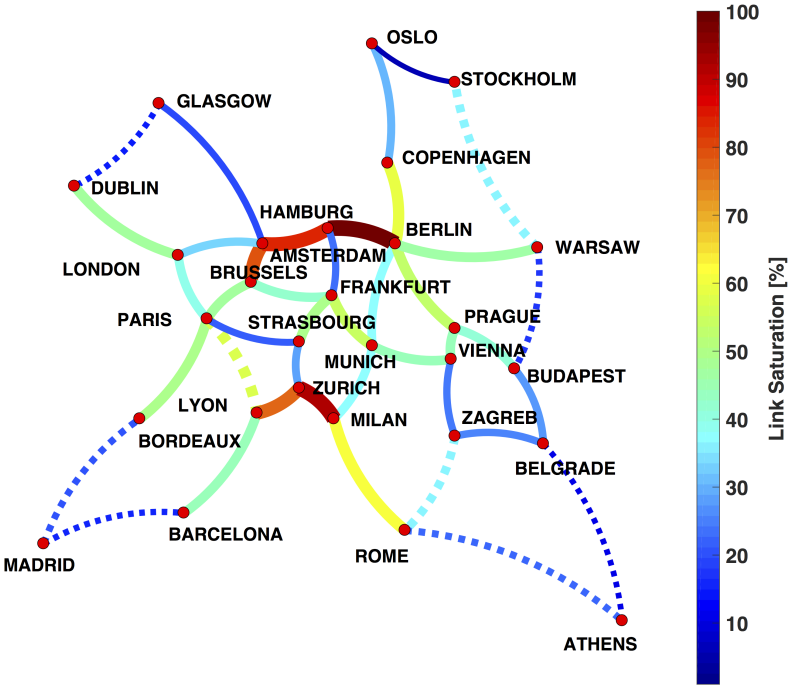

.

(b) Average links' spectral load at BP = 1%. The ticker the lines the more saturated the links. Dashed lines indicates HFA-upgraded links.

Fig. 3.11 Progressive-traffic results for the Pan-Eu topology post-HFA upgrade.

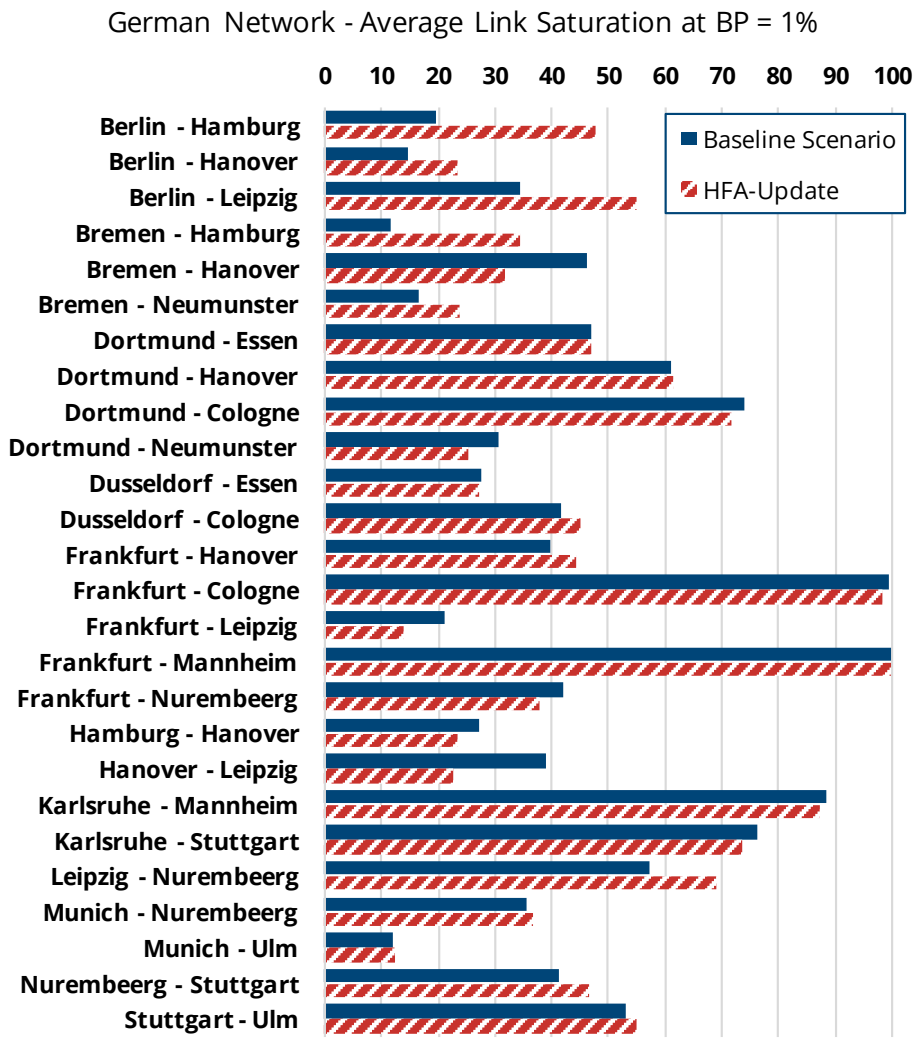

Fig. 3.12 Average link spectral saturation at BP=1% pre and post-HFA upgrades for the German topology

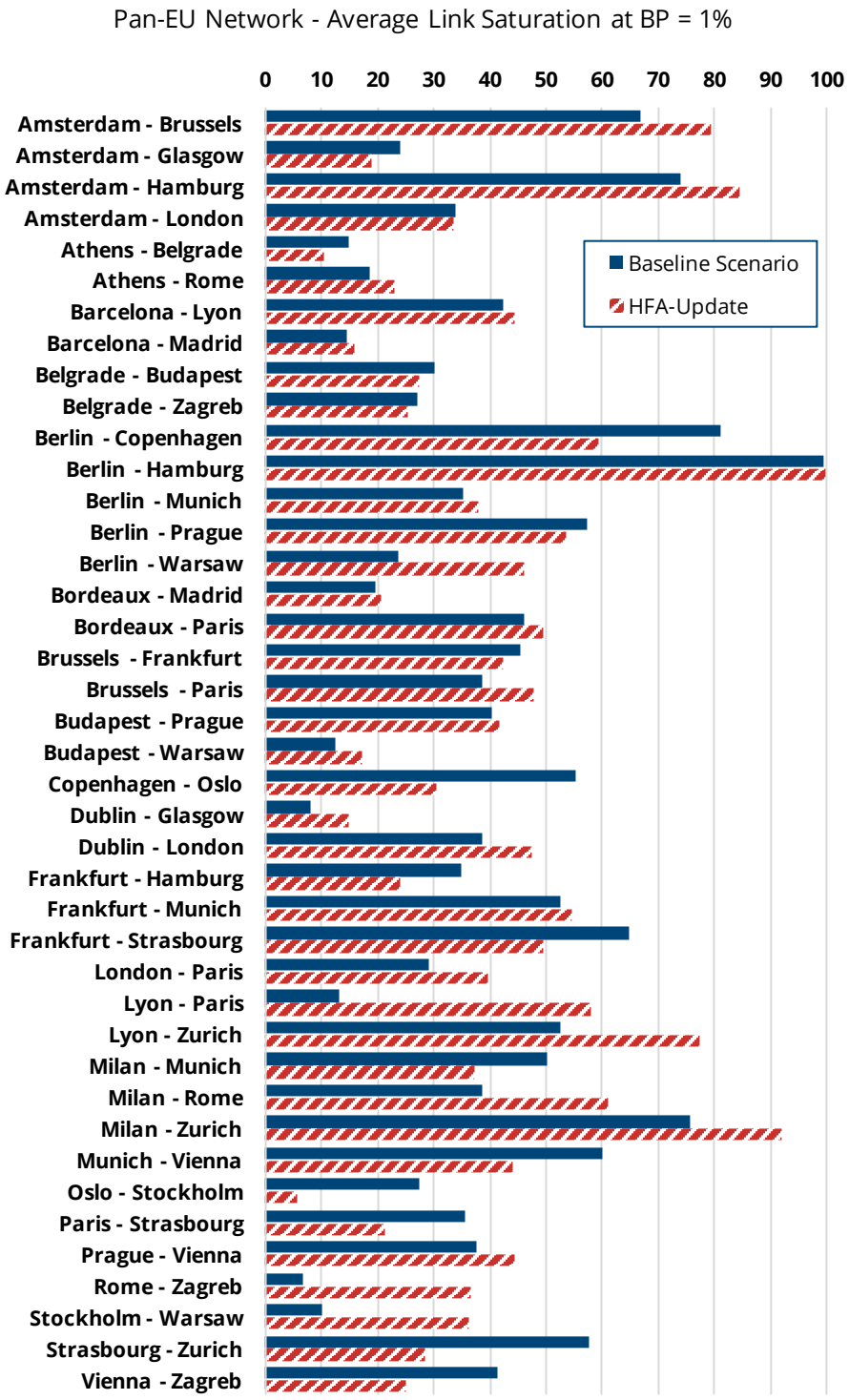

Fig. 3.13 Average link spectral saturation at BP=1% pre and post-HFA upgrades for the Pan-European topology

allocated network traffic of 5% and 9% for fixed and flexible transceivers with $R_G = 100$ Gbps and for multi-rate transceivers with $R_G = 200$ Gbps, respectively. It can be noticed that the crossing point between the two grooming sizes moves down close to 0.01% thanks to HFA upgrading. This is enabled by increased QoT in several network LPs, allowing to transmit more 200 Gbps requests using single PM-16QAM-operated LP allocations, thus increasing the overall spectral efficiency and the network capacity. As far as link saturation is concerned, it can be noted that some of the previously under-utilized links are now more heavily used, thanks to an improved traffic distribution among links enabled by the increase in availability of high-QoT paths. Similarly to German topology, to further improve network capacity one could also consider SDM-based solutions to remove bottlenecks, or further upgrades to physical layer equipment to guarantee an increased QoT in low-SNR links. The first strategy will be analyzed in the next section.

3.5.2 Unlocking Capacity through SDM Upgrades

In this section, we consider SDM solutions as a possible upgrade for unlocking capacity bottlenecks identified through SNAP-based saturation maps. In particular, all links with utilization larger than 80% have been selected and an additional parallel fiber pair is assumed to be lighted up, locally doubling the wavelength availability there. Such solution represents the easiest implementation for the SDM paradigm and is often referred to as fiber overlay. For the German topology, we upgraded the links between Cologne and Frankfurt, Frankfurt and Mannheim, Mannheim to Karlsruhe. Results are reported in Fig. 3.14. From Fig. 3.14a, we can observe that the total average allocated network traffic at BP=1% increased from 155 Tbps to around 255 Tbps, a 64% increase at the expense of a 12% increase in link number. At the same time, a larger average utilization in optical links is experienced as depicted in Fig. 3.14b. For example, breaking the bottlenecks in the western area of the topology, allowed a better utilization of eastern links as well.

For the Pan-European topology (Fig. 3.15), we doubled the link in between Berlin and Hamburg and Berlin and Copenhagen, yielding a 12% increase in capacity, from 98 Tbps to 110 Tbps at BP=1%. In such case, the number

of fibers increased by 7%. The increase of total network traffic is smaller than the previous case due to the average better utilization of links in the northern Europe region: using 80% as threshold for fiber doubling might be too conservative. For both topologies, it is interesting to notice that BP-vs-traffic rankings for different grooming and transceivers implementations are not changed after the upgrade: the considered SDM solution does not change average network QoT, thus low-QoT blocking is not affected by SDM, but wavelength contention induced blocking is. In conclusion, in this section we show how SNAP can be innovatively used to highlight topological bottlenecks and test possible fixes for them, highlighting the versatility of the tool.

3.6 Flex vs Fixed Grid Upgrade benefits.

In this section, SNAP is applied to understand the capacity advantage that is enabled by moving from fixed grid technology, to a fully flex grid one with bitrate and symbol rate elastic transceivers, implementing the elastic optical network paradigm [48], [157]. Several authors have already performed such a comparison [77], [142], [158]–[160], however their effort has focused mainly on estimating the benefit of flex grid technologies due to better spectrum utilization in optical network scenarios, without focusing specifically on mix scenarios where flex grid technologies are introduced in a reserved portion of the spectrum, free from legacy traffic. Furthermore, the capacity comparison in [142], [158]–[160] did not consider the impact of nonlinear interference on network capacity, referring to reach tables for different modulation formats obtained in fixed grid conditions. In this section, we propose a SNAP-based progressive traffic analysis that mainly covers these two aspects, focusing on the Telecom Italia network topology with 44 nodes, and different fiber types obtained from the Idealist project [146].

We focus on a transparent reconfigurable optical network scenario in which legacy, fixed-grid traffic, has been properly defragmented in a continuous region of the C-band, making available a continuous spectral bandwidth for future allocations. We refer to such residual free bandwidth as a percent-

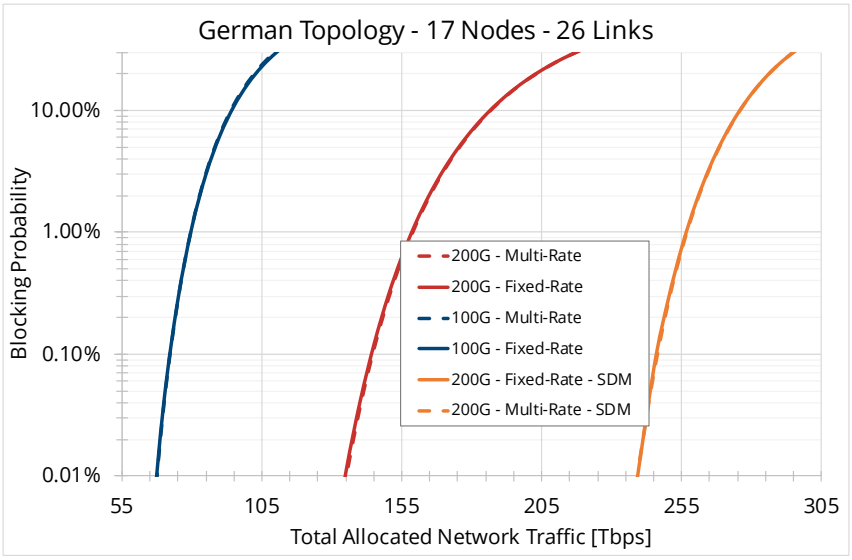

(a) Average blocking probability vs. average total allocated network traffic

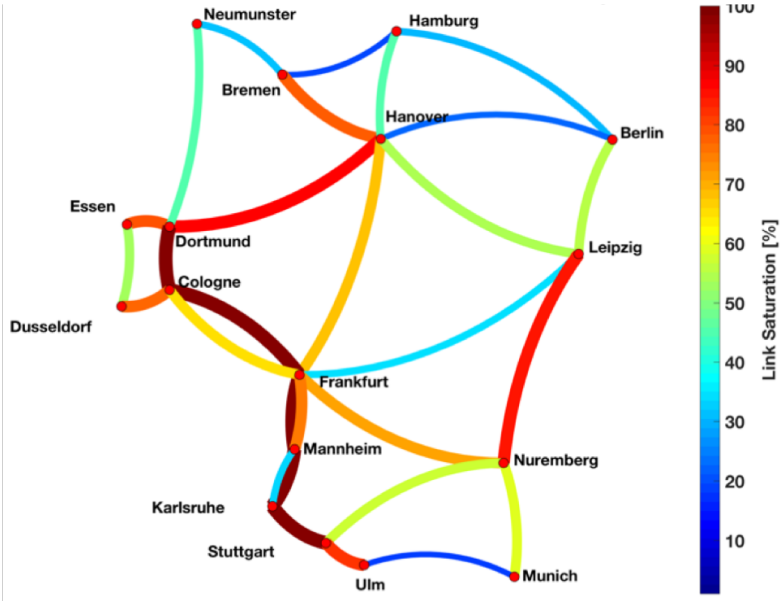

(b) Average links' spectral load at BP = 1%. The ticker the lines the more saturated the links.

Fig. 3.14 Progressive-traffic results for the German topology after selective SDM upgrade.

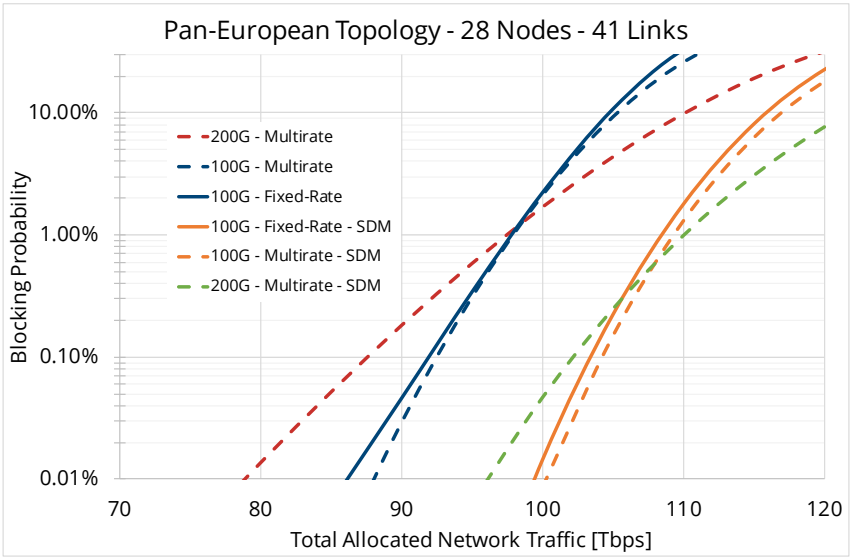

(a) Average blocking probability vs. average total allocated network traffic

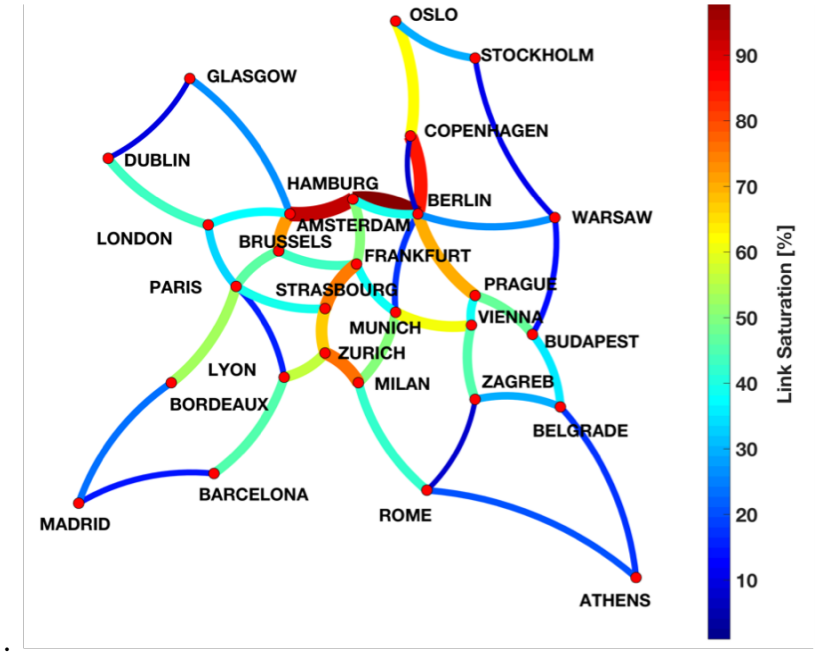

.

(b) Average links' spectral load at BP = 1%. The ticker the lines the more saturated the links.

Fig. 3.15 Progressive-traffic results for the Pan-Eu topology after selective SDM upgrade.

Table 3.2 Achievable net bitrate with bitrate flexbile transceivers over a 37.5 WDM grid.

Modulation Format	**Net bitrate [Gbps]**
PM-BPSK	50
PM-QPSK	100
PM-16QAM	200
PM-64QAM	300

age of the overall 4 THz C-band. We consider different values of residual bandwidth percentage (RBP) from 75% down to 25%.

As traffic model, we consider uniformly distributed random requests with grooming sizes R_G from 20 to 100 Gbps that are progressively allocated on the network. We suppose to exploit residual optical bandwidths using fixed grid with 37.5 GHz slots, or flex grid based on ITU-T standard [161] with 12.5 GHz spectral slots. For both fixed and flex grid we assume to use bitrate elastic transceivers able to vary the modulation format from PM-BPSK up to PM-64QAM using square PM-M-QAM formats via DSP. When considering flex grid upgrades, we assume transceivers to be also elastic in symbol rate, being able to use a number of 12.5 GHz slots N_S up to 5, corresponding to a total symbol rate of 62.5 GBaud. We assume fix grid transceivers to operate using a 31.25 GBaud gross symbol rate, allowing for a 6.25 GHz guardband over the 37.5 grid. We assume a typical 25% coding and protocol overhead, yielding a net symbol rate of 25 GBaud, corresponding to bitrates varying from 50 Gbps to 300 Gbps per channel when using PM-BPSK up to PM-QPSK as shown in Tab. 3.2. For the flex grid case, we assume transceivers to be able to deliver Nyquist shaped channels from 12.5 Gbaud for $N_S = 1$. Supposing the same 25% overhead as for the fixed grid case, each slot is delivering a net symbol rate of 10 GBaud. The full set of combination for N_S and modulation format and the consequent net bitrate values are reported in Tab. 3.3. For flex-grid transceivers we assume to allocate a 6.25 GHz guardband, thus being able to tune transceivers with a 6.25 GHz frequency granularity.

In order to compare these two different implementations, we use a SNAP-based progressive traffic analysis to obtain the average blocking probability vs allocated traffic per spectral unit T. T represents a spectral efficiency as it is measured in Tbps/THz. T is obtained by dividing the total allocated traffic

Table 3.3 Achievable net bitrate with bitrate ans symbol rate flexbile transceivers over a 12.5 WDM grid.

Modulation Format	**Net bitrate [Gbps]**				
	$N_S = 1$	$N_S = 2$	$N_S = 3$	$N_S = 4$	$N_S = 5$
PM-BPSK	20	40	60	80	100
PM-QPSK	40	80	120	140	280
PM-16QAM	80	160	240	320	600
PM-64QAM	120	246	360	480	600

by the available residual bandwidths. Relying on T as target network metric, we can compare how the considered different solutions are able to exploit the available spectrum, consequently giving a *fair* ranking for their use in the considered scenario. Notice that T can be larger than the maximum spectral efficiency of the highest cardinality modulation format of the considered transceivers, i.e. PM-64QAM, as it is an aggregated metric computed by summing all allocated requests on the whole network, i.e. all network links. Metrics are averaged over 5000 Monte Carlo realizations.

As RWSA policy we assume a QoT-based k_{MAX} routing with first fit wavelength/spectrum slot assignment. We assume $k_{MAX} = 50$ to exploit a relevant portion of the full routing space. As QoT parameter we refer to the generalized SNR computed according to the LOGO principle. To have a fair and relatively conservative QoT estimation for fixed and flex grid case, we compute the generalized SNR assuming full spectral load at Nyquist spacing, i.e. continuously filling the full C-band. This assumption entails a slight overestimation of NLI, but it allows to safely model nonlinear propagation impairments for the flex grid scenario, in which spectrum is filled in a highly irregular way due to symbol rate variability of LPs. Transparent amplification via EDFAs with 5 dB noise figure is assumed. ROADM nodes are assumed to have no add/drop or wavelength contention limitation. Nodes are introducing an 18 dB loss that is recovered by an additional booster amplifier. We assume that the considered 6.25 GHz guardband to be large enough to avoid any penalty with respect to cascaded filtering.

In order to exploit as much as possible QoT potentialities of the network under test, we assume to use bitrate overprovisioning in LP allocation. This

means that when allocating a LP, the highest possible modulation format that can be allocated over it based on its QoT is used. If the net bitrate corresponding to that modulation format is bigger than the grooming size of the request being allocated, the remaining bitrate will be used to allocate future requests on the same traffic directory, i.e. between the same nodes' pair. We assume this aggregation procedure to be nondisruptive for existing traffic. If the request cannot fit in the available bitrate of an existing LP, a new LP will be turned on. In case of symbol rate elastic transceivers, N_S is kept as small as possible to allocate a request, to optimize spectral efficiency. N_S is increased if the QoT of the considered path does not allow to use a single spectral slot.

Results in BP vs T are reported in Fig. 3.16. Fig. 3.16a and Fig. 3.16b show the results for the fixed grid and flex grid implementations respectively. Fig. 3.17 shows a comparison between the two implementations at a target BP of 1%, for different grooming sizes R_G and different residual bandwidth percentages. At first glance, it is clear – as from intuition – that the flex grid solution always outperforms the fixed grid one. However, it is interesting to observe that its performance advantage decreases with the increase of traffic grooming size. This is due to the fact that for the flex grid solution, request with larger grooming sizes are forced to be allocated over large spectral areas, e so the advantage with respect to fixed grid is marginal and it is enabled only by the higher SNR LPs for which a high cardinality modulation format – PM-64QAM or PM-16QAM – can carry the groomed traffic on one or two slots as clearly visible from Tab. 3.3.

Each curve of Fig. 3.16 displays a similar two-regime behavior vs. T: first, a steep BP increase with T due to traffic allocation through new LP activations saturating the available bandwidth, then, an evident slope reduction due to the exploitation of over-provisioned LPs. We observe that the regime-changing BP threshold decreases with RBP enlargement because of the larger spectrum portion available for LP allocation, and grows with R_G because of shrinking, on average, of the room left to allocate requests via overprovisioning. Moreover, it is smaller for flex-grid than for fixed grid, given the other parameters, because with flex-grid the number of activated LPs is in general larger. We observe also that curves for flex-grid are much more clustered, proving how this spectral-use performs more independently

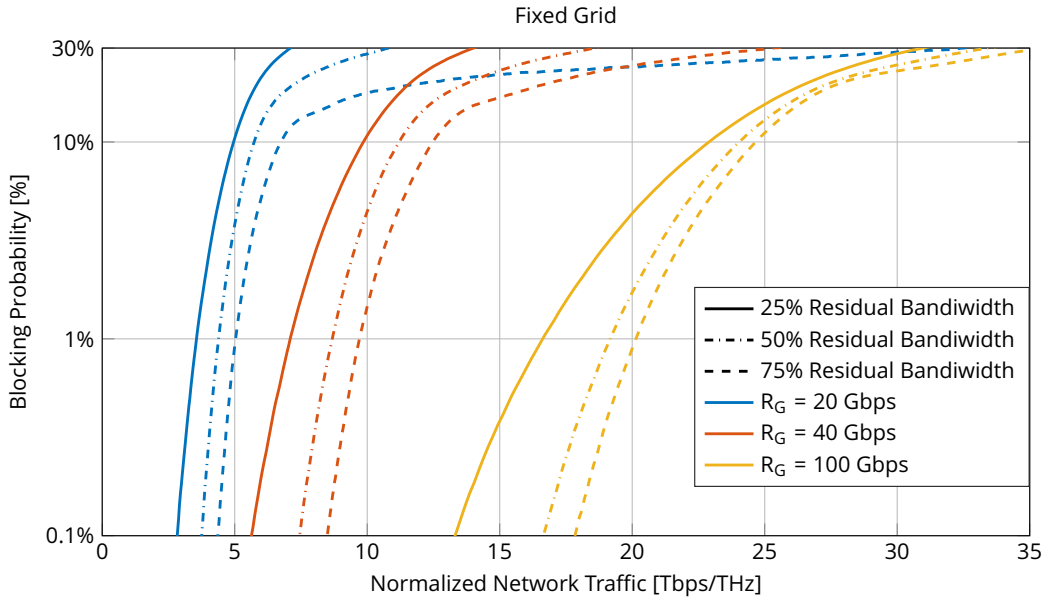

(a) Fixed grid solution

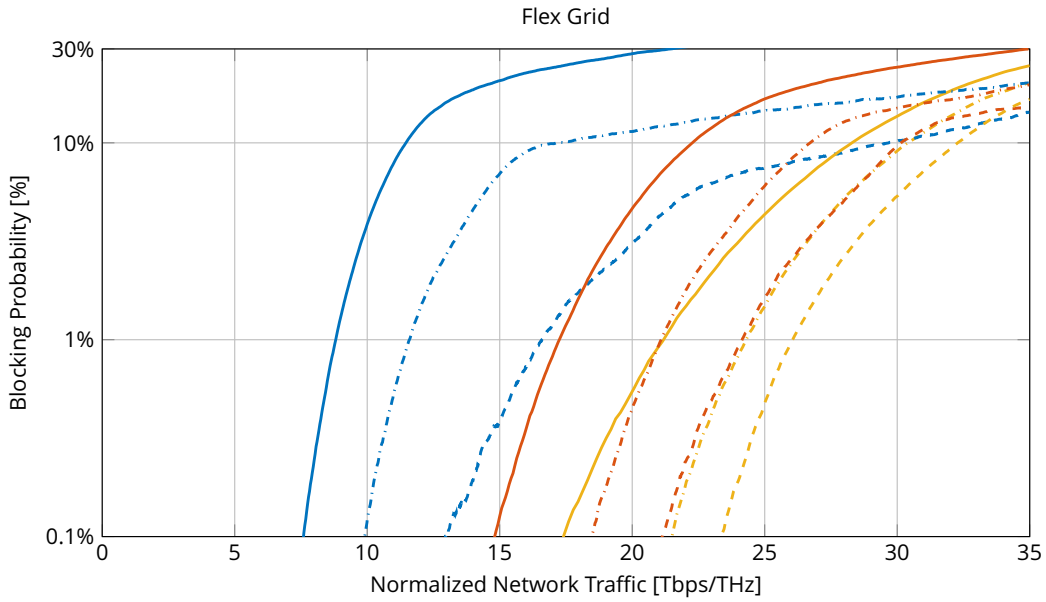

(b) Flex grid solution

Fig. 3.16 Blocking probability against the overall network traffic per available spectral unit for. Blue, red and yellow lines refer to 20, 40 and 100 Gbps of traffic grooming, respectively. Solid, dash-dotted and dashed lines refer to 25% 50% and 75% of residual bandwidth, respectively. Legend is reported only in Fig. 3.16a for space constraints.

of RBP and R_G than the fixed grid solution, for which the advantage of larger R_G is evident. Finally, we observe a saturation effect for flex-grid operated with $R_G = 100$ Gbps, that behaves only slightly better than $R_G = 40$ Gbps. This is due to the limited overall network capacity, that flex-grid enables to better approach.

To summarize results, we set a maximum tolerable blocking probability BP=1% and present the corresponding normalized traffic for all scenarios. Results are shown in Fig. 3.17, where each sub-figure refers to a different grooming size and includes results for RBP of 25%, 50%, and 75%. For all cases, performance hierarchy against RBP follows the intuitive behavior: the allocated traffic per spectral unit at a given BP increases with RBP because of the larger spectral range over which the RWSA algorithm may effectively operate. The growth of T with RBP is larger for flex-grid and decreases with larger R_G because of previously mentioned reasons with respect to better spectral efficiency that can be achieved by the flex grid solution.

Fig. 3.17a displays results for the smallest R_G of 20 Gbps and shows qualitative tendencies taking place also for other cases. The intuitive behavior of larger traffic per residual spectral unit with larger RBP is confirmed for both fixed and flex grid techniques, but flex grid better takes advantage of larger RBP, with a relative gap that grows with the available bandwidth. Analyzing numbers, we observe that with 20 Gbps grooming and RBP = 25%, the fixed grid solution enables an average 3.6 Tbps/THz with respect to an average of 8.8 Tbps/THz of the flex grid with a relative gap of 2.5 times. Moving to RBP = 50%, T grows to 4.4 and 11.6 Tbps/THz for fixed and flex-grid, respectively, corresponding to a relative increase still close to 2.5 times. For RBP = 75%, for which fix-grid enables T=5 Tbps/THz while using flex grid T=16.5 Tbps/THz with a relative gap that goes up to 3.3 times, that is the largest improvement enabled by flex-grid in all the analyzed scenarios. Moving to R_G = 40 Gbps (Fig. 3.17b we observe performances that are close to be double the ones for R_G = 20 Gbps, except for the case of RBP=75% and flex-grid for which network saturation limits the advantages. So, the flex grid advantage with respect to the fixed grid is steady around 2.5 times for all RBPs. Looking at numbers, for RBP = 25% we read 7.1 and 17.3 Tbps/THz; for RBP = 50%, T = 8.7 and 126.6 Tbps/THz; and for RBP = 75%, T = 9.7 and 4.2 Tbps/THz. Finally, for R_G = 100 Gbps (Fig. 3.17c) we can clearly

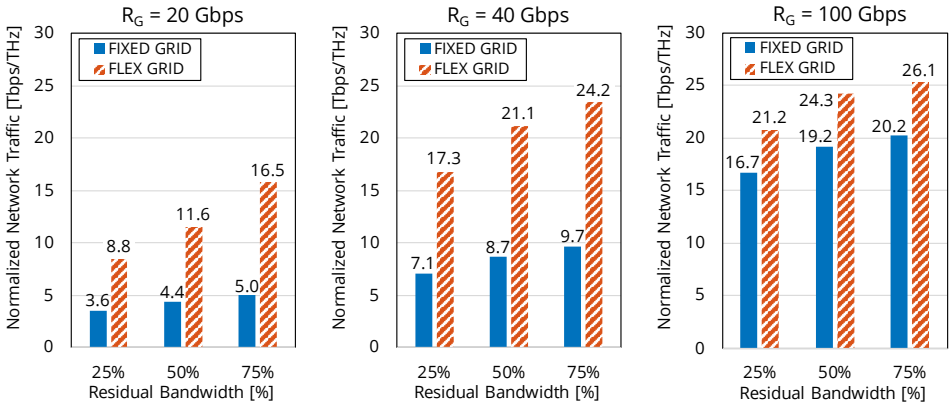

(a) $R_G = 20$ Gbps (b) $R_G = 40$ Gbps (c) $R_G = 100$ Gbps

Fig. 3.17 Network traffic per residual spectra unit at BP=1% for fixed and flex grid implementation vs different residual bandwidths and grooming sizes.

observe the saturation effect already qualitatively remarked in commenting Fig. 3.16b. With respect to the case of R_G = 40 Gbps, for fix-grid, the increase is still similar the ratio between grooming, i.e., 100/40=2.5. While the flex-grid spectral use is quite limited by saturation with an overall traffic per spectral unit that still grows with respect to the R_G = 40 Gbps scenarios, but the flex to fixed grid advantage is limited to a steady value around 1.3 times, independently of the RBP.

3.7 Merit of 2MxN WSSs on network blocking.

In this last example of application, SNAP is used to assess the impact of a recently proposed ROADM architecture for cost-efficient high degree nodes on network performances. Once again, this example is aimed at showing the flexibility of the proposed framework to assess the impact of physical layer solutions on network performances. Furthermore, this example represents a novelty *per se*, as the performance of this device is assessed for the first time to the best of the author's knowledge. The considered ROADM architecture is based on the so-called 2MxN wavelength selective switches (WSSs). These novel devices represent attractive solutions for cost reduction in networks with high average node degree such as metro topologies, at the price of partial wavelength contention in the device. In the next paragraphs we will

first describe the working principles of this novel family of device, and then assess the impact of their partial wavelength contention on network blocking probability using SNAP on a metro topology.

3.7.1 Working principle of 2MxN WSS family.

The requirements for next-generation colorless, contentionless and directionless (CDC) ROADMs include improved cost per add/drop port, increased number add/drop ports (>16), support for more degree ports (>16), channel filtering to improve performances and relax transceiver requirements, and support for high symbol rate transceivers [162], [163]. Current generation of CDC ROADMs leverages on MxN multicast switches (MCS) at add/drop side of the ROADM to achieve CDC capabilities [164], [165]. M represents the degree ports of the ROADM node, and N the number of add/drop ports. However, MCS based solutions do not scale well with the add/drop port count as EDFA arrays are required to overcome MCS splitting losses causing a degradation in linear SNR performance. Furthermore, EDFA arrays can leverage uncooled operations up to 16 add/drop ports, making the implementation for higher port count not practical [162], [163]. MCSs are also not attractive for high port count devices as they are filterless, thus causing performance degradation as noise generated by different transceivers is combined in the MCS causing linear SNR degradation across the WDM comb. A CDC ROADM based on MCS technology is depicted in Fig. 3.18. Each of the M degree ports is connected to a 1xN power splitter, so no wavelength filtering is present. Each of the N add/drop ports can be coupled to any degree port of the device by N Mx1 selector switches. Up to M instances of a given wavelength can be routed through the device without contention. EDFA arrays recover power splitters losses introducing additional impairments.

A possible alternative with respect to MCS-based ROADM is represented by MxN WSS based ROADMs [163], [165]–[167] in which the edge CDC functionality is implemented by an MxN WSS rather than a MxN MCS. Thanks to inherent filtering capabilities of WSSs, and lower splitting losses, this solution enables better performance by reducing noise accumulation and eliminating the need for EDFA arrays. A MxN WSS based ROADM is shown in Fig. 3.19. The functionality of this device is similar to the MCS-based one,

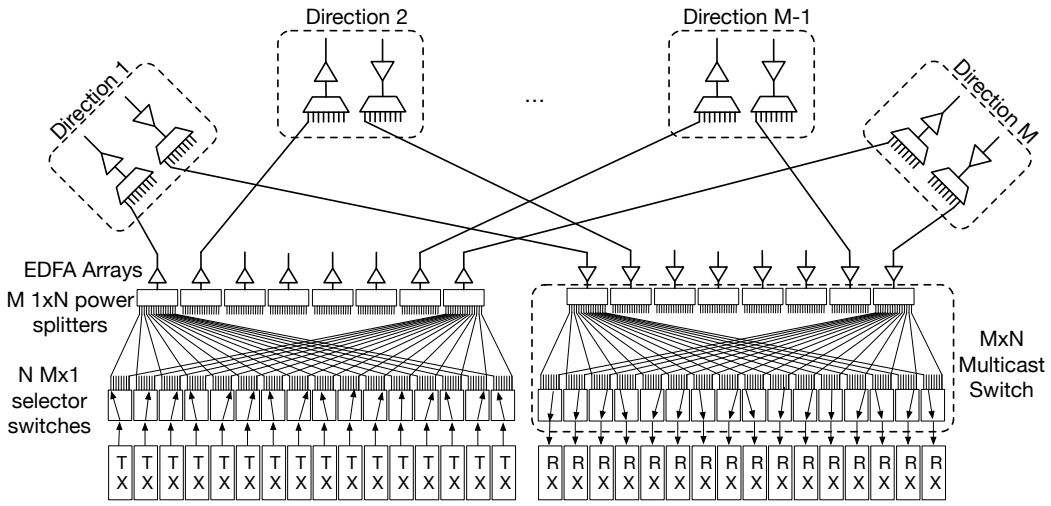

Fig. 3.18 MCS-based CDC-ROADM for a MxN node. Not all connections are shown for sake of clarity.

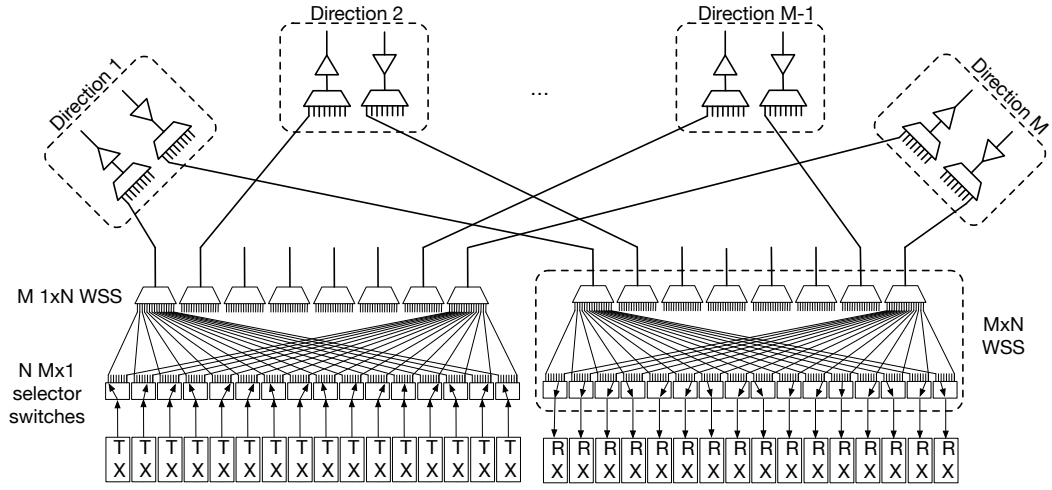

Fig. 3.19 WSS-based CDC-ROADM for a MxN node. Not all connections are shown for sake of clarity.

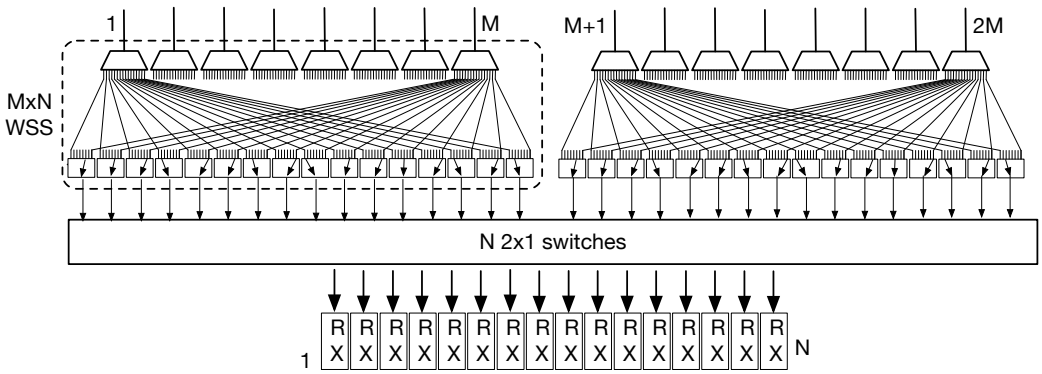

Fig. 3.20 WSS-based CDC-ROADM and pay-as-you-grow configuration for high degree count nodes.

but the M 1xN power splitters are replaced by M 1xN WSS. Thus individual wavelengths can be routed independently to any of the N add/drop ports and EDFA arrays are removed as losses are smaller. Unfortunately, the cost and complexity of an MxN WSS increase in proportion to the degree count, making the cost per add/drop port increase as the system grows in complexity with higher degree nodes [163]. This is mainly due to technological constraints imposed by the WSS switching engine that is implemented with Liquid Crystal on Silicon (LCOS) technology that has limited beam steering capabilities and thus requires cost, size, and complexity increase to achieve high degree counts [163], [167]. A possible solution to overcome such limitation is depicted in Fig. 3.20 where two MxN WSSs are connected by an external bank of 2x1 switches. However, this approach more than doubles the cost per add/drop port and can lead to excessive operational burden also due to the large footprint of this solution due to the additional switches.

A recent proposal to overcome such limitations is depicted in Fig. 3.21. In such architecture, a doubling in degree count is achieved by sharing a 2xN WSS over two-degree ports forming a 2MxN switching configuration. In such case, the complexity and cost increase are minimal with respect to a MxN WSS-based configuration, but the cost per add/drop port supporting 2M degrees is less than half of that of the architecture of Fig. 3.20. Similar considerations can be made with respect to the density of this solution, that has a footprint that is half with respect to Fig. 3.20. All these positive aspects are traded off with partial wavelength contention in the degrees M+1

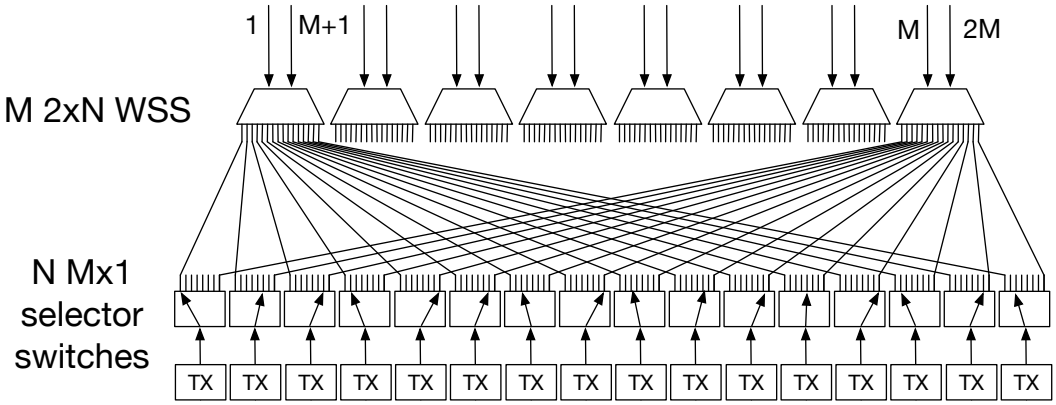

Fig. 3.21 2MxN WSS for high degree count nodes. Degrees sharing a 2xN WSS are affected by wavelength contention.

to 2M, as the same wavelength cannot be routed over the two directions that share a 2xN WSS. In the next paragraph, the impact of such limited contention on network blocking probability will be assessed through SNAP-based progressive traffic analysis.

3.7.2 SNAP-based blocking probability analyses

We use SNAP to assess the impact of the 2MxN WSS solution on network blocking probability up to saturation on a high nodal degree, highly meshed metro network topology. The considered topology is made of 40 nodes and 107 links, with an average node degree 5.35, with minimum and maximum node degree equal to 2 and 14, respectively. More details are reported in App. A. As the average node-to-node distance is 12.6 km, we do not consider fiber propagation or noise accumulations as limiting effects to LP allocation. Furthermore, as we are focusing only on the limits imposed by the wavelength contention constraints of the architecture of Fig. 3.21, we consider as the capacity metric the number of LPs that are successfully allocated during the SNAP progressive load. For the same reason, progressive random traffic requests are assumed to be generic LP connection requests, so as to decouple the obtained network results from line terminals and propagation impairments. As RWA policy, a hop-count based k_{MAX}-shortest path policy with first fit wavelength assignment has been used. k_{MAX} has been set to 200, to exploit the high average node degree of the topology under test, and to

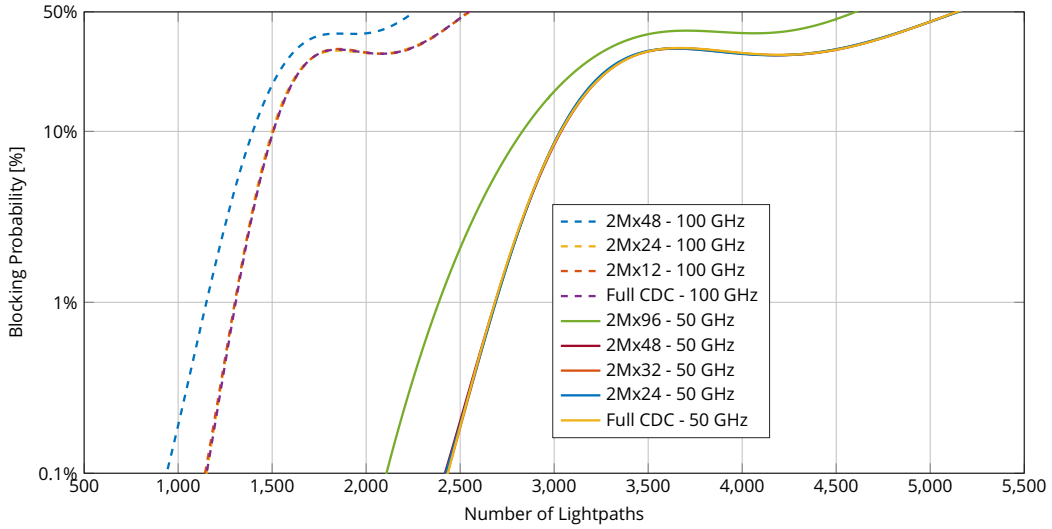

Fig. 3.22 Blocking probability vs number of allocated ligthpaths for different WSS architectures with 100 GHz and 50 GHz grid.

provide a routing space large enough to avoid wavelength contention at fiber level as much as possible. Links are assumed to carry a number of channels $N_W = 96$ over the 50 GHz fixed grid, or $N_W = 48$ wavelengths over the 100 GHz grid. Network metrics have been averaged over 5000 traffic realizations up to network saturation.

We compare 5 different ROADM architecture: using as reference full CDC ROADM, we study the impact of wavelength contention of 2MxN WSS devices assuming the number of add/drop ports $N \in \{24, 32, 48, 96\}$ for the 50-GHz grid, $N_W = 96$ channels links, and $N \in \{12, 24, 48\}$ for the 100-GHz grid, $N_W = 48$ channels links. As a first analysis, in order to perform a fair comparison between different scenarios, we suppose that the add/drop capability of each node is 100%, meaning that each node can add/drop N_W channels in each direction. This entails that in each node has N_W/N devices for each direction. Such an assumption will be verified *a posteriori* by counting the number of ROADMs actually needed in each node to sustain the traffic load, at different blocking probability. Later, the analysis will be repeated by assuming different levels of add/drop capability, to verify if such a posteriori evaluation is valid.

Fig. 3.22 shows the network blocking probability vs the number of allocated LPs for different ROADM architectures and WDM grids. Apparently,

only four curves are visible. his is because for both grid spacings, all results for N up to $\frac{1}{2}N_W$ display the same performances as blocking probability vs LP count. Only when the most restrictive architecture $N = N_W$ is deployed, a contention penalty can be observed and estimated to be in the range [6%; 16%] for the 100 GHz grid and in [6%; 13%] for the 50 GHz one. Considering, for example, a target blocking probability of 1%, the penalties for both grid spacings and $N = N_W$ are equal to approximately 12%. This behavior shows that the proposed node architecture is not inducing wavelength contention blocking if the number of add/drop ports is kept below $\frac{1}{2}$ the number of total wavelengths. Keeping the attention on Fig. 3.22, for every displayed curve, we can notice three different regimes that will be discussed later commenting the effect of the proposed node architecture. For BP roughly lower than 10%, BP's growth with the number of LPs is steep and constant, meaning that in such low-BP regime, each failed connection allocation has a relatively large impact on the overall network. Then, after a transient, for BP roughly higher than 30%, the curve flattens: in such regime, the value of BP is large, therefore each failed connection allocation has a much smaller impact on the overall BP. In this regime, the network topology is able to absorb traffic without enlarging the ratio of blocked requests. Finally, BP starts to grow rapidly again as the network is close to saturation. The results of Fig. 3.22 may suggest that deploying the proposed architecture is always convenient, as it allows a 50% cost saving with respect to a full CDC architecture, but additional analysis with limited add/drop capabilities – i.e. a limited number of devices – are needed. To this purpose we first count the average number of WSS devices that are actually needed, on average, to allocate the progressive traffic requests that have been allocated up to a certain target probability, and normalize this number over the degree of each node. We do this, to understand if full add/drop capability in each direction is actually needed, at a target blocking probability. We consider this metric both globally – i.e averaged over the full set of nodes – and locally – i.e. individually on each node. Fig. 3.23 represents the average number of WSS per node per direction averaged over the full topology. We notice that up to blocking probability of 20%, this metric slowly grows around 1 for the 100 GHz grid and around 1.2 average WSSs/node/direction for the 50 GHz grid. This phenomenon takes place independently of the number of the actual number of WSS ports, mean-

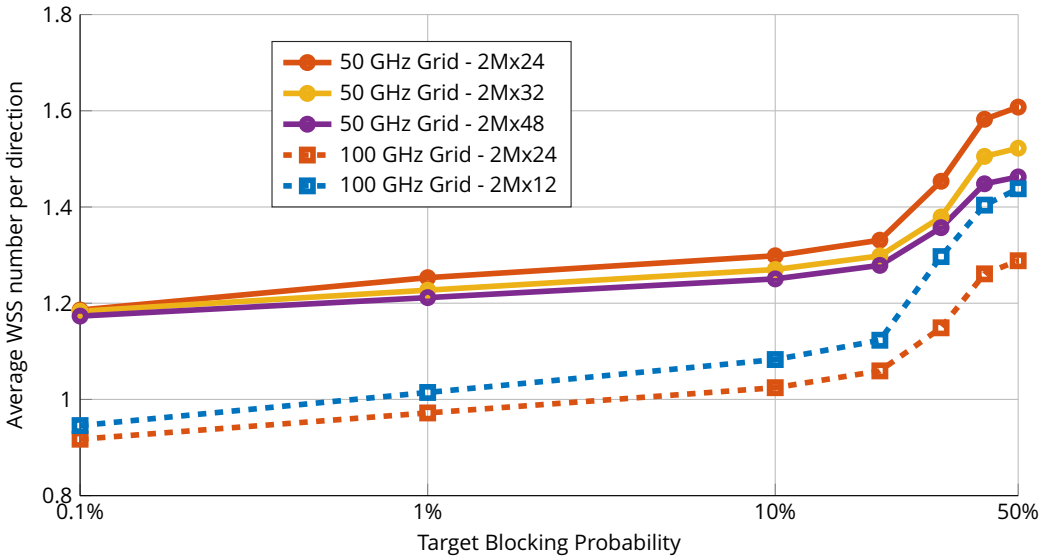

Fig. 3.23 Average number of required WSS per node per direction for two different grid spacings and WSSs architectures.

ing that few selected nodes need WSS-replication at target BP<20%, thus, port utilization count is -– on average -– smaller or equal than the smallest considered N. As the target BP becomes larger than 20%, architectures with small N values requires a larger number of average WSSs/node/direction (up to 1.6 average WSSs/node/direction for N=24 in the 50GHz-grid case). Note that this analysis is not significant for $N = N_W$ as such utilization metrics will be equal to 1. Node-level results are qualitatively reported in Fig. 3.24, where we visually report the average number of WSS devices per direction by means of the node size, using the scale reported in Fig. 3.24a. We consider the network topology under test deploying 2Mx24 (Fig. 3.24a and Fig. 3.24b) and 2Mx48 (Fig. 3.24c and Fig. 3.24d) WSSs with 50 GHz grid spacing for two different levels of blocking probability, i.e. 1% (Fig. 3.24a and Fig. 3.24c) and 40% (Fig. 3.24b and Fig. 3.24d). It can be observed that Fig. 3.24a and Fig. 3.24c – both obtained at 1% blocking probability – are similar, even though the node architecture is different. This means, that on average each node requires the around 1 WSS per direction, as the number of wavelengths added/dropped per direction is – on average – smaller or equal than 24. A small difference can be seen in the peripheral nodes of the topology, that in the $N = 24$ case are slightly bigger than the $N = 48$ scenario. Fixing the node architecture and comparing these results at different

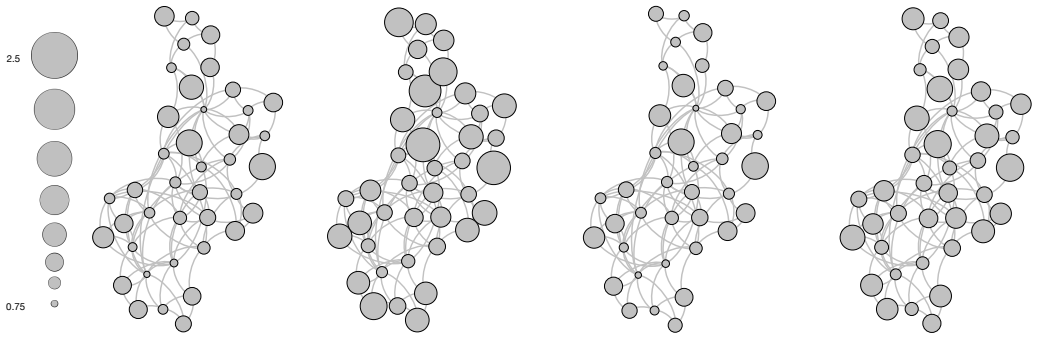

(a) 2Mx24 WSS - BP = 1% (b) 2Mx24 WSS - BP = 40% (c) 2Mx48 WSS - BP = 1% (d) 2Mx48 WSS - BP = 40%

Fig. 3.24 Qualitative description of required number of WSSs per direction in each network node, for two different node configurations (2Mx24 and 2Mx48) and two different target blocking probabilities (1% and 40%). All 4 cases refer to the 50-GHz grid scenario. Node sizes varies from 0.75 to 2.5 WSS/direction.

blocking probability, it is clearly evident how for the 2Mx24 architecture, the average number of WSS per direction in each node increases substantially with respect to the BP=1% case, being for the majority of the nodes larger than 2. For the 2Mx48 architecture instead, a small increase of required WSS in each node is visible when moving from BP=1% (Fig 3.24c) to BP=40% (Fig. 3.24d). In such case, however, the majority of nodes require around 1.5 WSSs per direction.

As a final analysis, we verify if the average requirements in terms of WSS devices per node per direction derived from the previous analysis entail an allocation penalty during node allocation. To do so, we limit the add/drop capability per direction in each node. The results of these analyses are shown in Fig. 3.25, where the 2Mx24 and 2Mx48 WSS architectures are compared against a full-CDC implementation over the 50 GHz grid imposing limitation of the add/drop capability in each node. Namely, we focus on two different levels of add/drop capability: 25% and 50%, meaning that the total number of channels that can be added or dropped in each direction of the node is either 25% or 50% of the total. These limitations are directly correlated to the number of devices deployed in each node: assuming a node of degree M, imposing a 50% add/drop capability per direction means to deploy either 2 2Mx24 WSSs or 1 2Mx48 WSSs. Obviously, 2Mx48 devices can only be used to achieve 50% add/drop capability. The curves of Fig. 3.25 corresponding

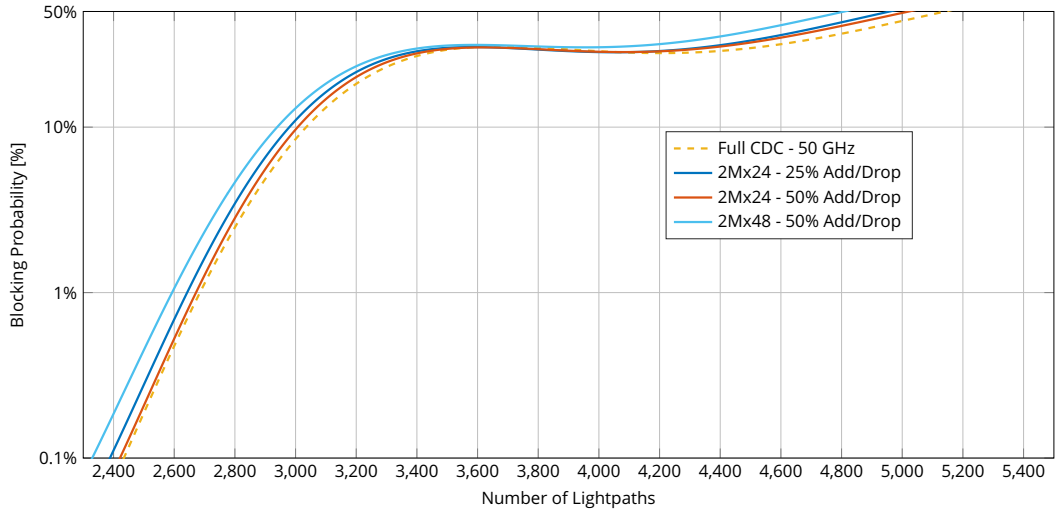

Fig. 3.25 Blocking probability vs number of allocated ligthpaths for of two different WSS architecture with different levels of add/drop capability.

to limited add/drop capabilities (solid curves) show a penalty with respect to the full-CDC penalty. We do not report 2Mx48 and 2Mx24 curves with full add/drop capability as they are practically indistinguishable from the full-CDC curve as shown in Fig. 3.22. As it can be reasonably expected, different solutions are ranked in terms of increasing penalty, as follow: 2Mx24 with 50% add/drop capability, 2Mx24 with 24% add/drop capability, and 2Mx48 with 50% add/drop capability. These different configurations do actually rank in terms of node architectural flexibility: the least-penalty solution has the smallest level of contention while having a number of ports large enough to accommodate the add/drop requests. The second-best one, faces some extra penalty due to the limited number of add/drop ports, although the WSS-level contention probability is the same as the previous case. Finally, the worst performing solution, although having a large of ports, have a higher contention probability at the WSS-level hence larger network level blocking. These penalties are however quite limited with respect to the full-CDC case. Referring to a target blocking probability of 1%, the maximum penalty is 3.4%, while the minimum one is smaller than 1%. With increasing BP, hence increasing network saturation, these penalties get larger. At BP=40%, the maximum penalty is around 7%, while the minimum is 2.6%. These results show that wavelength contention at a fiber level still remains the main limiting cause for network blocking.

The results discussed in this section prove that the proposed 2MxN WSS architecture does not yield relevant additional network blocking penalties in the highly meshed, high node count metro network topology under test. The considered node architecture can be a promising solution for cost, space, and power effective deployment in metro networks.

3.8 Conclusions and next steps.

In this chapter, the Statistical Network Assessment Process has been introduced and several examples of application of this method have been given. As highlighted throughout this chapter, SNAP aims at delivering an unbiased general assessment of the merit of different physical layer technologies on network performances, to assess technologies during the design phase, and to identify topological bottlenecks and test possible solutions. The examples of application proposed in this chapter represent a portion of the results that have been published in literature during my PhD program. Other examples of applications of SNAP include assessment of digital back propagation impact on OEO savings [168] impact, DSP [169], HFAs on OEO regenerators savings [170], comparison of different physical layer models for network capacity assessment [139]. The full list of publication is reported at the beginning of this thesis.

Chapter 4

QoT Estimations for Network Design of Multi-Vendor Networks

In this chapter, the activities that have been performed in the context of the development of a vendor-agnostic QoT estimation tool for the design of multi-vendor networks will be described. Specifically, the activities performed within the Physical Simulation Environment (PSE) group of the Telecom Infra Project (TIP) [46] will be discussed. The topics described in this chapter represent open research problems, therefore only a limited set of results is presented.

4.1 QoT Estimation for Vendor-Agnostic Network Design.

In this section the activities carried out in the PSE group of the TIP consortium will be shortly discussed.

As discussed in the introductory chapter, the dramatic increase in data traffic is forcing operators to disaggregate optical network architectures in order to achieve TCO reduction. This practice leads to a push in exploring multi-vendor optical networks disaggregating hardware and software focusing on interoperability. In this paradigm, operators are responsible for ensuring the performance of such disaggregated architectures. Thus,

operators and vendors are collaborating in defining control and data models that can be promptly used by off-the-shelf controllers [45]–[47]. However, node and network models are only part of the answer. To take reasonable decisions, controllers need to incorporate logic to simulate and assess optical performance. Hence, vendor-independent QoT estimators are needed. Given their vendor-agnostic nature, operators and vendors must work together to jointly define them. These activities have the potential to change the way optical networks are designed and controlled. Firstly, an agreed QoT module enables operators to simplify deployment by planning for vendor-neutral implementations rather than relying on closed source vendor planning tools. Secondly, system integrators are empowered to pick & choose optical components from various vendors thereby designing networks fulfilling high standards while keeping costs down, built in a manner that can be simulated and confirmed by a neutral performance estimation. Thirdly, system vendors will be equipped with the necessary performance benchmark for their product offering by providing a stable base for cost/performance decisions in the design. The PSE group of the TIP consortium aims at developing one of such vendor agnostic QoT estimators, and during my PhD we took part in some key development efforts to create the GNpy library [171]. GNpy is a Python library aiming at QoT estimation for transparent optical network scenarios. One of the modules of GNpy is the so-called Optical Link Emulator (OLE) that is a Gaussian noise model-based tool to estimate the generalized SNR of multispan optical links. OLE has been fully developed in Politecnico di Torino, and part of my PhD activities over the last months related to its development. The OLE requirements have been defined by PSE as follows:

- the tool must output generalized SNR information for a comb of channels that is given as input;
- the tool must include both linear and nonlinear SNR estimations;
- the tool must deliver *local* information, making use of *local* models, i.e. related individually to each network element (e.g. a fiber span);
- the tool must process data with computational times that are compatible with realtime operations so that the tool could be integrated into realtime network controller and orchestrator;

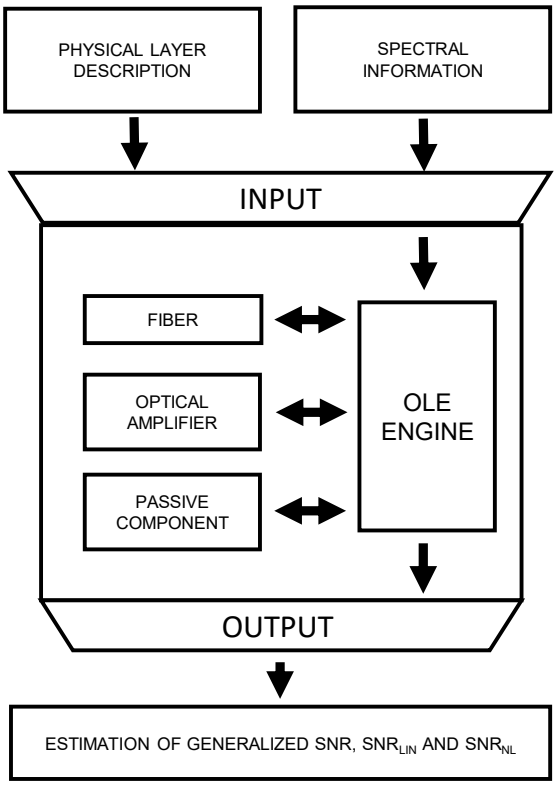

Fig. 4.1 The Optical Link Emulator architecture.

- SNR estimations should fall ± 0.75 dB from measured data.

Based on these requirements, that OLE architecture has been defined as described in Fig. 4.1. OLE uses as input a description of the physical layer, i.e. the architecture of the link under test, and a set of spectral information describing the optical spectrum that propagates through the link. The architectural information is mapped to a component library for instantiating each network element. The component library includes three different classes: fiber, optical amplifier, and passive component. Each of these objects makes use of the set of spectral information to compute linear, nonlinear and generalized SNR variations introduced by each element. To do so, the three library elements make use of a linear and nonlinear engine to compute linear and nonlinear noise contributions and the related signal degradations. The linear engine simply starts from the noise characterization of the components – i.e. their noise figures – to compute the generated ASE noise as described in 2.3. Provided that optical components that are part of the considered route are

well-characterized, including details about their insertion losses, gain and frequency variations of their noise figures, the evaluation of the linear SNR is a trivial aspect with respect to modeling. However, correctly estimating linear noise is fundamental in generalized SNR evaluations as the ASE noise power is – at optimum power – twice as large than NLI noise, thus twice more relevant for accurate QoT estimation.

Due to the requirements imposed by PSE in terms of model *locality* of the estimation for each network element and due to the computational time constraint of the modeling solution, the incoherent Gaussian GN model was selected as modeling option of choice for nonlinearity estimation. Two versions of the GN model were implemented, the GN model reference formula, i.e. the double integral described by Eq. 2.8 in Sec. 2, and the closed form formulae given by Eq. 120 – Eq. 124 in [88]. These two implementations have been tested against SSFM simulations, and both have been shown to be equally precise in nonlinearity estimation. Results of this comparison are not shown in this chapter as they do not present any scientifically relevant information, but rather they represent a common testing procedure for software development.

The OLE source code, together with the full PSE GNpy module is available at [171], where it is constantly updated and improved by the TIP community.

4.2 OLE Validation against Commercial Testbeds.

A key requirement for the successful development of a vendor-agnostic QoT estimation tool is the validation against commercial equipment. Between August and October 2017, OLE has been validated in three different testbed by three different operators, namely Orange [172], Facebook [173] and Microsoft [174]. During my PhD activities, I was involved in the validation tests performed at Microsoft, that represented the most comprehensive experimental testing of the OLE. The full set of results has been published in [174]. The Microsoft testbed, as depicted in Fig. 4.2, is made of approximately 2000 km of mixed optical fiber operated with a commercial open line system (OLS) mixing both SMF and NZDSF fibers. Spans are amplified by either EDFA or

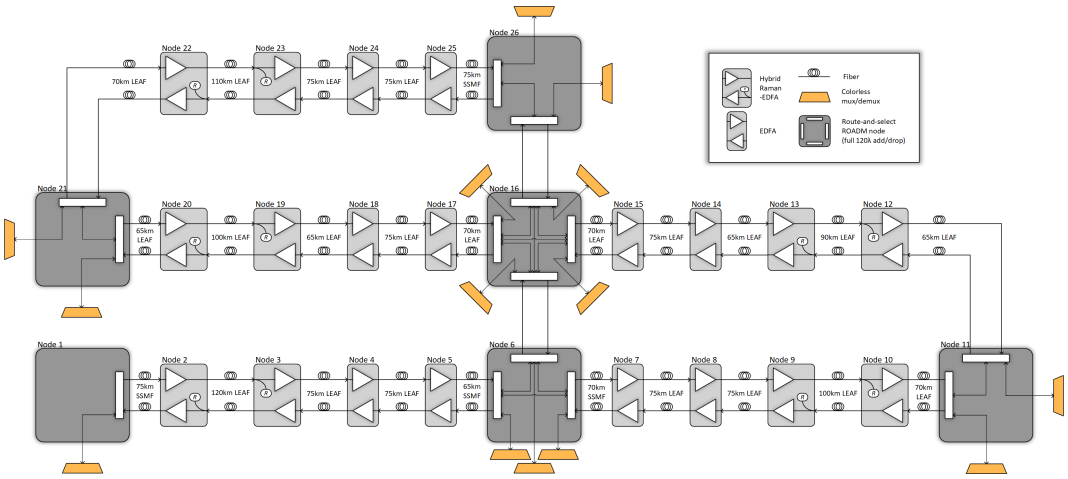

Fig. 4.2 Microsoft testbed for OLE validation.

HFA solutions. The OLS features a colorless, directional architecture with full SDN-enabled support for alien wavelengths. The mostly NZDSF fiber plant spans 1945 km bidirectionally and is roughly made up of 85 percent Corning LEAF and 15 percent Corning SMF-28e LL.

OLE was tested by comparing its generalized SNR estimations with real-time measurements performed over a set of 32 channels generated by commercial linecards by eight different vendors (Acacia, Arista, Ciena, Cisco, Coriant, Infinera, Juniper, and Nokia). All linecards feature variable modulation and Nyquist pulse shaping with symbol rates ranging from 33 to 45 GBaud depending on supplier. In the experiment, PM-8QAM was employed, and with sources featuring conventional star-8QAM constellations, multi-dimensional 8QAM implementations, and/or digital subcarrier modulation. Electro-optics employed include both silicon photonic (SiP) and indium phosphide (InP) processing technologies. All channels were carrying PM-8QAM modulation formats These channels were co-propagated with shaped ASE noise and PM-8QAM bulk modulated channels to achieve a total spectral occupancy of 94 channels over a standard 50 GHz grid, i.e. approximately 4.7 THz of spectral occupation. Fig. 4.3 represents the power spectral density of the transmitted WDM comb.

The measurement methodology was as follows. The optical sources from the eight suppliers were each characterized in a B2B noise-loading setup, with BER vs linear SNR curve measured for each device. These characterizations

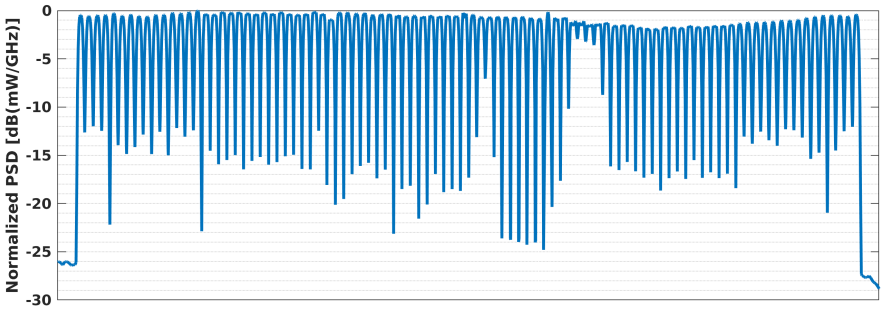

Fig. 4.3 Normalized power spectral density of the transmitted multi-vendor channel comb for OLE testing.

were then used to map measured BER values after propagation to generalized SNR values for comparison with OLE output. This mapping is assumed to be valid assuming no chromatic dispersion and nonlinear penalties for the different DSP implementations. The full 94 channels WDM comb was propagated over the fiber test bed, and BER was captured at five different distances, i.e. 1945, 1540, 1165, 800, and 410 km.

We compared the experimentally derived generalized SNR values with OLE estimations. OLE has been used to derive nonlinear SNR estimations using as input the channel power levels at the input of each span that have been obtained from the processing of monitoring data obtained from the OLS interfaces of the line amplifiers. The line system reported the power level of the channel with the largest PSD computed over 12.5 GHz, thus we used this information together with spectral measurement obtained by tapping out the signal of each line amplifier and analyzing it with an Optical Spectrum Analyzer (OSA), to obtain exact power levels of each channel, taking into account ripple and tilting effects. Furthermore, we exploited the same spectral measurements to compute linear SNR values after each amplifier by integrating the measured PSD over each channel bandwidth to obtain the channel power. Even though PSD measurements include in bandwidth NLI noise, as NLI power is much *smaller* than channel power levels, the integration of the measured PSD yields a sufficiently accurate estimation of the channel power levels without overestimating it due to in-band NLI. Similarly, we integrated the noise levels at the side of each channel over a 12.5 GHz bandwidth, and then scale the obtained value

over the channel bandwidth, assuming flat ASE noise and no relevant NLI contributions outside of the channel bandwidth. To obtain the linear SNR, we computed the ratio of these two quantities. We did not directly use noise figure values provided by the OLS supplier in OLE as they yielded too conservative linear SNR results, as they noise figure values referred to end of life (EOL). This process proved to be quite cumbersome, thus in the future will be fundamental to streamline such a workflow, either by using characterization data of noise figure vs gain of the amplifiers directly provided by vendors, or by improving the output of the OLS monitoring interfaces both in terms of comprehensiveness (e.g. full set of power per channel) and accuracy. As these efforts need to be shared among vendors, system integrators and operators, consortia like TIP represent the ideal working groups to target these goals.

Fig. 4.4 includes summary results of the validation for the five considered distances. Fig. 4.4a-4.4e show the SNR measurements (red diamond-marked curves) and OLE estimations (blue dot-marked curves) vs frequency for the 27 central frequency values of the commercial line cards used for the comparison. OLE estimations are surrounded by a ± 0.75 dB region to show the target accuracy boundaries dictated by PSE. Fig. 4.4f shows the box plot for the absolute value of the relative estimation error (in dB) vs distance. It is worth to mention that these results represent also the first validation of the GN-model in a mixed-fiber scenario with commercial linecards. For all distances, a good agreement can be found between measurements and OLE-based estimations within the target ± 0.75 dB range.

In Fig. 4.4a, the low-frequency points are omitted as too large an extrapolation from B2B measurement was needed to estimate their generalized SNR values. In Fig. 4.4e, the results at 193.55 THz and at 193.6 THz are not present since the signal degradation was too high, then the line cards were in out of service state and thus the pre-FEC BER was not available. For all distances, a good agreement can be found between measurements and OLE-based estimations with ± 0.75 dB accuracy. The oscillations in the generalized SNR values are mainly due to the ripple of the amplifier gain. We overcame this problem in the prediction feeding the fiber module with the actual power profile but for effective improvement of QoT estimation procedures, it will be important to automate this process as well as to have an

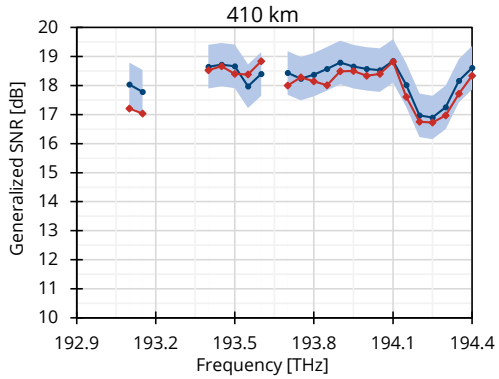

(a) SNR comparison after 410 km.

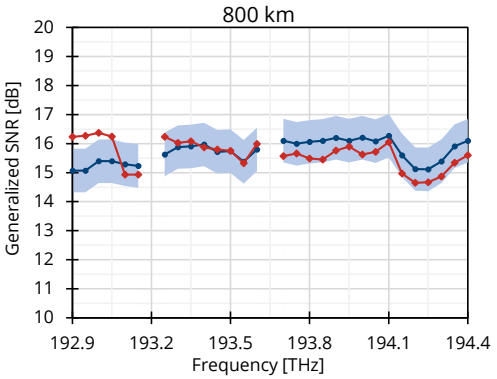

(b) SNR comparison after 800 km.

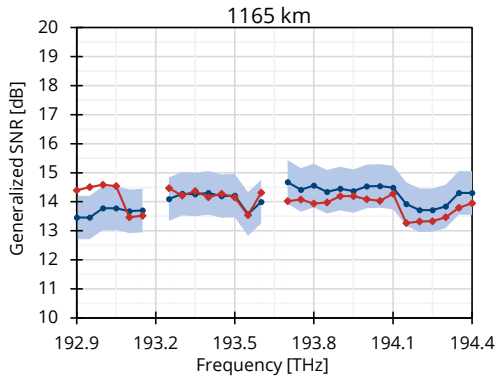

(c) SNR comparison after 1165 km.

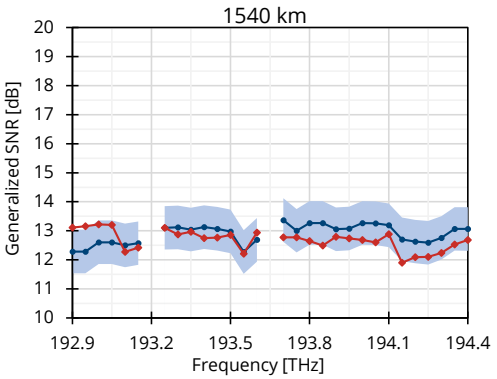

(d) SNR comparison after 1540 km.

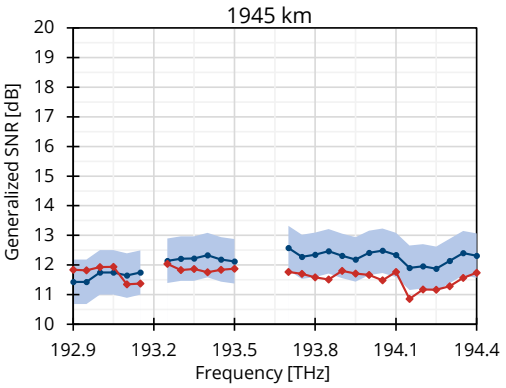

(e) SNR comparison after 1945 km.

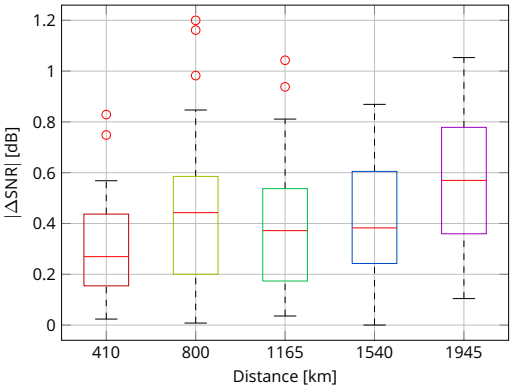

(f) Boxplot of SNR estimation error in absolute value vs distance.

Fig. 4.4 SNR values measured from commercial linecards (red diamond-marked curves) and estimated through the OLE software (blue circle-marked curves) at different distances. A ±0.75 dB area around OLE estimation is shown in light blue. The box plots for the absolute value of the SNR estimation error are also reported.

accurate characterization of the amplifiers' gain and noise figure frequency profiles. Channels at the edges of WSSs media channels and high symbol rate channels show larger estimation errors due to filtering effects that do not allow a reliable estimation of linear SNR with the previously described PSD-based procedure. Some of these points are represented by the outliers in the box plots of Fig. 4.4f. Furthermore, as the OLE version used for this validation campaign does not include Hybrid Raman amplification and Stimulated Raman Scattering modeling for both linear and nonlinear SNR estimation [121], some inconsistency across the estimations can be expected. Additionally, the OLS used in the testbed automatically applied channel tilting of each amplifier to compensate for Raman tilting during propagation. This effect is yet again not modeled in OLE, but it has been shown to be relevant for both linear and nonlinear SNR estimations as it can be predicted from the GGN model. These effects explain why the OLE estimations, for the majority of the channels, are not conservative with respect to SNR measurements as it is usually shown in literature and by simulations [86], [116]. Lastly, the current OLE version does not include filtering penalty estimation. Nevertheless, it is worth highlighting that the error distributions are consistent with OOPT-PSE goals with respect to estimation precision, even though there is much room for improvement for the adopted algorithms. The median of the absolute value of the SNR estimation error ΔSNR varies from 0.27 dB to 0.57 dB from 410 km to 1945 km. The mean interquartile range (IQR) across all distances is 0.36 dB. This growth in ΔSNR median vs distance is due to the many effects that OLE is currently neglecting, causing an accumulation of errors with increasing distance.

4.3 Conclusion

Developing and helping to validate the OLE within the PSE group of TIP represented a great opportunity for steering future research in an industrially relevant context both from a physical layer modeling standpoint and an information integration one. Industry requires more consistent and computationally efficient modeling across the full WDM comb for integrating models in orchestrator and vendor agnostic design tools. However, such a

requirement cannot be achieved without a consistent information gathering from devices that need to be designed keeping into account both ease of access and accuracy of the measurements. With respect to this, multi-vendor common APIs need to be developed, to make multi-vendor disaggregated networks a commercial reality.

Leveraging the TIP-PSE experience, we started, together with the Optical Networking Advanced Research (OpNeAR) lab in the University of Texas at Dallas, the integration of a QoT estimation module within a multilayer orchestrator called ProNET [175]. Among the goals of this integration, there is the demonstration of advanced proactive techniques for automated elastic circuit deployment, with real-time computation of optical feasibility exploiting the QoT estimation module. As these aspects represent active research topics, preliminary results are not included in this thesis as they will be fully developed in the near future.

Chapter 5

Conclusions and Future Work

In this thesis, physical layer awareness for the design and orchestration of optical networks has been discussed. Novel aspects in terms of nonlinear physical layer modeling and network design have been proposed.

5.1 Summary

This thesis began with a general introduction to optical communications and network, with a review of the main trends in optical communications. It was shown how the IP traffic increase and revenue compression in the Telecom industry are putting a lot of pressure on the optical community to develop novel solutions that must both increase total capacity while being cost effective. This requirement is pushing operators towards network disaggregation, where optical network infrastructure in built by mix and match different physical layer technology solutions from different vendors.

In such a novel context, every equipment and transmission technique at the physical layer impacts the overall network behavior. Hence, methods giving quantitative evaluations of individual merit of physical layer equipment at network level are a firm request during *network design* phases as well as during network lifetime, when it is essential for the *orchestration* of logical and transmission layers and for addressing selected upgrades to properly react to growth and modifications of traffic requests. Therefore

physical layer awareness in network design and operation is fundamental to fairly assess the potentialities, and exploit the capabilities of different physical layer technologies in modern flexible, transparent and reconfigurable optical networks.

Starting from these requirements, a review of propagation impairments in transparent optical networks were given, mainly focusing on nonlinear modeling. The well-known Gaussian Noise model was described, then a set of simulative and experimental studies for its generalization for C-band and beyond optical systems was presented. Specifically, the impact of polarization mode dispersion on nonlinear interference generation was studied, showing how the PMD impact is *negligible* for polarization multiplexed signals, thus making valid the usage of the well-known Manakov equation beyond its bandwidth of validity. Based on this result, the GN-model have been extended to take into account space and frequency amplitude variations, mainly due to Stimulated Raman Scattering, on NLI generation. The Generalized GN model has been derived, experimentally validated, and an example of application was given. Then, network-level power optimization strategies were discussed reviewing the LOGO approach for power optimization in optical networks.

Later in Ch. 3, a novel framework of analysis for optical networks leveraging detailed modeling of propagation impairments, have been proposed. The Statistical Network Assessment Process (SNAP) have been introduced, motivated by the need of having a *general* framework to assess the impact of different physical layer technologies on network performance, without relying on rigid and complex optimization approaches that are not well-suited for technology comparison. Several examples of applications of SNAP have been given, including bitrate flexible transceivers, amplifiers, ROADMs and flexible grid technology comparison. SNAP has been also used to highlight topological bottlenecks in progressively loaded network scenario, and its output adapted to derive possible solutions for such bottlenecks. The SNAP results proposed in this thesis are also covered in journal and conference peer-reviewed works, and at the time of writing, two different vendors of optical communications equipment demonstrated interest in SNAP as a framework to test their goodness of their technologies at a network level.

In the final chapter, the work performed within the Physical Simulation Environment (PSE) of the Telecom Infra Project consortium for the development of a vendor agnostic quality of transmission estimator have been described, and the related validation over multi-vendor commercial equipment in collaboration with Microsoft have been shown.

5.2 Next steps

There are several possible future evolutions for the topics tackled in this thesis. Starting from the GGN model, it will be interesting to derive closed-form formulae to make the model much more computationally efficient. A possible approach to make this feasible would be to consider closed form solutions for the SRS-induced tilt, as for example the one described in [176]. Starting from that, a natural step for evolving this would be the derivation of optimal power profile for SNR maximization across the full optical band, C+L systems.

With respect to SNAP, an interesting research opportunity is represented by the matching of SNAP obtained results with theoretical investigations of network blocking phenomena, especially under QoT constraints. Another interesting set of studies with respect to SNAP would be a simplified derivation of network bottlenecks, in order to steer the topological design without the need for SNAP-based traffic allocations, in a purely *offline* way.

Another relevant topic that could be of interest for future studies is related to the assessment of filtering penalties due to cascaded filtering for enhancement of QoT-E predictions, as well as SNAP based analyses.

Finally, the more interesting field of study is related to the extension of the OLE with more accurate modeling options such as the GGN-model, and the integration of it in network orchestrator. Such effort is ongoing, as a collaboration with the OpNear lab in UTD is currently active to achieve this goal. While the software integration is now getting finalized, we are working, as of today, towards the development of a real demonstration of a QoT aware orchestrator, showing how QoT awareness can bring advantage in network

flexibility with respect to failure and disaster recovery and automation of network operations.

References

[1] R. Valentini, "15 settembre 1977, Torino, prima stesura al mondo di una fibra ottica in esercizio. Un record detenuto da TIM.," 2017.

[2] S. Buzzelli, B. Catania, D. Gagliardi, and F. Tosco, "Optical fibre field experiments in Italy: COS 1 COS 2 and COS 3/FOSTER," in *Proc. Int. Conf. Commun.*, 1980, pp. 38–3.

[3] J. Hecht, *City of Light: The Story of Fiber Optics*, ser. Oxford University Press paperback. Oxford University Press, 2004.

[4] R. Mears, L. Reekie, I. Jauncey, and D. Payne, "Low-noise erbium-doped fibre amplifier operating at 1.54μm," *Electronics Letters*, vol. 23, no. 19, p. 1026, 1987. DOI: 10.1049/el:19870719.

[5] P. J. Winzer and D. T. Neilson, "From Scaling Disparities to Integrated Parallelism: A Decathlon for a Decade," *Journal of Lightwave Technology*, vol. 35, no. 5, pp. 1099–1115, Mar. 2017. DOI: 10.1109/JLT.2017.2662082.

[6] T. Economist, "The great telecoms crash," *The Economist*, Jul. 18, 2002.

[7] R. W. Tkach, "Scaling optical communications for the next decade and beyond," *Bell Labs Technical Journal*, vol. 14, no. 4, pp. 3–9, Feb. 23, 2010. DOI: 10.1002/bltj.20400.

[8] V. Vusirikala, B. Koley, T. Hofmeister, V. Dangui, V. Kamalov, and X. Zhao, "Scalable and Flexible Transport Networks for Inter-Datacenter Connectivity," in *2015 Optical Fiber Communication Conference*, OSA, 2015, Tu3H.1. DOI: 10.1364/OFC.2015.Tu3H.1.

[9] S. Hardy. (Mar. 17, 2016). Nokia upgrades 1830 PSS packet-optical transport family with new coherent chipsets, improved multi-rate performance, [Online]. Available: http://bit.ly/2zLYTv0 (visited on 10/23/2017).

[10] J. Homa and K. Bala, "ROADM Architectures and Their Enabling WSS Technology," *IEEE Communications Magazine*, vol. 46, no. 7, pp. 150–154, Jul. 2008. DOI: 10.1109/MCOM.2008.4557058.

[11] S. L. Woodward, M. D. Feuer, and P. Palacharla, "ROADM-Node Architectures for Reconfigurable Photonic Networks," in *Optical Fiber Telecommunications*, Elsevier, 2013, pp. 683–707. DOI: 10.1016/B978-0-12-396960-6.00015-8.

[12] N. Antoniades, G. Ellinas, J. Homa, and K. Bala, "ROADM Architectures and WSS Implementation Technologies," in *Convergence of Mobile and Stationary Next-Generation Networks*, Hoboken, NJ, USA: John Wiley & Sons, Inc., Sep. 21, 2010, pp. 643–674. DOI: 10.1002/9780470630976.ch20.

[13] A. A. M. Saleh and J. M. Simmons, "All-Optical Networking—Evolution, Benefits, Challenges, and Future Vision," *Proceedings of the IEEE*, vol. 100, no. 5, pp. 1105–1117, May 2012. DOI: 10.1109/JPROC.2011.2182589.

[14] J. Strand and A. Chiu, "Realizing the advantages of optical reconfigurability and restoration with integrated optical cross-connects," *Journal of Lightwave Technology*, vol. 21, no. 11, pp. 2871–2882, Nov. 2003. DOI: 10.1109/JLT.2003.819539.

[15] Cisco, *Cisco Visual Networking Index: Forecast and Methodology, 2016–2021*, Sep. 15, 2017.

[16] E. I. E. Association, "European IXP Report 2016," 2017.

[17] A. I. Exchange. (2017). Historical Traffic Data, [Online]. Available: https://ams-ix.net/technical/statistics/historical-traffic-data.

[18] M. Z. Shafiq, L. Ji, A. X. Liu, J. Pang, and J. Wang, "A first look at cellular machine-to-machine traffic: Large scale measurement and characterization," in *IEEE/ACM Transactions on Networking*, ACM Press, 2012, p. 65. DOI: 10.1145/2254756.2254767.

[19] S. I. Exchange. (2017). Traffic Graphs, [Online]. Available: https://www.seattleix.net/statistics/.

[20] PeeringDB. (2017). PeeringDB, [Online]. Available: https://www.peeringdb.com/.

[21] W. B. Norton, *The Internet Peering Playbook: Connecting to the Core of the Internet*. Palo Alto, Ca.: DrPeering Press, 2011, OCLC: 789668916.

[22] Google. (2017). Google Edge Network, [Online]. Available: https://peering.google.com.

[23] Facebook. (2017). Facebook Peering, [Online]. Available: https://www.facebook.com/peering/.

[24] Netflix. (2017). Netflix Open Connect, [Online]. Available: https://openconnect.netflix.com.

[25] B. Rogan, "Providing Self-Service to Google's Peers," presented at the NANOG49, San Francisco, Jun. 3, 2015.

[26] R.-J. Essiambre, G. Kramer, P. J. Winzer, G. J. Foschini, and B. Goebel, "Capacity Limits of Optical Fiber Networks," *Journal of Lightwave Technology*, vol. 28, no. 4, pp. 662–701, Feb. 2010. DOI: 10.1109/JLT.2009.2039464.

[27] C. Wilson. (Sep. 1, 2017). Nolle: In 2017, Cost Per Bit Exceeds Revenues, [Online]. Available: http://www.lightreading.com/business-employment/business-transformation/nolle-in-2017-cost-per-bit-exceeds-revenues/d/d-id/729446.

[28] J. S. Marcus, "The Economic Impact of Internet Traffic Growth on Network Operators," *SSRN Electronic Journal*, 2014. DOI: 10.2139/ssrn.2531782.

[29] OVUM, "Telecoms, Media & Entertainment Outlook 2015," 2015.

[30] G. Wellbrock and T. J. Xia, "How will optical transport deal with future network traffic growth?" In *2014 The European Conference on Optical Communication (ECOC)*, IEEE, Sep. 2014, pp. 1–3. DOI: 10.1109/ECOC.2014.6964248.

[31] D.-S. Ly-Gagnon, S. Tsukamoto, K. Katoh, and K. Kikuchi, "Coherent detection of optical quadrature phase-shift keying signals with carrier phase estimation," *Journal of Lightwave Technology*, vol. 24, no. 1, pp. 12–21, Jan. 2006. DOI: 10.1109/JLT.2005.860477.

[32] M. Taylor, "Coherent Detection Method Using DSP for Demodulation of Signal and Subsequent Equalization of Propagation Impairments," *IEEE Photonics Technology Letters*, vol. 16, no. 2, pp. 674–676, Feb. 2004. DOI: 10.1109/LPT.2003.823106.

[33] J. M. Dugan, A. J. Price, M. Ramadan, D. L. Wolf, E. F. Murphy, A. J. Antos, D. K. Smith, and D. W. Hall, "All-Optical, Fiber-Based 1550 nm Dispersion Compensation in a 10 Gbit/s, 150 km Transmission Experiment over 1310 nm Optimized Fiber," in *Optical Fiber Communication Conference*, OSA, 1992, PD14. DOI: 10.1364/OFC.1992.PD14.

[34] M. Hayee and A. Willner, "NRZ versus RZ in 10-40-Gb/s dispersion-managed WDM transmission systems," *IEEE Photonics Technology Letters*, vol. 11, no. 8, pp. 991–993, Aug. 1999. DOI: 10.1109/68.775323.

[35] V. Curri, M. Cantono, and R. Gaudino, "Elastic All-Optical Networks: A New Paradigm Enabled by the Physical Layer. How to Optimize Network Performances?" *Journal of Lightwave Technology*, vol. 35, no. 6, pp. 1211–1221, Mar. 15, 2017. DOI: 10.1109/JLT.2017.2657231.

[36] H. Sun, K.-T. Wu, and K. Roberts, "Real-time measurements of a 40 Gb/s coherent system," *Optics Express*, vol. 16, no. 2, p. 873, 2008. DOI: 10.1364/OE.16.000873.

[37] S. J. Savory, G. Gavioli, R. I. Killey, and P. Bayvel, "Electronic compensation of chromatic dispersion using a digital coherent receiver," *Optics Express*, vol. 15, no. 5, p. 2120, 2007. DOI: 10.1364/OE.15.002120.

[38] H. Bulow, F. Buchali, and A. Klekamp, "Electronic Dispersion Compensation," *Journal of Lightwave Technology*, vol. 26, no. 1, pp. 158–167, 2008. DOI: 10.1109/JLT.2007.913066.

[39] S. J. Savory, "Digital Coherent Optical Receivers: Algorithms and Subsystems," *IEEE Journal of Selected Topics in Quantum Electronics*, vol. 16, no. 5, pp. 1164–1179, Sep. 2010. DOI: 10.1109/JSTQE.2010.2044751.

[40] X. Zhou, L. E. Nelson, and P. Magill, "Rate-adaptable optics for next generation long-haul transport networks," *IEEE Communications Magazine*, vol. 51, no. 3, pp. 41–49, Mar. 2013. DOI: 10.1109/MCOM.2013.6476864.

[41] F. P. Guiomar, R. Li, C. R. S. Fludger, A. Carena, and V. Curri, "Hybrid Modulation Formats Enabling Elastic Fixed-Grid Optical Networks," *Journal of Optical Communications and Networking*, vol. 8, no. 7, A92, Jul. 1, 2016. DOI: 10.1364/JOCN.8.000A92.

[42] V. Curri, P. Poggiolini, A. Carena, and F. Forghieri, "Dispersion Compensation and Mitigation of Nonlinear Effects in 111-Gb/s WDM Coherent PM-QPSK Systems," *IEEE Photonics Technology Letters*, vol. 20, no. 17, pp. 1473–1475, Sep. 2008. DOI: 10.1109/LPT.2008.927906.

[43] V. Kamalov, V. Dangui, T. Hofmeister, B. Koley, C. Mitchell, M. Newland, J. O'Shea, C. Tomblin, V. Vusirikala, and X. Zhao, "Lessons Learned from Open Line System Deployments," in *2017 Optical Fiber Communication Conference*, OSA, 2017, M2E.2. DOI: 10.1364/OFC.2017.M2E.2.

[44] Gazzetabyte. (Dec. 4, 2016). The white box concept gets embraced at the optical layer, [Online]. Available: http://www.gazettabyte.com/home/2016/4/12/the-white-box-concept-gets-embraced-at-the-optical-layer.html (visited on 11/07/2017).

[45] OpenConfig. (). OpenConfig, [Online]. Available: http://openconfig.net/.

[46] TIP. (). The Telecom Infra Project (TIP), [Online]. Available: https://telecominfraproject.com.

[47] O. ROADM. (). Open ROADM MSA, [Online]. Available: http://www.openroadm.org.

[48] M. Jinno, H. Takara, B. Kozicki, Y. Tsukishima, T. Yoshimatsu, T. Kobayashi, Y. Miyamoto, K. Yonenaga, A. Takada, O. Ishida, and S. Matsuoka, "Demonstration of novel spectrum-efficient elastic optical path network with per-channel variable capacity of 40 Gb/s to over 400 Gb/s," in *2008 34th European Conference on Optical Communication*, IEEE, 2008, pp. 1–2. DOI: 10.1109/ECOC.2008.4729581.

[49] I. Tomkos, S. Azodolmolky, J. Sole-Pareta, D. Careglio, and E. Palkopoulou, "A tutorial on the flexible optical networking paradigm: State of the art, trends, and research challenges," *Proceedings of the IEEE*, vol. 102, no. 9, pp. 1317–1337, Sep. 2014. DOI: 10.1109/JPROC.2014.2324652.

[50] R. Munoz, R. Vilalta, R. Casellas, R. Martinez, F. Francois, M. Channegowda, A. Hammad, S. Peng, R. Nejabati, D. Simeonidou, N. Yoshikane, T. Tsuritani, V. Lopez, and A. Autenrieth, "Transport Network Orchestration for End-to-End Multilayer Provisioning Across Heterogeneous SDN/OpenFlow and GMPLS/PCE Control Domains," *Journal of Lightwave Technology*, vol. 33, no. 8, pp. 1540–1548, Apr. 15, 2015. DOI: 10.1109/JLT.2015.2393634.

[51] G. P. Agrawal, *Nonlinear Fiber Optics*. Amsterdam: Academic Press, 2013, OCLC: 820850077.

[52] D. Marcuse, C. Manyuk, and P. Wai, "Application of the Manakov-PMD equation to studies of signal propagation in optical fibers with randomly varying birefringence," *Journal of Lightwave Technology*, vol. 15, no. 9, pp. 1735–1746, Sept./1997. DOI: 10.1109/50.622902.

[53] J. P. Gordon and H. Kogelnik, "PMD fundamentals: Polarization mode dispersion in optical fibers," *Proceedings of the National Academy of Sciences*, vol. 97, no. 9, pp. 4541–4550, Apr. 25, 2000. DOI: 10.1073/pnas.97.9.4541.

[54] C. R. Menyuk and A. Galtarossa, *Polarization Mode Dispersion*. New York, N.Y.: Springer, 2005, OCLC: 64583024.

[55] A. Mecozzi and M. Shtaif, "The statistics of polarization-dependent loss in optical communication systems," *IEEE Photonics Technology Letters*, vol. 14, no. 3, pp. 313–315, Mar. 2002. DOI: 10.1109/68.986797.

[56] Y.-T. Hsueh, A. Stark, C. Liu, T. Detwiler, S. Tibuleac, M. Filer, G.-K. Chang, and S. E. Ralph, "Passband Narrowing and Crosstalk Impairments in ROADM-Enabled 100G DWDM Networks," *Journal of Lightwave Technology*, vol. 30, no. 24, pp. 3980–3986, Dec. 2012. DOI: 10.1109/JLT.2012.2208262.

[57] D. Rafique and A. D. Ellis, "Nonlinear and ROADM induced penalties in 28 Gbaud dynamic optical mesh networks employing electronic signal processing," *Optics Express*, vol. 19, no. 18, p. 16 739, Aug. 28, 2011. DOI: 10.1364/OE.19.016739.

[58] T. Rahman, A. Napoli, D. Rafique, B. Spinnler, M. Kuschnerov, I. Lobato, B. Clouet, M. Bohn, C. Okonkwo, and H. de Waardt, "On the Mitigation of Optical Filtering Penalties Originating From ROADM Cascade," *IEEE Photonics Technology Letters*, vol. 26, no. 2, pp. 154–157, Jan. 2014. DOI: 10.1109/LPT.2013.2290745.

[59] C. V. Raman, "A new radiation," 1928.

[60] R. H. Stolen and E. P. Ippen, "Raman gain in glass optical waveguides," *Applied Physics Letters*, vol. 22, no. 6, pp. 276–278, Mar. 15, 1973. DOI: 10.1063/1.1654637.

[61] R. G. Smith, "Optical Power Handling Capacity of Low Loss Optical Fibers as Determined by Stimulated Raman and Brillouin Scattering," *Applied Optics*, vol. 11, no. 11, p. 2489, Nov. 1, 1972. DOI: 10.1364/AO.11.002489.

[62] M. Cantono, V. Curri, A. Mecozzi, and R. Gaudino, "Polarization-Related Statistics of Raman Crosstalk in Single-Mode Optical Fibers," *Journal of Lightwave Technology*, vol. 34, no. 4, pp. 1191–1205, Feb. 15, 2016. DOI: 10.1109/JLT.2015.2506481.

[63] D. Semrau, R. Killey, and P. Bayvel, "Achievable rate degradation of ultra-wideband coherent fiber communication systems due to stimulated Raman scattering," *Optics Express*, vol. 25, no. 12, p. 13 024, Jun. 12, 2017. DOI: 10.1364/OE.25.013024.

[64] S. D. Personick, "Receiver Design for Digital Fiber Optic Communication Systems, I," *Bell System Technical Journal*, vol. 52, no. 6, pp. 843–874, Jul. 8, 1973. DOI: 10.1002/j.1538-7305.1973.tb01993.x.

[65] G. P. Agrawal, *Fiber-Optic Communication Systems*, 4. ed, ser. Wiley series in microwave and optical engineering. Hoboken, NJ: Wiley, 2010, 603 pp., OCLC: 705930760.

[66] W. Freude, R. Schmogrow, B. Nebendahl, M. Winter, A. Josten, D. Hillerkuss, S. Koenig, J. Meyer, M. Dreschmann, M. Huebner, C. Koos, J. Becker, and J. Leuthold, "Quality metrics for optical signals: Eye diagram, Q-factor, OSNR, EVM and BER," in *2012 14th International Conference on Transparent Optical Networks (ICTON)*, IEEE, Jul. 2012, pp. 1–4. DOI: 10.1109/ICTON.2012.6254380.

[67] B. Ramamurthy, D. Datta, H. Feng, J. Heritage, and B. Mukherjee, "Impact of transmission impairments on the teletraffic performance of wavelength-routed optical networks," *Journal of Lightwave Technology*, vol. 17, no. 10, pp. 1713–1723, Oct./1999. DOI: 10.1109/50.793740.

[68] S. Azodolmolky, M. Klinkowski, E. Marin, D. Careglio, J. Pareta, and I. Tomkos, "A survey on physical layer impairments aware routing and wavelength assignment algorithms in optical networks," *Computer Networks*, vol. 53, no. 7, pp. 926–944, May 2009. DOI: 10.1016/j.comnet.2008.11.014.

[69] R. Cardillo, V. Curri, and M. Mellia, "Considering transmission impairments in configuring wavelength routed optical networks," in *2006 Optical Fiber Communication Conference and the National Fiber Optic Engineers Conference*, IEEE, 2006, 3 pp. DOI: 10.1109/OFC.2006.215976.

[70] S. Benedetto and E. Biglieri, *Principles of Digital Transmission: With Wireless Applications*, ser. Information technology. New York: Kluwer, 1999, 855 pp., OCLC: 246138833.

[71] A. Carena, V. Curri, G. Bosco, P. Poggiolini, and F. Forghieri, "Modeling of the Impact of Nonlinear Propagation Effects in Uncompensated Optical Coherent Transmission Links," *Journal of Lightwave Technology*, vol. 30, no. 10, pp. 1524–1539, May 2012. DOI: 10.1109/JLT.2012.2189198.

[72] E. Desurvire, "Analysis of noise figure spectral distribution in erbium doped fiber amplifiers pumped near 980 and 1480 nm," *Applied Optics*, vol. 29, no. 21, p. 3118, Jul. 20, 1990. DOI: 10.1364/AO.29.003118.

[73] M. Islam, "Raman amplifiers for telecommunications," *IEEE Journal of Selected Topics in Quantum Electronics*, vol. 8, no. 3, pp. 548–559, May 2002. DOI: 10.1109/JSTQE.2002.1016358.

[74] V. Curri and A. Carena, "Merit of Raman Pumping in Uniform and Uncompensated Links Supporting NyWDM Transmission," *Journal of Lightwave Technology*, vol. 34, no. 2, pp. 554–565, Jan. 15, 2016. DOI: 10.1109/JLT.2015.2477599.

[75] J. Pan, C. Pulikkaseril, L. Stewart, and S. Tibuleac, "Comparison of ROADM filter shape models for accurate transmission penalty assessment," in *2016 IEEE Photonics Conference (IPC)*, IEEE, Oct. 2016, pp. 550–551. DOI: 10.1109/IPCon.2016.7831225.

[76] T. Foggi, G. Colavolpe, A. Bononi, and P. Serena, "Overcoming filtering penalties in flexi-grid long-haul optical systems," in *2015 IEEE International Conference on Communications (ICC)*, IEEE, Jun. 2015, pp. 5168–5173. DOI: 10.1109/ICC.2015.7249144.

[77] T. Takagi, H. Hasegawa, K. Sato, T. Tanaka, B. Kozicki, Y. Sone, and M. Jinno, "Algorithms for maximizing spectrum efficiency in elastic optical path networks that adopt distance adaptive modulation," in *36th European Conference and Exhibition on Optical Communication*, IEEE, Sep. 2010, pp. 1–3. DOI: 10.1109/ECOC.2010.5621146.

[78] F. Vacondio, O. Rival, C. Simonneau, E. Grellier, A. Bononi, L. Lorcy, J.-C. Antona, and S. Bigo, "On nonlinear distortions of highly dispersive optical coherent systems," *Optics Express*, vol. 20, no. 2, p. 1022, Jan. 16, 2012. DOI: 10.1364/OE.20.001022.

[79] A. Bononi, P. Serena, N. Rossi, E. Grellier, and F. Vacondio, "Modeling nonlinearity in coherent transmissions with dominant intrachannel-four-wave-mixing," *Optics Express*, vol. 20, no. 7, p. 7777, Mar. 26, 2012. DOI: 10.1364/OE.20.007777.

[80] A. Mecozzi and R.-J. Essiambre, "Nonlinear Shannon Limit in Pseudolinear Coherent Systems," *Journal of Lightwave Technology*, vol. 30, no. 12, pp. 2011–2024, Jun. 2012. DOI: 10.1109/JLT.2012.2190582.

[81] M. Secondini and E. Forestieri, "Analytical Fiber-Optic Channel Model in the Presence of Cross-Phase Modulation," *IEEE Photonics Technology Letters*, vol. 24, no. 22, pp. 2016–2019, Nov. 2012. DOI: 10.1109/LPT.2012.2217952.

[82] P. Johannisson and M. Karlsson, "Perturbation Analysis of Nonlinear Propagation in a Strongly Dispersive Optical Communication System," *Journal of Lightwave Technology*, vol. 31, no. 8, pp. 1273–1282, Apr. 2013. DOI: 10.1109/JLT.2013.2246543.

[83] R. Dar, M. Feder, A. Mecozzi, and M. Shtaif, "Properties of nonlinear noise in long, dispersion-uncompensated fiber links," *Optics Express*, vol. 21, no. 22, p. 25 685, Nov. 4, 2013. DOI: 10.1364/OE.21.025685.

[84] P. Serena and A. Bononi, "An Alternative Approach to the Gaussian Noise Model and its System Implications," *Journal of Lightwave Technology*, vol. 31, no. 22, pp. 3489–3499, Nov. 2013. DOI: 10.1109/JLT.2013.2284499.

[85] M. Secondini, E. Forestieri, and G. Prati, "Achievable Information Rate in Nonlinear WDM Fiber-Optic Systems With Arbitrary Modulation Formats and Dispersion Maps," *Journal of Lightwave Technology*, vol. 31, no. 23, pp. 3839–3852, Dec. 2013. DOI: 10.1109/JLT.2013.2288677.

[86] P. Poggiolini, G. Bosco, A. Carena, V. Curri, Y. Jiang, and F. Forghieri, "The GN-Model of Fiber Non-Linear Propagation and its Applications," *Journal of Lightwave Technology*, vol. 32, no. 4, pp. 694–721, Feb. 2014. DOI: 10.1109/JLT.2013.2295208.

[87] R. Dar, M. Feder, A. Mecozzi, and M. Shtaif, "Accumulation of nonlinear interference noise in fiber-optic systems," *Optics Express*, vol. 22, no. 12, p. 14 199, Jun. 16, 2014. DOI: 10.1364/OE.22.014199.

[88] P. Poggiolini, A. Carena, V. Curri, G. Bosco, and F. Forghieri, "Analytical Modeling of Nonlinear Propagation in Uncompensated Optical Transmission Links," *IEEE Photonics Technology Letters*, vol. 23, no. 11, pp. 742–744, Jun. 2011. DOI: 10.1109/LPT.2011.2131125.

[89] S. J. Savory, "Approximations for the Nonlinear Self-Channel Interference of Channels With Rectangular Spectra," *IEEE Photonics Technology Letters*, vol. 25, no. 10, pp. 961–964, May 2013. DOI: 10.1109/LPT.2013.2255869.

[90] A. Bononi, O. Beucher, and P. Serena, "Single- and cross-channel nonlinear interference in the Gaussian Noise model with rectangular spectra," *Optics Express*, vol. 21, no. 26, p. 32 254, Dec. 30, 2013. DOI: 10.1364/OE.21.032254.

[91] P. Johannisson and E. Agrell, "Modeling of Nonlinear Signal Distortion in Fiber-Optic Networks," *Journal of Lightwave Technology*, vol. 32, no. 23, pp. 4544–4552, Dec. 1, 2014. DOI: 10.1109/JLT.2014.2361357.

[92] P. Poggiolini and Y. Jiang, "Recent Advances in the Modeling of the Impact of Nonlinear Fiber Propagation Effects on Uncompensated Coherent Transmission Systems," *Journal of Lightwave Technology*, vol. 35, no. 3, pp. 458–480, Feb. 1, 2017. DOI: 10.1109/JLT.2016.2613893.

[93] A. Splett, C. Kurtzke, and K. Petermann, "Ultimate Transmission Capacity of Amplified Optical Fiber Communication Systems taking into Account Fiber Nonlinearities," in *1993 European Conference and Exhibition on Optical Communications*, vol. 2, Montreaux, Switzerland, Sep. 1993, pp. 41–44.

[94] Jau Tang, "The channel capacity of a multispan DWDM system employing dispersive nonlinear optical fibers and an ideal coherent optical receiver," *Journal of Lightwave Technology*, vol. 20, no. 7, pp. 1095–1101, Jul. 2002. DOI: 10.1109/JLT.2002.800344.

[95] H. Louchet, A. Hodzic, and K. Petermann, "Analytical model for the performance evaluation of DWDM transmission systems," *IEEE Photonics Technology Letters*, vol. 15, no. 9, pp. 1219–1221, Sep. 2003. DOI: 10.1109/LPT.2003.816133.

[96] X. Chen and W. Shieh, "Closed-form expressions for nonlinear transmission performance of densely spaced coherent optical OFDM systems," *Optics Express*, vol. 18, no. 18, p. 19 039, Aug. 30, 2010. DOI: 10.1364/OE.18.019039.

[97] P. Poggiolini, G. Bosco, A. Carena, V. Curri, Y. Jiang, and F. Forghieri, "A Detailed Analytical Derivation of the GN Model of Non-Linear Interference in Coherent Optical Transmission Systems," Sep. 3, 2012. arXiv: 1209.0394 [physics].

[98] K. Inoue and H. Toba, "Fiber four-wave mixing in multi-amplifier systems with nonuniform chromatic dispersion," *Journal of Lightwave Technology*, vol. 13, no. 1, pp. 88–93, Jan./1995. DOI: 10.1109/50.350641.

[99] A. Carena, G. Bosco, V. Curri, Y. Jiang, P. Poggiolini, and F. Forghieri, "EGN model of non-linear fiber propagation," *Optics Express*, vol. 22, no. 13, p. 16 335, Jun. 30, 2014. DOI: 10.1364/OE.22.016335.

[100] L. Galdino, G. Liga, G. Saavedra, D. Ives, R. Maher, A. Alvarado, S. Savory, R. Killey, and P. Bayvel, "Experimental Demonstration of Modulation-Dependent Nonlinear Interference in Optical Fibre Communication," in *ECOC 2016; 42nd European Conference on Optical Communication*, Sep. 2016, pp. 1–3.

[101] W. Zeiler, F. Di Pasquale, P. Bayvel, and J. Midwinter, "Modeling of four-wave mixing and gain peaking in amplified WDM optical communication systems and networks," *Journal of Lightwave Technology*, vol. 14, no. 9, pp. 1933–1942, Sep. 1996. DOI: 10.1109/50.536960.

[102] P. Poggiolini, G. Bosco, A. Carena, V. Curri, Y. Jiang, and F. Forghieri, "A Simple and Effective Closed-Form GN Model Correction Formula Accounting for Signal Non-Gaussian Distribution," *Journal of Lightwave Technology*, vol. 33, no. 2, pp. 459–473, Jan. 15, 2015. DOI: 10.1109/JLT.2014.2387891.

[103] A. Carena, G. Bosco, V. Curri, P. Poggiolini, M. T. Taiba, and F. Forghieri, "Statistical characterization of PM-QPSK signals after propagation in uncompensated fiber links," in *36th European Conference and Exhibition on Optical Communication*, IEEE, Sep. 2010, pp. 1–3. DOI: 10.1109/ECOC.2010.5621509.

[104] G. Bosco, A. Carena, R. Cigliutti, V. Curri, P. Poggiolini, and F. Forghieri, "Performance prediction for WDM PM-QPSK transmission over uncompensated links," in *2011 Optical Fiber Communication Conference and Exposition and the National Fiber Optic Engineers Conference*, Mar. 2011, pp. 1–3.

[105] E. Grellier and A. Bononi, "Quality parameter for coherent transmissions with Gaussian-distributed nonlinear noise," *Optics Express*, vol. 19, no. 13, p. 12 781, Jun. 20, 2011. DOI: 10.1364/OE.19.012781.

[106] P. Poggiolini, G. Bosco, A. Carena, R. Cigliutti, V. Curri, F. Forghieri, R. Pastorelli, and S. Piciaccia, "The LOGON Strategy for Low-Complexity Control Plane Implementation in New-Generation Flexible Networks," in *2013 Optical Fiber Communication Conference*, OSA, 2013, OW1H.3. DOI: 10.1364/OFC.2013.OW1H.3.

[107] V. Curri, A. Carena, A. Arduino, G. Bosco, P. Poggiolini, A. Nespola, and F. Forghieri, "Design Strategies and Merit of System Parameters for Uniform Uncompensated Links Supporting Nyquist-WDM Transmission," *Journal of Lightwave Technology*, vol. 33, no. 18, pp. 3921–3932, Sep. 15, 2015. DOI: 10.1109/JLT.2015.2447151.

[108] A. Bononi, N. Rossi, and P. Serena, "On the nonlinear threshold versus distance in long-haul highly-dispersive coherent systems," *Optics Express*, vol. 20, no. 26, B204, Dec. 10, 2012. DOI: 10.1364/OE.20.00B204.

[109] R. Pastorelli, G. Bosco, S. Piciaccia, and F. Forghieri, "Network Planning Strategies for Next-Generation Flexible Optical Networks [Invited]," *Journal of Optical Communications and Networking*, vol. 7, no. 3, A511, Mar. 1, 2015. DOI: 10.1364/JOCN.7.00A511.

[110] S. Piciaccia, R. Pastorelli, E. Griseri, and F. Forghieri, "Analytical extension of LOGO approach for commercial optical networks and experimental validation," in *2015 Fotonica AEIT Italian Conference on Photonics Technologies*, Institution of Engineering and Technology, 2015, pp. 4 .–4 . DOI: 10.1049/cp.2015.0105.

[111] C. J. McKinstrie, H. Kogelnik, R. M. Jopson, S. Radic, and A. V. Kanaev, "Four-wave mixing in fibers with random birefringence," *Optics Express*, vol. 12, no. 10, p. 2033, 2004. DOI: 10.1364/OPEX.12.002033.

[112] A. Carena, V. Curri, R. Gaudino, P. Poggiolini, and S. Benedetto, "On the joint effects of fiber parametric gain and birefringence and their influence on ASE noise," *Journal of Lightwave Technology*, vol. 16, no. 7, pp. 1149–1157, Jul. 1998. DOI: 10.1109/50.701393.

[113] D. J. Elson, G. Saavedra, K. Shi, D. Semrau, L. Galdino, R. Killey, B. C. Thomsen, and P. Bayvel, "Investigation of bandwidth loading in optical fibre transmission using amplified spontaneous emission noise," *Optics Express*, vol. 25, no. 16, p. 19 529, Aug. 7, 2017. DOI: 10.1364/OE.25.019529.

[114] G. Saavedra, M. Tan, D. J. Elson, L. Galdino, D. Semrau, M. A. Iqbal, I. Phillips, P. Harper, N. MacSuibhne, A. Ellis, D. Lavery, B. C. Thomsen, R. Killey, and P. Bayvel, "Experimental Investigation of Nonlinear Signal Distortions in Ultra-Wideband Transmission Systems," in *2017 Optical Fiber Communication Conference*, OSA, 2017, W1G.1. DOI: 10.1364/OFC.2017.W1G.1.

[115] P. Serena, N. Rossi, O. Bertran-Pardo, J. Renaudier, A. Vannucci, and A. Bononi, "Intra- versus inter-channel pmd in linearly compensated coherent pdm-psk nonlinear transmissions," *Journal of Lightwave Technology*, vol. 29, no. 11, pp. 1691–1700, Jun. 2011. DOI: 10.1109/JLT.2011.2144570.

[116] D. Pilori, M. Cantono, A. Carena, and V. Curri, "FFSS: The fast fiber simulator software," in *2017 19th International Conference on Transparent Optical Networks (ICTON)*, IEEE, Jul. 2017, pp. 1–4. DOI: 10.1109/ICTON.2017.8025002.

[117] P. Wai and C. Menyak, "Polarization mode dispersion, decorrelation, and diffusion in optical fibers with randomly varying birefringence," *Journal of Lightwave Technology*, vol. 14, no. 2, pp. 148–157, Feb./1996. DOI: 10.1109/50.482256.

[118] M. Eberhard and C. Braimiotis, "Numerical Implementation of the Coarse-Step Method with a Varying Differential-Group Delay," in *Optical Networks and Technologies*, K.-I. Kitayama, F. Masetti-Placci, and G. Prati, Eds., vol. 164, Boston: Kluwer Academic Publishers, 2005, pp. 530–534. DOI: 10.1007/0-387-23178-1_68.

[119] O. Sinkin, R. Holzlohner, J. Zweck, and C. Menyuk, "Optimization of the split-step fourier method in modeling optical-fiber communications systems," *Journal of Lightwave Technology*, vol. 21, no. 1, pp. 61–68, Jan. 2003. DOI: 10.1109/JLT.2003.808628.

[120] W. A. Gardner, A. Napolitano, and L. Paura, "Cyclostationarity: Half a century of research," *Signal Processing*, vol. 86, no. 4, pp. 639–697, Apr. 2006. DOI: 10.1016/j.sigpro.2005.06.016.

[121] M. Cantono, D. Pilori, A. Ferrari, and V. Curri, "Introducing the Generalized GN-model for Nonlinear Interference Generation including space/frequency variations of loss/gain," *arXiv preprint arXiv:1710.02225*, 2017.

[122] D. Semrau and P. Bayvel, "The Gaussian Noise Model in the Presence of Inter-channel Stimulated Raman Scattering," *arXiv preprint arXiv:1801.02460*, 2017.

[123] I. Roberts, J. M. Kahn, J. Harley, and D. W. Boertjes, "Channel Power Optimization of WDM Systems Following Gaussian Noise Nonlinearity Model in Presence of Stimulated Raman Scattering," *Journal of Lightwave Technology*, vol. 35, no. 23, pp. 5237–5249, Dec. 1, 2017. DOI: 10.1109/JLT.2017.2771719.

[124] C. Fludger, V. Handerek, and R. Mears, "Pump to signal RIN transfer in Raman fibre amplifiers," *Electronics Letters*, vol. 37, no. 1, p. 15, 2001. DOI: 10.1049/el:20010027.

[125] M. Cantono, V. Curri, and R. Gaudino, "Raman Crosstalk Suppression in NG-PON2 Using Optimized Spectral Shaping," *Journal of Lightwave Technology*, vol. 33, no. 24, pp. 5284–5292, Dec. 15, 2015. DOI: 10.1109/JLT.2015.2501058.

[126] R. Aparicio-Pardo, P. Pavon-Marino, and B. Mukherjee, "Robust upgrade in optical networks under traffic uncertainty," in *2012 16th International Conference on Optical Network Design and Modelling (ONDM)*, IEEE, Apr. 2012, pp. 1–6. DOI: 10.1109/ONDM.2012.6210204.

[127] D. Amar, E. Le Rouzic, N. Brochier, E. Bonetto, and C. Lepers, "Traffic forecast impact on spectrum fragmentation in gridless optical networks," in *2014 The European Conference on Optical Communication (ECOC)*, IEEE, Sep. 2014, pp. 1–3. DOI: 10.1109/ECOC.2014.6963877.

[128] P. Soumplis, K. Christodoulopoulos, M. Quagliotti, A. Pagano, and E. Varvarigos, "Network Planning With Actual Margins," *Journal of Lightwave Technology*, vol. 35, no. 23, pp. 5105–5120, Dec. 1, 2017. DOI: 10.1109/JLT.2017.2743461.

[129] A. Bononi, P. Serena, G. Picchi, and A. Morea, "Load-aware transparent reach maximization in flexible optical networks," IEEE, Jun. 2014, pp. 165–172. DOI: 10.1109/NOC.2014.6996847.

[130] J. Pan, p. isautier, M. Filer, S. Tibuleac, and S. Ralph, "Addition of In-band Crosstalk to the Gaussian Noise Model," in *2015 Optical Fiber Communication Conference*, OSA, 2015, Th2A.22. DOI: 10.1364/OFC.2015.Th2A.22.

[131] M. Cantono, R. Gaudino, and V. Curri, "Potentialities and Criticalities of Flexible-Rate Transponders in DWDM Networks: A Statistical Approach," *Journal of Optical Communications and Networking*, vol. 8, no. 7, A76, Jul. 1, 2016. DOI: 10.1364/JOCN.8.000A76.

[132] D. J. Ives, P. Bayvel, and S. J. Savory, "Adapting Transmitter Power and Modulation Format to Improve Optical Network Performance Utilizing the Gaussian Noise Model of Nonlinear Impairments," *Journal of Lightwave Technology*, vol. 32, no. 21, pp. 4087–4096, Nov. 1, 2014. DOI: 10.1109/JLT.2014.2346582.

[133] L. Yan, E. Agrell, M. N. Dharmaweera, and H. Wymeersch, "Joint Assignment of Power, Routing, and Spectrum in Static Flexible-Grid Networks," *Journal of Lightwave Technology*, vol. 35, no. 10, pp. 1766–1774, May 15, 2017. DOI: 10.1109/JLT.2017.2657698.

[134] D. J. Ives and S. J. Savory, "How Pessimistic is a Worst-Case SNR Degradation as a Link Abstraction Metric?" In *2016 Optical Fiber Communication Conference*, OSA, 2016, Tu3F.6. DOI: 10.1364/OFC.2016.Tu3F.6.

[135] D. J. Ives, A. Lord, P. Wright, and S. J. Savory, "Quantifying the Impact of Non-linear Impairments on Blocking Load in Elastic Optical Networks," in *2014 Optical Fiber Communication Conference*, OSA, 2014, W2A.55. DOI: 10.1364/OFC.2014.W2A.55.

[136] J. Lopez Vizcaino, Y. Ye, and I. Tafur Monroy, "Energy efficiency analysis for flexible-grid OFDM-based optical networks," *Computer Networks*, vol. 56, no. 10, pp. 2400–2419, Jul. 2012. DOI: 10.1016/j.comnet.2012.03.012.

[137] P. Papanikolaou, K. Christodoulopoulos, and E. Varvarigos, "Multilayer flex-grid network planning," in *2015 International Conference on Optical Network Design and Modeling (ONDM)*, IEEE, May 2015, pp. 151–156. DOI: 10.1109/ONDM.2015.7127290.

[138] P. Papanikolaou, P. Soumplis, K. Manousakis, G. Papadimitriou, G. Ellinas, K. Christodoulopoulos, and E. Varvarigos, "Minimizing Energy and Cost in Fixed-Grid and Flex-Grid Networks," *Journal of Optical Communications and Networking*, vol. 7, no. 4, p. 337, Apr. 1, 2015. DOI: 10.1364/JOCN.7.000337.

[139] M. Cantono, R. Gaudino, and V. Curri, "Data-rate figure of merit for physical layer in fixed-grid reconfigurable optical networks," in *2016 Optical Fiber Communications Conference and Exhibition (OFC)*, OSA, 2016, Tu3F.3. DOI: 10.1364/OFC.2016.Tu3F.3.

[140] ——, "A statistical analysis of transparent optical networks comparing merit of fiber types and elastic transceivers," in *2016 18th International Conference on Transparent Optical Networks (ICTON)*, IEEE, Jul. 2016, pp. 1–4. DOI: 10.1109/ICTON.2016.7550511.

[141] Liang Zhang, Wei Lu, Xiang Zhou, and Zuqing Zhu, "Dynamic RMSA in spectrum-sliced elastic optical networks for high-throughput service provisioning," in *2013 International Conference on Computing, Networking and Communications (ICNC)*, IEEE, Jan. 2013, pp. 380–384. DOI: 10.1109/ICCNC.2013.6504113.

[142] P. Wright, A. Lord, and S. Nicholas, "Comparison of Optical Spectrum Utilization Between Flexgrid and Fixed Grid on a Real Network Topology," in *2012 Optical Fiber Communication Conference*, OSA, 2012, OTh3B.5. DOI: 10.1364/OFC.2012.OTh3B.5.

[143] H. Dai, Y. Li, and G. Shen, "Explore Maximal Potential Capacity of WDM Optical Networks Using Time Domain Hybrid Modulation Technique," *Journal of Lightwave Technology*, vol. 33, no. 18, pp. 3815–3826, Sep. 15, 2015. DOI: 10.1109/JLT.2015.2445056.

[144] A. Morea, J. Renaudier, T. Zami, A. Ghazisaeidi, and O. Bertran-Pardo, "Throughput comparison between 50-ghz and 37.5-ghz grid transparent networks [invited]," *IEEE/OSA Journal of Optical Communications and Networking*, vol. 7, no. 2, A293–A300, 2015. DOI: 10.1364/JOCN.7.00A293.

[145] D. J. Ives, P. Wright, A. Lord, and S. J. Savory, "Using 25 gbe client rates to access the gains of adaptive bit- and code-rate networking," *J. Opt. Commun. Netw.*, vol. 8, no. 7, A86–A91, Jul. 2016. DOI: 10.1364/JOCN.8.000A86.

[146] "IDEALIST FP7 Project, Deliverable D1.1-Elastic optical network architecture: Reference scenario, cost and planning," 2013.

[147] J. Y. Yen, "Finding the *K* Shortest Loopless Paths in a Network," *Management Science*, vol. 17, no. 11, pp. 712–716, Jul. 1971. DOI: 10.1287/mnsc.17.11.712.

[148] V. Curri, A. Carena, P. Poggiolini, R. Cigliutti, F. Forghieri, C. R. Fludger, and T. Kupfer, "Time-Division Hybrid Modulation Formats: Tx Operation Strategies and Countermeasures to Nonlinear Propagation," in *2014 Optical Fiber Communication Conference*, OSA, 2014, Tu3A.2. DOI: 10.1364/OFC.2014.Tu3A.2.

[149] M. Noelle, F. Frey, R. Elschner, C. Schmidt-Langhorst, A. Napoli, and C. Schubert, "Performance Comparison of Different 8QAM Constellations for the Use in Flexible Optical Networks," in *2014 Optical Fiber Communication Conference*, OSA, 2014, W3B.2. DOI: 10.1364/OFC.2014.W3B.2.

[150] D. J. Ives, A. Alvarado, and S. J. Savory, "Adaptive Transceivers in Nonlinear Flexible Networks," in *ECOC 2016; 42nd European Conference on Optical Communication*, Sep. 2016, pp. 1–3.

[151] D. J. Ives, A. Alvarado, and S. J. Savory, "Throughput Gains From Adaptive Transceivers in Nonlinear Elastic Optical Networks," *Journal of Lightwave Technology*, vol. 35, no. 6, pp. 1280–1289, Mar. 15, 2017. DOI: 10.1109/JLT.2017.2674308.

[152] S. K. Korotky, R.-J. Essiambre, and R. W. Tkach, "Expectations of optical network traffic gain afforded by bit rate adaptive transmission," *Bell Labs Technical Journal*, vol. 14, no. 4, pp. 285–295, Feb. 23, 2010. DOI: 10.1002/bltj.20416.

[153] S. Makovejs, C. Behrens, R.-P. Braun, S. Ten, C. Towery, I. Roudas, K. Koreshkov, T. Nath, and A. Gladisch, "Impact of Adaptive-Rate Transponders and Fiber Attributes on the Achievable Capacity," *Journal of Optical Communications and Networking*, vol. 7, no. 3, p. 172, Mar. 1, 2015. DOI: 10.1364/JOCN.7.000172.

[154] M. Ghobadi, J. Gaudette, R. Mahajan, A. Phanishayee, B. Klinkers, and D. Kilper, "Evaluation of Elastic Modulation Gains in Microsoft's Optical Backbone in North America," OSA, 2016, M2J.2. DOI: 10.1364/OFC.2016.M2J.2.

[155] A. Alvarado, D. J. Ives, S. J. Savory, and P. Bayvel, "Impact of Amplifier Noise Figure on Network Throughput," in *2016 Optical Fiber Communications Conference and Exhibition (OFC)*, OSA, Mar. 2016, Tu3F.4. DOI: 10.1364/OFC.2016.Tu3F.4.

[156] M. Cantono. (2017). Presentation of Research Activities, [Online]. Available: https://youtu.be/VWgTQeAIxdc?t=3m10s.

[157] O. Gerstel, M. Jinno, A. Lord, and S. Yoo, "Elastic optical networking: A new dawn for the optical layer?" *IEEE Communications Magazine*, vol. 50, no. 2, s12–s20, Feb. 2012. DOI: 10.1109/MCOM.2012.6146481.

[158] A. Lord, P. Wright, and A. Mitra, "Core Networks in the Flexgrid Era," *Journal of Lightwave Technology*, vol. 33, no. 5, pp. 1126–1135, Mar. 1, 2015. DOI: 10.1109/JLT.2015.2396685.

[159] P. Wright, A. Lord, and L. Velasco, "The network capacity benefits of Flexgrid," in *2013 17th International Conference on Optical Networking Design and Modeling (ONDM)*, Apr. 2013, pp. 7–12.

[160] A. Mitra, A. Lord, S. Kar, and P. Wright, "Effect of Link Margins and Frequency Granularity on the Performance and Modulation Format Sweet Spot of Multiple Flexgrid Optical Networks," in *2014 Optical Fiber Communication Conference*, OSA, 2014, W3A.6. DOI: 10.1364/OFC.2014.W3A.6.

[161] "ITU-T G.694.1 - Spectral grids for WDM applications: DWDM frequency grid," International Telecommunications Union, Feb. 2012.

[162] B. Smith, "Next Generation CDC ROADM," Sep. 18, 2017.

[163] "Next Generation CDC ROADM Solutions," Lumentum, 2017.

[164] W. I. Way, "Optimum Architecture for M×N Multicast Switch-Based Colorless, Directionless, Contentionless, and Flexible-Grid ROADM," in *National Fiber Optic Engineers Conference*, ser. National Fiber Optic Engineers Conference, Optical Society of America, 2012, NW3F.5. DOI: 10.1364/NFOEC.2012.NW3F.5.

[165] J. M. Simmons, "A Closer Look at ROADM Contention," *IEEE Communications Magazine*, vol. 55, no. 2, pp. 160–166, Feb. 2017. DOI: 10.1109/MCOM.2017.1600829CM.

[166] B. C. Collings, "Wavelength selectable switches and future photonic network applications," in *2009 International Conference on Photonics in Switching*, Sep. 2009, pp. 1–4. DOI: 10.1109/PS.2009.5307841.

[167] P. Colbourne, "ROADM switching technologies," in *2011 Optical Fiber Communication Conference and Exposition and the National Fiber Optic Engineers Conference*, Mar. 2011, pp. 1–3.

[168] M. Cantono, R. Gaudino, P. Poggiolini, and V. Curri, "Comparing Networking Benefits of Digital Back-Propagation vs. Lightpath Regeneration," in *ECOC 2016; 42nd European Conference on Optical Communication*, Sep. 2016, pp. 1–3.

[169] A. Ferrari, M. Cantono, U. Waheed, A. Ahmad, and V. Curri, "Networking benefits of advanced DSP techniques and hybrid fiber amplification," in *2017 19th International Conference on Transparent Optical Networks (ICTON)*, Jul. 2017, pp. 1–4. DOI: 10.1109/ICTON.2017.8025170.

[170] M. Cantono, A. Ferrari, U. Waheed, A. Ahmad, S. M. H. Zaidi, A. Bianco, and V. Curri, "Networking benefit of hybrid fiber amplification for lightpath regenerators saving," in *2017 Optical Fiber Communications Conference and Exhibition (OFC)*, Mar. 2017, pp. 1–3.

[171] OOPT_PSE. (). GNpy: Optical Route Planning Based on Gaussian Noise Model, [Online]. Available: https://github.com/Telecominfraproject/gnpy.

[172] G. Grammel, V. Curri, and J. L. Auge, "Physical Simulation Environment of The Telecommunications Infrastructure Project (TIP)," in *2018 Optical Fiber Communication Conference*, 2018. DOI: 10.1364/OFC.2018.M1D.3.

[173] B. Taylor, G. Goldfarb, S. Bandyopadhyay, V. Curri, and H.-J. Schmidtke, "Towards a Route Planning Tool for Open Optical Networks in the Telecom Infrastructure Project," in *2018 Optical Fiber Communication Conference*, 2018. DOI: 10.1364/OFC.2018.Tu3E.4.

[174] M. Filer, M. Cantono, A. Ferrari, G. Grammel, G. Galimberti, and V. Curri, "Multi-vendor Experimental Validation of an Open Source QoT Estimator for Optical Networks," *submitted to Journal of Lightwave Technology*, 2018.

[175] D. Hicks, C. Malina-Maxwell, M. Razo, M. Tacca, A. Fumagalli, and D. Nguyen, "PROnet: A programmable optical network prototype," in *2016 18th International Conference on Transparent Optical Networks (ICTON)*, IEEE, Jul. 2016, pp. 1–4. DOI: 10.1109/ICTON.2016.7550421.

[176] D. Christodoulides and R. Jander, "Evolution of stimulated Raman crosstalk in wavelength division multiplexed systems," *IEEE Photonics Technology Letters*, vol. 8, no. 12, pp. 1722–1724, Dec. 1996. DOI: 10.1109/68.544731.

[177] A. Betker, C. Gerlach, R. Hülsermann, M. Jäger, M. Barry, S. Bodamer, J. Späth, C. Gauger, and M. Köhn, "Reference transport network scenarios," *MultiTeraNet Report*, 2003.

[178] M. Cantono, D. Pilori, A. Ferrari, A. Carena, and V. Curri, "Observing the Interaction of PMD with Generation of NLI in Uncompensated Am- plified Optical Links," in *2018 Optical Fiber Communications Conference and Exhibition (OFC)*, Mar. 2018, pp. 1–3. DOI: 10.1364/OFC.2018.W1G.4.

Appendix A

Physical Layer Parameters and Topology References

In this appendix, the typical parameters for physical layer components and the network topologies used throughout the thesis will be listed.

A.1 Fiber types

In this section, the propagation parameters for different fiber types are reported. Typical fiber parameters are reported in Tab.A.1 for Standard Single Mode Fiber (SSMF), Non-Zero Dispersion Shifted Fiber (NZDSF), and Pure Silica Core Fiber (PSCF). , and Corning SMF-28e+ commercial SMF.

Table A.1 Typical Fiber Parameters

Parameter	**SMF**	**NZDSF**	**PSCF**	**Corning SMF-28e+®**
Attenuation – α_{dB} [dB/km]	0.20	0.22	0.167	0.2
Chromatic dispersion – D [ps/nm/km]	16.7	3.8	21.0	17
Non-linear coefficient – γ [1/W/km]	1.3	1.45	0.9	1.2
Effective Area – A_{eff} [μm^2]	80	70	120	80

A.2 Network Topologies

The different network topologies considered in this thesis are depicted in the following figures. Their main topological characteristics are reported in Tab. A.2. The considered topologies are depicted in Fig. A.1-Fig. A.5. Fiber types, unless reported on the figure, are detailed in the body of the thesis.

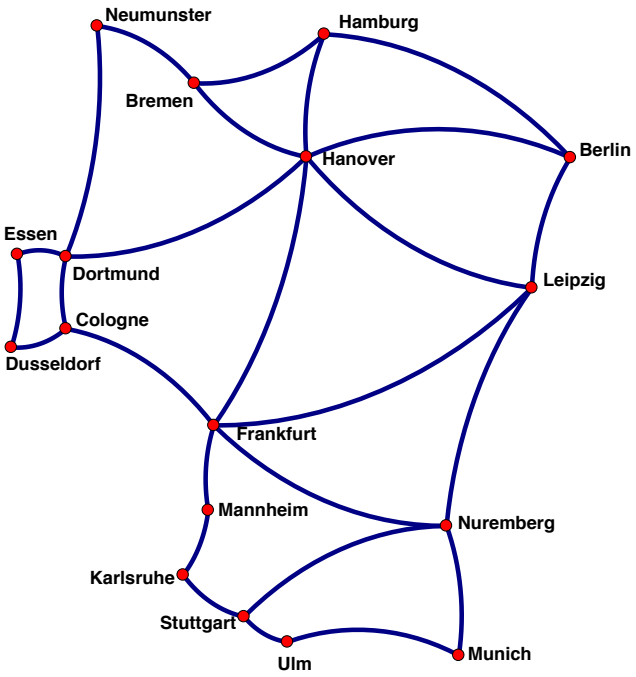

Fig. A.1 German topology.

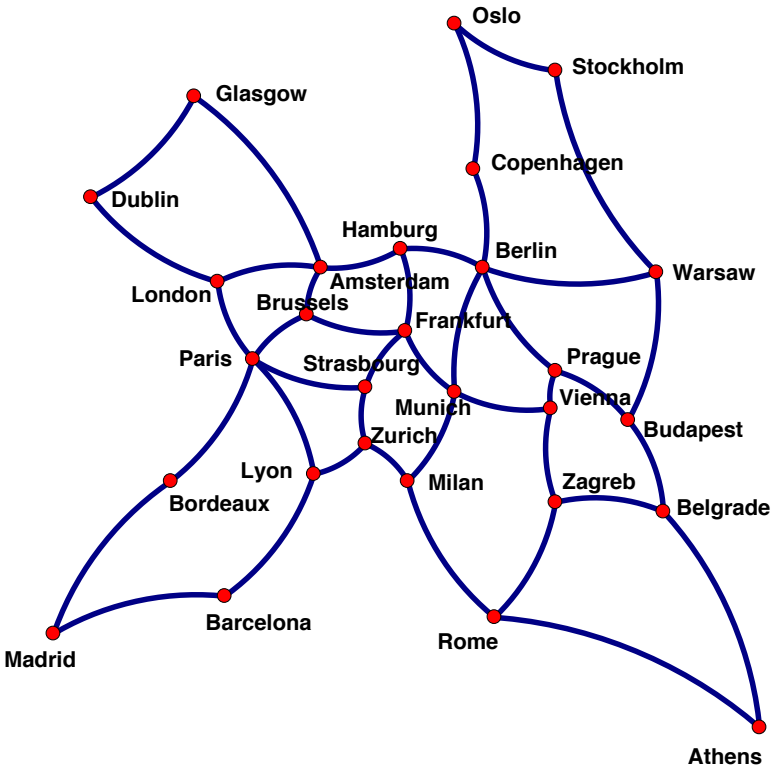

Fig. A.2 Pan-European topology.

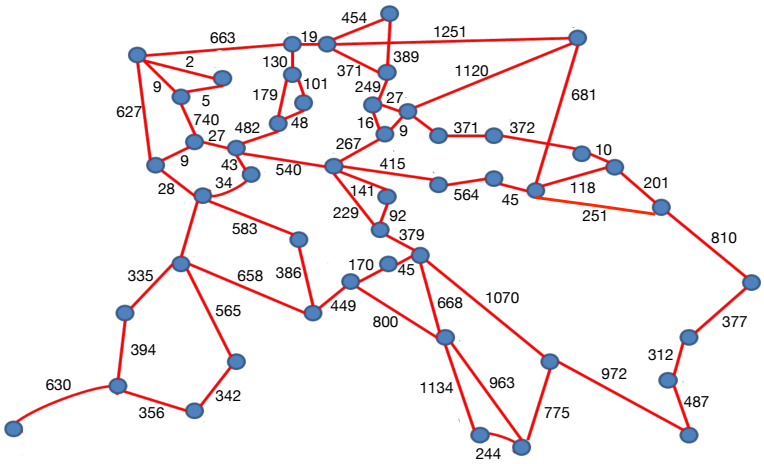

Fig. A.3 Telecom Italia Sparkle Pan-European topology. Labels represent link lenghts in km.

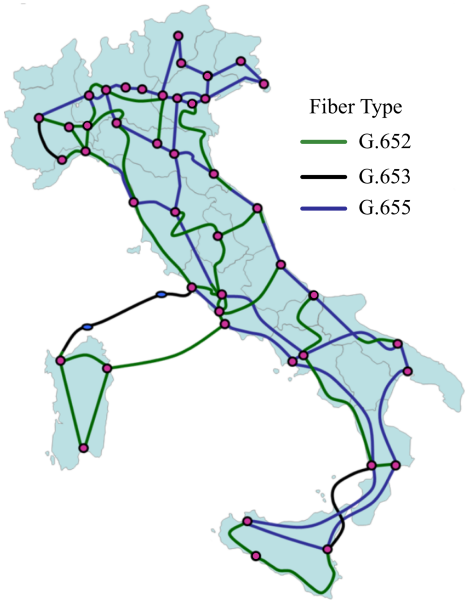

Fig. A.4 Telecom Italia topology.

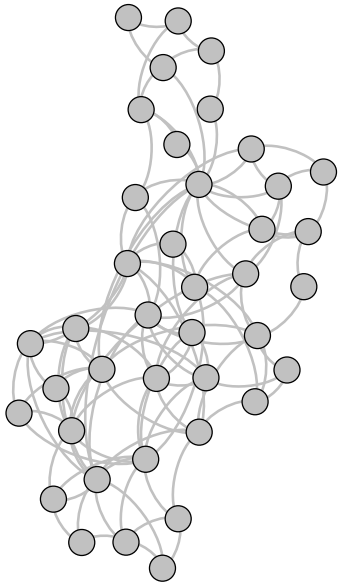

Fig. A.5 Metro Network topology.

Table A.2 Topology Data

Parameter	German	Pan-European	Sparkle Pan-EU	Telecom Italia	Metro
Number of nodes	17	28	49	44	40
Number of links	26	41	68	71	107
Average Link Length [km]	207	637	384	174	11
Average node degree	3.06	2.98	2.78	3.36	5.35
Reference Figure	Fig. A.1	Fig. A.2	Fig. A.3	Fig. A.4	Fig. A.5
Source	[177]	[177]	[146]	[146]	Internal

A.3 BER vs SNR for different modulation format

In this section, BER vs SNR performance curves for different PM-M-QAM modulation formats are reported. The curves are based on the well-known formulae for AWGN channel performance estimation [70]. The curves are reported in Fig. A.6 and they are used in this thesis to derive SNR sensitivity requirements for different modulation format at a given pre-FEC BER level.

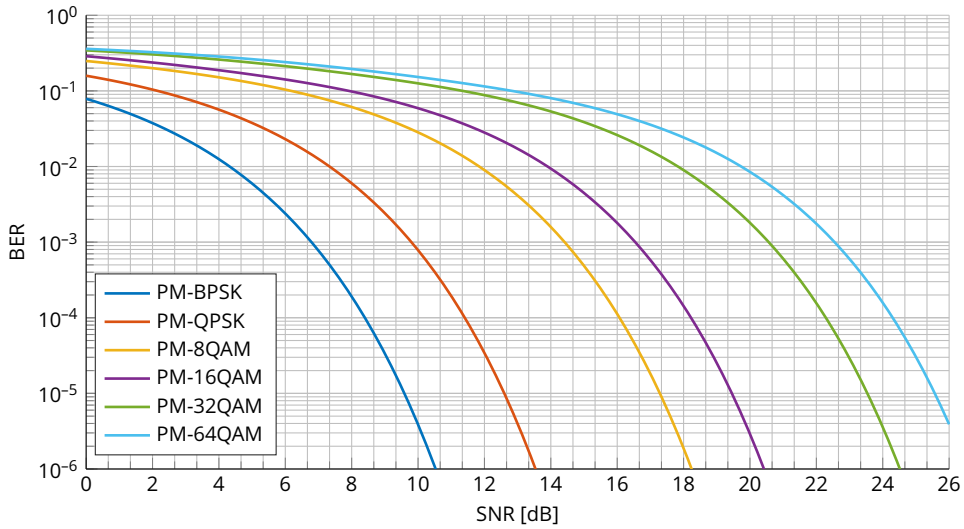

Fig. A.6 BER vs SNR for different modulation formats on AWGN channel.

Appendix B

Analytical derivation of the GGN-model.

The derivation of the GGN-model follows the method already exploited in deriving the GN-model detailed described in [88], so assuming to analyze the propagation of Gaussian distributed spectral components. Then, in addition to [88] hypotheses, we suppose frequency/space variation of power profile in fiber spans. As in [88], we develop the model exploiting the single-polarization wave equation in fibers – the nonlinear Schrödinger equation (NLSE) – then, we generalize the results including polarization relying on the Manakov equation (ME), i.e., on the dual-polarization NLSE with random birefringence – and consequent PMD effect – averaged out. It has been shown that the ME can be reliably used far beyond its validity bandwidth in case of propagation of Gaussian distributed and depolarized signals [114], [178], so this will be the validity scenario for the GGN-model.

The nonlinear Schrödinger equation (NLSE), in the frequency domain, has the following form:

$$\partial_z E(z,f) = [g(z,f) - j\beta(f)]\, E(z,f) + Q_{NLI}(z,f) \tag{B.1}$$

where z is the propagation direction, $E(z,f)$ is the Fourier transform of the propagating modal amplitude, ∂_z is the partial derivative of $E(z,f)$ with respect to z, $\beta(f)$ is the dispersion coefficient, $g(z,f)$ is the profile of amplitude evolution of modal amplitude that may vary with respect to both z and f,

$Q_{NLI}(z, f)$ is the nonlinear term determined by the Kerr effect that is given by:

$$Q_{NLI}(z, f) = -j\gamma E(z, f) * E^*(z, -f) * E(z, f) \ . \tag{B.2}$$

where "$*$" is the convolution operator. according to the theory of differential equation, the formal solution of Eq. B.1, i.e., of the evolution of the Fourier transform of the modal amplitude vs. z, has the following form:

$$E(z, f) = e^{\Gamma(z,f)} \int_0^z e^{-\Gamma(\zeta,f)} Q_{NLI}(\zeta, f) d\zeta \ + \ e^{\Gamma(z,f)} E(0, f) \tag{B.3}$$

where $\Gamma(z, f)$ is given by:

$$\Gamma(z, f) = \int_0^z -j\beta(f) + g(\zeta, f) d\zeta = -j\beta(f) z + \int_0^z g(\zeta, f) d\zeta \tag{B.4}$$

We can subdivide $E(z, f)$ solution of Eq. B.3 as the sum of two components: $E_{LIN}(z, f)$ considering linear propagation effects only ($g(z, f) - j\beta(f)$), and $E_{NLI}(z, f)$ considering the impairment of Kerr effect and its interaction with linear propagation. Therefore,

$$E(z, f) = E_{NLI}(z, f) + E_{LIN}(z, f) \ , \tag{B.5}$$

where the linear component $E_{LIN}(z, f)$ is:

$$E_{LIN}(z, f) = e^{\Gamma(z,f)} E(0, f) \ , \tag{B.6}$$

and the nonlinear component $E_{NLI}(z, f)$ is:

$$E_{NLI}(z, f) = e^{\Gamma(z,f)} \int_0^z e^{-\Gamma(\zeta,f)} Q_{NLI}(\zeta, f) d\zeta \tag{B.7}$$

In general, the formal solution of Eq. B.3 for the modal amplitude evolution is useful to observe the two contributes – linear and nonlinear – to propagation impairments, but cannot be practically exploited, because the unknown function $E(z, f)$ is also in the right side term of Eq. B.3 being the cause of $Q_{NLI}(z, f)$ as clearly displayed by Eq. B.2.

Perturbative Approach on the nonlinear Impairment

In silica fibers, the strength of Kerr effect is much less intense of impairments of linear propagation, mainly given by chromatic dispersion. So, we are legitimate to exploit a perturbative approach for which $E_{NLI}(z,f)$ is indeed a perturbation of $E_{LIN}(z,f)$. Consequently, we may assume that the nonlinear term defined in Eq. B.2 is induced only by the linear component $E_{LIN}(z,f)$ of the modal amplitude $E(z,f)$. Such an approximation yields to not considering the second-order effects, i.e., the nonlinear effects induced by $E_{NLI}(z,f)$. So, practically, the perturbative approach implies to use the following form for $Q_{NLI}(z,f)$ in place of the *exact* one of Eq. B.2:

$$Q_{NLI}(z,f) = -j\gamma E_{LIN}(z,f) * E^*_{LIN}(z,-f) * E_{LIN}(z,f)\ . \tag{B.8}$$

As the convolution operator is defined as:

$$x(t) * h(t) = \int_{-\infty}^{\infty} x(\tau)h(t-\tau)d\tau\ , \tag{B.9}$$

we can expand Eq. B.8 in the following form:

$$\begin{aligned}
&Q_{NLI}(z,f) = \\
&= -j\gamma \left[\int_{-\infty}^{+\infty} e^{\Gamma(z,f_1)} e^{\Gamma^*(z,f_1-f)} E(0,f_1)E^*(0,f_1-f)df_1\right] * \\
&\quad * \left[e^{\Gamma(z,f)}E(0,f)\right] && \text{(B.10)}\\
&= -j\gamma \iint_{-\infty}^{+\infty} e^{\Gamma(z,f_1)} e^{\Gamma^*(z,f_1-f_2)} e^{\Gamma(z,f-f_2)}\cdot \\
&\quad \cdot E(0,f_1)E^*(0,f_1-f_2)E(0,f-f_2)df_1df_2 && \text{(B.11)}\\
&= -j\gamma \iint_{-\infty}^{+\infty} e^{\Gamma(z,f_1)+\Gamma^*(z,f_1-f_2)+\Gamma(z,f-f_2)}\cdot \\
&\quad \cdot E(0,f_1)E^*(0,f_1-f_2)E(0,f-f_2)df_1df_2 && \text{(B.12)}\\
&= -j\gamma \iint_{-\infty}^{+\infty} A(z,f)\cdot \\
&\quad \cdot E(0,f_1)E^*(0,f_1-f_2)E(0,f-f_2)df_1df_2 && \text{(B.13)}
\end{aligned}$$

where $A(z, f)$ is:

$$\begin{aligned} &A(z, f) = \\ &= \exp\left(\int_0^z -j[\beta(f_1) - \beta(f_1 - f_2) + \beta(f - f_2)] + \right. \\ &\quad \left. + [g(\zeta, f_1) + g(\zeta, f_1 - f_2) + g(\zeta, f - f_2)]d\zeta\right). \end{aligned} \tag{B.14}$$

Then, inserting Eq. B.4 in Eq. B.7 we get the following expression for the perturbation $E_{NLI}(z, f)$:

$$\begin{aligned} &E_{NLI}(z, f) = \\ &= e^{-j\beta(f)z} e^{\int_0^z g(\zeta,f)d\zeta} \cdot \\ &\quad \cdot \int_0^z e^{j\beta(f)} e^{-\int_0^\zeta g(z_1,f)dz_1} Q_{NLI}(\zeta, f)d\zeta \\ &= e^{-j\beta(f)z} e^{\int_0^z g(\zeta,f)d\zeta} I(z, f) \end{aligned} \tag{B.15}$$

where $I(z, f)$ is:

$$\begin{aligned} &I(z, f) = \\ &= -j\gamma \iint_{-\infty}^{+\infty} E(0, f_1) E^*(0, f_1 - f_2) E(0, f - f_2) \\ &\quad \int_0^z \exp(+j\beta(f)\zeta) \\ &\quad A(\zeta, f) \exp\left(-\int_0^\zeta g(z_1, f)dz_1\right) d\zeta df_1 df_2 \end{aligned} \tag{B.16}$$

Substituting in Eq. B.15 the expression of $I(z,f)$ we obtain the following expression for the nonlinear perturbation introduced by the Kerr effect:

$$\begin{aligned}
&E_{NLI}(z,f) = \\
&= e^{-j\beta(f)z} e^{\int_0^z g(\zeta,f)d\zeta} I(z,f) \\
&\quad - j\gamma \iint_{-\infty}^{+\infty} E(0,f_1)E^*(0,f_1-f_2)E(0,f-f_2) \\
&\quad \int_0^z \exp(+j\beta(f)\zeta) \\
&\quad A(\zeta,f)\exp\left(-\int_0^\zeta g(z_1,f)dz_1\right) d\zeta df_1 df_2 \,.
\end{aligned} \tag{B.17}$$

Note that Eq. B.17 relies on the only approximation of Kerr effect being a perturbation of linear propagation and does include frequency/space variations of loss and gain as $g(\zeta,f)$ in addition to frequency variations of the propagation constant $\beta(f)$.

NLI Power Spectral Density

In this section, we rely on the same signal form – depolarized and Gaussian signals – and follow the same procedure of [88] to derive the power spectral density $G_{NLI}(z,f)$ of $E_{NLI}(z,f)$, that is assumed to be a Gaussian random process. Specifically, using Eq. 16 of [88], one can write the NLI field as

$$\begin{aligned}
&E_{NLI}(z,f) = -j\gamma f_0^{\frac{3}{2}} e^{-j\beta(f)z} e^{\int_0^z g(\zeta,f)d\zeta} \cdot \\
&\sum_{i=-\infty}^{+\infty} \delta(f-if_0) \sum_{m,n,k\in\widetilde{A}_i} \sqrt{G_{TX}(mf_0)G_{TX}(nf_0)G_{TX}(kf_0)} \cdot \\
&\xi_m \xi_n^* \xi_k \int_0^z \exp[-\Gamma(\zeta,(m-n+k)f_0) + \Gamma(\zeta,mf_0) + \\
&+ \Gamma^*(\zeta,nf_0) + \Gamma(\zeta,kf_0)]d\zeta
\end{aligned} \tag{B.18}$$

where f_0 is a divider of the symbol rate, ξ is a complex Gaussian random variable and $\delta(f)$ is the Dirac delta function. $\widetilde{A}_i$ represents the set of all triples (m,n,k) such that $m-n+k=i$ and $m \neq n$ or $k \neq n$. This set identifies all non degenerate fourwave mixing components, as detailed in

[88]. Following the same averaging procedure of Sec. IV (D) of [88], one obtains the following expression for the single polarization expression of the power spectral density of the NLI noise, i.e.

$$
\begin{aligned}
&G_{NLI}^{sp}(z,f) = 2\gamma^2 f_0^3 \left| \exp\left[\int_0^z g(\zeta,f)d\zeta\right]\right|^2 \cdot \\
&\sum_{i=-\infty}^{+\infty} \delta(f-if_0) \sum_m \sum_k G_{TX}(mf_0)G_{TX}(kf_0)\cdot \\
&G_{TX}((m-i+k)f_0) \int_0^z \exp[-\Gamma(\zeta,if_0)+ \\
&+\Gamma(\zeta,mf_0)+\Gamma^*(\zeta,(m-i+k)f_0)+\Gamma(\zeta,kf_0)]d\zeta
\end{aligned}
\tag{B.19}
$$

Similarly, considering a dual polarization signal, following the exact derivation of the previous section and the averaging procedure of Sec.IV (E) in [88] one can write the PSD of the NLI noise generated by dual-polarization signals as

$$
\begin{aligned}
&G_{NLI}(z,f) = \frac{16}{27}\gamma^2 f_0^3 \left| \exp\left[\int_0^z g(\zeta,f)d\zeta\right]\right|^2 \cdot \\
&\sum_{i=-\infty}^{+\infty} \delta(f-if_0) \sum_m \sum_k G_{TX}(mf_0)G_{TX}(kf_0)\cdot \\
&G_{TX}((m-i+k)f_0) \int_0^z \exp[-\Gamma(\zeta,if_0)+ \\
&+\Gamma(\zeta,mf_0)+\Gamma^*(\zeta,(m-i+k)f_0)+\Gamma(\zeta,kf_0)]d\zeta
\end{aligned}
\tag{B.20}
$$

Then, taking the limit of Eq. B.20 for $f_0 \to 0$, such expression can be written as:

$$\begin{aligned} &G_{NLI}(z,f) = \\ &= \frac{16}{27}\gamma^2 \left| e^{\int_0^z g(\zeta,f)d\zeta} \right|^2 \cdot \\ &\quad \cdot \iint_{-\infty}^{+\infty} G_{TX}(f_1) G_{TX}(f_2) G_{TX}(f_1+f_2-f) \cdot \\ &\quad \cdot \left| \int_0^z e^{+j[\beta(f_1+f_2-f)-\beta(f_1)+\beta(f)-\beta(f_2)]\zeta} \cdot \right. \\ &\quad \left. \cdot e^{+\int_0^\zeta g(z_1,f_1)-g(z_1,f)+g(z_1,f_2)+g(z_1,f_1+f_2-f)dz_1} d\zeta \right|^2 \cdot \\ &\quad \cdot df_1 df_2 \,. \end{aligned} \tag{B.21}$$

To compact the expression, we introduce the following function $\rho(z,f)$ that considers the evolution of the modal amplitude vs. z for each spectral component f:

$$\rho(z,f) = e^{\int_0^z g(\zeta,f)d\zeta} \,. \tag{B.22}$$

This expression may include the effect of frequency variation of loss coefficient, of SRS-induced crosstalk and of distributed amplification.

Exploiting the linearity of the integral operator and the properties of the exponential function, we can rewrite the Eq. B.21 as:

$$\begin{aligned} &G_{NLI}(z,f) = \\ &= \frac{16}{27}\gamma^2 \rho(z,f)^2 \cdot \\ &\quad \cdot \iint_{-\infty}^{+\infty} G_{TX}(f_1) G_{TX}(f_2) G_{TX}(f_1+f_2-f) \cdot \\ &\quad \cdot \left| \int_0^z e^{+j[\beta(f_1+f_2-f)-\beta(f_1)+\beta(f)-\beta(f_2)]\zeta} \cdot \right. \\ &\quad \left. \cdot \frac{\rho(\zeta,f_1)\rho(\zeta,f_1+f_2-f)\rho(\zeta,f_2)}{\rho(\zeta,f)} d\zeta \right|^2 df_1 df_2 \,. \end{aligned} \tag{B.23}$$

Finally obtaining the following expression for the NLI PSD that is the also the final expression of the generalized Gaussian noise model for NLI

generated by a single fiber span.

$$\begin{aligned} &G_{NLI}(z,f) = \\ &= \frac{16}{27}\gamma^2\rho(z,f)^2 \iint_{-\infty}^{+\infty} G_{TX}(f_1)G_{TX}(f_2)G_{TX}(f_1+f_2-f)\cdot \\ &\quad \cdot \left| \int_0^z e^{+j\Delta\beta(f_1,f_2,f)\zeta}\Delta\rho(z,f,f_1,f_2)d\zeta \right|^2 df_1 df_2 \end{aligned} \tag{B.24}$$

where $\Delta\rho$ is given by

$$\Delta\rho(z,f,f_1,f_2) = \frac{\rho(\zeta,f_1)\rho(\zeta,f_1+f_2-f)\rho(\zeta,f_2)}{\rho(\zeta,f)} \tag{B.25}$$

The use of Eq. B.24 in multi-span links is straightforward as for the GN-model. and $\Delta\beta$

$$\Delta\beta(z,f,f_1,f_2) = [\beta(f_1+f_2-f) - \beta(f_1) + \beta(f) - \beta(f_2)]z \tag{B.26}$$

that can be further expanded as

$$\Delta\beta(z,f,f_1,f_2) = 4\pi^2(f_1-f)(f_2-f)[\beta_2 + \pi\beta_3(f_1+f_2)]z \tag{B.27}$$

as detailed described in Eq. G.2 of [88]. Eq. B.24 can be also expanded to be used with coherent accumulation with spans inserting the "phased-array" factor, or relying on the incoherent accumulation simply adding up independently NLI generated by each fiber span.